

PHOTOLUMINESCENCE PROPERTIES OF Si NANOCRYSTALS
EMBEDDED IN SiO₂ MATRIX

A THESIS SUBMITTED TO
THE GRADUATE SCHOOL OF NATURAL AND APPLIED SCIENCES
OF
MIDDLE EAST TECHNICAL UNIVERSITY

BY

AYŞE SEYHAN

IN PARTIAL FULFILLMENT OF THE REQUIREMENTS
FOR
THE DEGREE OF DOCTOR OF PHILOSOPHY
IN
PHYSICS

MARCH 2010

Approval of the thesis:

**PHOTOLUMINESCENCE PROPERTIES OF Si NANOCRYSTALS
EMBEDDED IN SiO₂ MATRIX**

submitted by **Ayşe Seyhan** in partial fulfillment of the requirements for the degree
of **Doctor of Philosophy in Physics Department, Middle East Technical
University** by,

Prof. Dr. Canan Özgen
Dean, Graduate School of **Natural and Applied Sciences** _____

Prof. Dr. Sinan Bilikmen
Head of Department, **Physics** _____

Prof. Dr. Raşit Turan
Supervisor, **Department of Physics, METU** _____

Examining Committee Members:

Prof. Dr. Mehmet Parlak
Department of Physics, METU _____

Prof. Dr. Raşit Turan
Department of Physics, METU _____

Prof. Dr. Bahtiyar Salamov
Department of Physics, Gazi University _____

Prof. Dr. Nizami Hasanlı
Department of Physics, METU _____

Asst. Prof. Uğur Serincan
Department of Physics, Anadolu University _____

Date: _____ 12.03.2010 _____

I hereby declare that all information in this document has been obtained and presented in accordance with academic rules and ethical conduct. I also declare that, as required by these rules and conduct, I have fully cited and referenced all material and results that are not original to this work.

Name, Last name : Ayşe Seyhan

Signature :

ABSTRACT

PHOTOLUMINESCENCE PROPERTIES OF Si NANOCRYSTALS EMBEDDED IN SiO₂ MATRIX

Seyhan, Ayşe

PhD, Department of Physics

Supervisor: Prof. Dr. Raşit Turan

March 2010, 101 pages

This thesis examines the luminescence properties of nanoscale silicon (Si) by using spectroscopic techniques. Since the development of new optical devices requires understanding light emission mechanism optical spectroscopy has become more important tool in the analysis of these structures. In this thesis, Si nanocrystals embedded in SiO₂ matrix will be studied.

Photoluminescence (PL) and Time-resolved photoluminescence spectroscopy (TRPL) have been used to detect the light emission in UV-Vis-NIR range. Experiments have been performed in the temperature range 10-300 K. PL is sensitive to impurities and defects that affect materials quality and device performance. In this context, the role of defects in limiting the luminescence of Si nanocrystals and the removal of these defects by hydrogen passivation has been investigated.

TRPL was employed to determine the time evolution of photoluminescence as function of temperature. The decay time of the PL spectra was determined by a stretched exponential function and perfectly fitted to an expression based on three excitonic levels. Carrier lifetimes associated with these three levels were determined and compared with literature.

Additionally, temporal variation of PL from free-standing Si nanoparticles is studied under a strong laser illumination. The observed bleaching behavior (time dependent emission intensity), which is reversible, have discussed in terms of exciton trapping at the interface between nanocrystal and the surrounding oxide layer.

The results of this thesis will provide new insight on the understanding of light emission mechanism of Si nanocrytals.

Keywords: Silicon, Nanocrystals, Photoluminescence, Time-resolved Photoluminescence, Free-standing Si.

ÖZ

SiO₂ MATRİKS İÇERİSİNE GÖMÜLMÜŞ Si NANOKRİSTALLERİN FOTOLUMİNESANS ÖZELLİKLERİ

Seyhan, Ayşe

Doktora, Fizik Bölümü

Tez Yöneticisi: Prof. Dr. Raşit Turan

Mart 2010, 110 sayfa

Bu tez, nano boyutta silikonların optik özelliklerini inceler. Yeni optiksel aygıtların gelişmesi, ışık çıkma mekanizmaların anlaşılmasını gerektirdiği için optiksel spektroskopi bu yapıların analizinde bir araç olarak daha çok önem kazanmıştır. Bu tezde SiO₂ matris içine gömülen Si nanokristaller çalışılmıştır.

Analiz tekniği olarak fotoluminesans ve zaman çözömlü fotoluminesans spektroskopisi UV-Vis-NIR bölgelerini araştırmakta kullanılmıştır. Ölçümler 10-300 K sıcaklık aralığında yapılmıştır. Fotoluminesans, aygıtların performansını ve kalitesini etkileyen kusurlara duyarlıdır. Bu bağlamda, silicon nanokristallerin luminesansını sınırlayan kusurların rolü ve bu kusurların hidrojen pasivasyonu araştırılmıştır.

Zaman çözümlü fotoluminesans spektroskopisi fotoluminesansın zaman değişimini sıcaklığın fonksiyonu olarak belirlemede kullanılmıştır. PL spektrumlarının sönüm süresinin sıcaklığa bağlılığı, üç eksiton seviyesi üzerine kurulu ifadeye mükemmel şekilde uymuştur. Bu üç seviye ile ilişkilendirilen taşıyıcı ömrü belirlenmiş ve literature ile karşılaştırılmıştır.

Ek olarak, güçlü lazer aydınlatması altında serbest duran silikon nanoparçacıkların zaman bağımlı fotoluminesans varyasyonu çalışılmıştır. Geridönüşür olan gözlemlenen ağarma davranışı (zaman bağımlı emisyon yoğunluğu) nanocrystal ve çevresindeki oksit tabakası arasındaki arayüzde eksiton yakalanması olarak tartışılmıştır.

Bu tezin sonuçları ışık çıkma mekanizmalarının anlaşılması ve onların optoelektronik aletler için potansiyel kullanımlarına yeni bir görüş sağlayacaktır.

Anahtar Kelimeler: Silicon nanokristal, Fotoluminesans, Zaman-çözümlü fotoluminesans, serbest duran nanokristaller.

to my lovely family...

ACKNOWLEDGEMENTS

I wish to endless thank my supervisor Prof. Dr. Raşit Turan: he has provided me the possibility to face with the academic world and has constantly stimulated me to do my best. His Vision, enthusiasm and support have been major factors in completion of a Ph.D thesis.

I want to express my gratitude to Prof.Dr. Magnus Willander and other members of Linkoping group. Thanks for giving me the opportunity to study their Time-resolved Photoluminescence laboratory, his thoughtful discussion and his support.

I am so sorry I could not find the opportunity to study with an excellent physicist Dr. Marcofabio Righini due to untimely death. At least, I am lucky that I got the chance to work in his laboratory at CNR in Rome. I am also deeply grateful to Dr. Andrea Gnoli and Rosanna not only teaching me TRPL but also friendships.

I am also grateful to Assoc. Prof. Dr. Ceyhun Bulutay for his scientific knowledge; support and helping me gain very valuable insights on Si nanocrystals.

I would like also to thank Assocs. Prof. Dr. Ugur Serincan and Asist. Prof. Dr. Bülent Aslan for support and proficient aid on my initial experiments. Support from Mustafa Kulakçı was also indispensable. His friendliness and endless support during this work is so much important for me. Thank you!!

A special thank is dedicated to Dr. Hasan Yıldırım for his fundamental help on discussions, his support and being with me during difficult times.

I am really grateful to Assocs. Prof. Dr. Ismail Turan; he made unforgettable encouraged me during the difficult moments.

All the members of the Semiconductor Materials and Devices Group are acknowledged: Yücel Eke, Arife Gencer, Nader A. P. Moghaddam, Urcan Güler, Ilker Dođan, Umut Bostancı, Döndü Şahin, Buket Kaleli, Zeynep Deniz Eygi, İlker Yıldız, Seçkin Öztürk and Sedat Canlı.

A fervid thank is dedicated to all my friends for the sharing good things, their support and funny time spent together. I feel so lucky to always have the support and camaraderie of their supportive, interesting, and fun individuals. (Banu Özel, Elif Beklen, Hatice Eşberk, Nuray Ateş, Gülderen Tarcan Sağlam, Ali Sarıgöl, Vural Köksal, Ayşe Arat, Mine Kalkancı, Fevziye Dolunay, Tuba Fidan, Kadir Gökşen, Volkan Çuha, Cüneyt Erođlu, Dođan Mansurođlu)

Finally, I wish to thank heartily my parents, sister and brother for the support and love they gave to me during these years of PhD.

I would like to thank to Scientific and Technological Research Council of Turkey (TUBITAK) for partial financial support during this study.

TABLE OF CONTENTS

ABSTRACT	iv
ÖZ	vi
DEDICATION	viii
ACKNOWLEDGMENTS	ix
TABLE OF CONTENTS	xi
LIST OF TABLES	xiv
LIST OF FIGURES	xv
LIST OF ABBREVIATIONS.....	xvi
CHAPTERS	
1. INTRODUCTION	1
1.1. Motivation.....	1
1.2. Si Nc as a new light emitting structure for Si-based technology.....	2
1.3. Thesis Structure.....	8
References.....	9
2. EXPERIMENTAL.....	10
2.1. Sample Preparation Methodology.....	10
2.1.1. Ion Implantation.....	10
2.1.2. Magnetron Sputtering.....	11

2.1.3. Preparation of Free Standing Nanocrystals by Laser Pyrolysis Technique.....	13
2.2. Sample Details.....	16
2.2.1. Thermal Annealing and Hydrogen Passivation.....	16
2.2.2. Samples.....	16
2.3. Sample Characterization.....	18
2.3.1. Photoluminescence Spectroscopy.....	18
2.3.2. Time-Resolved Photoluminescence.....	22
2.3.3. Raman spectroscopy.....	23
2.3.4. Transmission electron microscopy (TEM).....	23
3. PHOTOLUMINESCENCE SPECTROSCOPY OF Si NANOCRYSTALS	
3.1 Introduction.....	24
3.2 PL, Influence of using different production techniques.....	25
3.3 PL, Effects of annealing temperature on PL from Si nanocrystals.....	29
3.4 PL, Effect of dose on PL from Si nanocrystals.....	30
3.5. The effect of H ₂ passivation on PL from Si nanocrystals.....	32
3.6. Conclusion.....	35
4. TEMPERATURE DEPENDENT PHOTOLUMINESCENCE OF Si NANOCRYSTALS	
4.1 Introduction.....	36
4.2 Experiment.....	38
4.2.1. Preparation of Silicon (Si) Nanocrystals in SiO ₂	38
4.2.2. Photoluminescence and Time Resolved Measurements.....	38
4.3. Results and Discussions.....	39
4.4. Conclusion.....	43
5. TIME-RESOLVED PHOTOLUMINESCENCE OF Si NANOCRYSTALS..	
5.1. Introduction.....	44

5.2. Experiment.....	45
5.3. Excitonic Model for Si NC's.....	45
5.4. Conclusion.....	54
6. LIGHT EMISSION FROM FREE-STANDING Si NANOCRYSTALS...	
6.1. Historical Perspective.....	56
6.2. Temperature dependent photoluminescence properties of Free-standing Si Nanocrystals.....	57
6.4. Photoluminescence Experiments as a function of Time	67
6.5. Photoluminescence bleaching and possible mechanisms for the observed intensity decay.....	73
6.6. Raman Spectroscopy.....	76
6.7. Transmission electron microscopy (TEM).....	83
6.8. Conclusion.....	86
7. CONCLUSIONS.....	87
REFERENCES.....	90
CURRICULUM VITAE.....	98

LIST OF TABLES

TABLES

Table 2.1. Ion Implantation conditions of samples.....	17
Table 2.2. Sputtering parameter of samples.....	17
Table 2.3. Laser Pyrolysis properties of samples.....	17
Table 3.1. Details of the implantation process. Samples were implanted with 1×10^{17} W/cm ² silicon doses and annealed at 800, 900, 1050 °C.....	29
Table 6.1. The deconvolution parameters of the Raman spectra for all samples..	83

LIST OF FIGURES

FIGURES

Figure 1.1 PL spectroscopy of sample implanted with different dose ^{28}Si into SiO_2/Si substrate. Sample labels (Si ion dose) are A ($1.5 \times 10^{17} \text{ cm}^{-2}$), B ($1 \times 10^{17} \text{ cm}^{-2}$), C ($5 \times 10^{16} \text{ cm}^{-2}$), and D ($2 \times 10^{16} \text{ cm}^{-2}$)	2
Figure 1.2 Schematic energy-band diagrams of Si and GaAs. The top of the valence band lies at $k = 0$ and the minimum of the conduction band is at approximately $0.85X$ along the (001) direction. Thus, direct photon emission is not allowed for silicon. A phonon is needed for the recombination process which might generate an emission.....	3
Figure 1.3. Room temperature PL of a freshly etched layer as a result of partial chemical dissolution in 40% aqueous HF for the times indicated.....	5
Figure 1.4. The surface-to-volume (STV) ratio for a 2D slab, 1D cylinder and 0D sphere where R is the thickness of the slab, radius of the cylinder and radius of the sphere respectively. In all three cases, d represents the thickness of the surface.....	6
Figure 2.1. Simplified schematic diagram and photograph of ion implantation system.....	12
Figure 2.2 Photograph of Nano-D100 sputtering system	14
Figure 2.3 Schematic of the laser pyrolysis reactor	16
Figure 2.4 Typical band structures of direct- and indirect-gap semiconductors	20

Figure 2.5. Band diagram illustrating; radiative recombination, deep level, bound-exiton, auger process (non-radiative recombination).....	21
Figure 2.6. Schematic diagram of photoluminescence set-up.....	22
Figure 2.7. Schematic diagram of TRPL set-up.....	23
Figure 3.1. PL spectra of ion implanted sample with a dose of $1 \times 10^{17} \text{ cm}^{-2}$	26
Figure 3.2. PL spectra of magnetron sputtered sample.....	26
Figure 3.3. PL spectra of as prepared and oxidized powder at 300 K.....	27
Figure 3.4 Luminescence spectra of samples produced by three different methods.....	28
Figure 3.5 PL spectra of a sample which is implanted with Si with a dose of $1.5 \times 10^{17} \text{ cm}^{-2}$ and annealed at various annealing temperatures for 2 h under N_2 atmosphere.....	30
Figure 3.6. PL spectra of SiO_2 film implanted different doses as indicated in the figure.....	31
Figure 3.7. The peak intensity position as a function of fluence.....	32
Figure 3.8. The effect of H_2 passivation on the PL of the Si nanocrystal.....	33
Figure 3.9 Typical normalized decay time measurements of the PL signal around 775 nm for the sample post annealed with H_2 for 1 h. The solid lines are the stretched exponential fit. Data was taken at room temperature.....	34
Figure 4.1. PL spectra taken from 30 to 300 K of ion beam synthesized Si nanocrystals with a broad size distribution. Samples annealed at 1100 °C with nitrogen atmosphere and subsequent annealing performed at 1000 °C with H_2	39
Figure 4.2. P1 and P2 depicted by focusing view of photoluminescence spectra.	40

Figure 4.3. Temperature dependence of the PL peak position for samples with Si implantation doses of $1 \times 10^{17} \text{ cm}^{-2}$	40
Figure 4.4. Temperature dependence of the PL intensity for samples with Si implantation doses of $1 \times 10^{17} \text{ cm}^{-2}$ (diamonds), and $2 \times 10^{17} \text{ cm}^{-2}$, (triangles) respectively. Solid lines are the best fits of data using Eq. 1. In the inset are plotted the activation energies obtained from the fitting procedure.....	41
Figure 4.5. PL lifetime versus inverse temperature of Si nanocrystals and fitting curve with respect to two levels model for sample implanted with a dose of 1×10^{17} . Data was taken at 750 nm.....	42
Figure 5.1. PL spectra of Si nanocrystals obtained from sample I9 at different temperatures.....	46
Figure 5.2. TRPL decays (not normalized to the initial PL intensity) at 300 K for sample I9. The solid line represents the fit of the experimental data to the equation of from, $I(t) = I_0 \exp(-(t/\tau)^\beta)$ where τ is the PL lifetime and β ($0 \leq \beta \leq 1$) is the dispersion exponent.....	47
Figure 5.3. PL decay curves at various low temperatures.....	47
Figure 5.4. Arrhenius plot of the PL lifetime obtained from sample I9 for different wavelengths.....	48
Figure 5.5. Schematically illustration of two levels with τ_L, τ_U and Δ being the lower state (triplet), the upper state (singlet) lifetime and the splitting energy, respectively.....	49
Figure 5.6. PL lifetime versus inverse temperature of Si nanocrystals and fitting curve with respect to two level model for sample I9 at 750 nm.....	51
Figure 5.7. PL lifetime versus inverse temperature of Si nanocrystals and fitting curve with respect to three level model.....	52

Figure 5.8. Schematic diagram of exciton splitting of Si nanocrystals. The measured energies and lifetimes of the excitonic states are presented. The degeneracy of each exciton is shown as X3 (level is 3 times degenerate), etc. An  and an  denote allowed and forbidden states respectively.....	55
Figure 6.1. PL spectra of sample Si155 recorded on as prepared powder and sample Si104A oxidized powder, at 300 K. NdYAG laser, 532 nm, was used as an excitation source.....	58
Figure 6.2. PL spectra of oxidized sample with respect to different temperature.....	59
Figure 6.3. PL spectra of as prepared sample with respect to different temperature.....	59
Figure 6.4. PL emission maxima intensity as a function of 1/T.....	60
Figure 6.5. Wavelength of PL emission maxima as a function of temperature... ..	60
Figure 6.6. Deconvolution spectra for Si104A taken with NdYAG Laser at 300 K. PL spectra are deconvoluted by four peaks and labeled as follows black is Peak 1, red is Peak 2, green is Peak 3, and blue one is Peak4.....	61
Figure 6.7. PL emission maxima intensity as a function of 1/T.....	62
Figure 6.8. Deconvolution spectra for Si155 taken with NdYAG Laser at 300 K. PL spectra are deconvoluted by four peaks and labeled as follows Black is Peak 1, red is Peak 2, Green is Peak 3, and Blue one is Peak 4.....	63
Figure 6.9. PL emission maxima intensity as a function of 1/T.....	63
Figure 6.10. Wavelength of PL emission maxima as a function of temperature.	64
Figure 6.11. PL spectra of oxidized sample with respect to different temperature conducted by HeCd Laser, 325 nm.....	65

Figure 6.12. PL spectra of oxidized sample with respect to different excitation wavelength at 300 K. (NdYAG, 532 nm and HeCd, 325 nm.....	65
Figure 6.13. Deconvoluted spectra for Si104A taken with HeCd Laser at 300 K. PL spectra are deconvoluted by four peaks and labeled as follows Black is Peak 1, red is Peak 2, Green is Peak 3, and Blue one is Peak 4.....	68
Figure 6.14. PL emission maxima intensity as a function of temperature.....	67
Figure 6.15. PL intensity of the emission at 800 nm under continuous irradiation (Ndyag laser) as a function of time.....	68
Figure 6.16. PL recovery intensity of the emission at 800 nm as a function of time	68
Figure 6.17. PL intensity of the emission under continuous irradiation with NdYAG laser as a function of time.....	69
Figure 6. 18. PL intensity of the emission at 744 nm under continuous irradiation (HeCd laser) as a function of time at 50 K.....	70
Figure 6.19. PL intensity of the emission at 775 nm under continuous irradiation (NdYAG laser) as a function of time at 100 K.....	71
Figure 6.20. PL intensity of the emission at 800 nm under continuous irradiation (with respect to NdYAG laser power) as a function of time at RT.....	71
Figure 6.21. PL intensity of the emission intensity as a function of time under continuous irradiation with different laser power.....	72
Figure 6.22. PL intensity of the emission intensity as a function of time under continuous irradiation with different observation wavelength at RT.....	73
Figure 6.23. Schematic illustration of processes involved in the radiative and nonradiative recombination of a single Si nanocrystal.....	74

Figure 6.24. The colored arrows indicate the recombination ways for an excited electron. Green arrows: excitation with photons by using 2.33 eV light . Blue arrows:indirect absorption. Red arrows: indirect radiative recombination (with the assistance of a phonon). Black arrow: Auger recombination. Orange arrows: nonradiative recombination mechanism.....	76
Figure 6.25. The Raman spectra of as-grown and annealed sample for a Si/SiO ₂ superlattice.....	77
Figure 6.26. Raman spectra of the as-prepared and oxidized free-standing Si nanocrystals.....	79
Figure 6.27. Deconvolution of Raman spectra for oxidized free-standing Si nanocrystal.....	80
Figure 6.28. Raman spectra of the laser induced oxidized free-standing Si nanocrystals.....	81
Figure 6.29. The HRTEM image of free-standing nanopowders containing Si nanocrystals. a) agglomerated free-standing Si nano particles., b) Si-nc with diameter ~5 nm, c) Si-nc with diameter ~3 nm.....	85

LIST OF ABBREVIATIONS

CCD	Charge-coupled device
ESR	Electron Spin resonance
EDS	Energy-dispersive X-ray spectrometer
GaAs	Gallium Arsenide
HeCd	Helium Cadmium
He-Ne	Helium Neon
NdYAG	Neodymium-doped yttrium aluminium garnet
PL	Photoluminescence
QC	Quantum confinement
SEM	Scanning Electron Microscope
Si	Silicon
Si nc	Silicon nanocrystals
STEM	Scanning transmission microscopy
TRPL	Time-Resolved Photoluminescence
TEM	Transmission electron microscopy
UV	Ultraviolet

CHAPTER 1

INTRODUCTION

1.1. Motivation

Silicon (Si) is one of the most known and used materials in microelectronic [1] and solar cells [2] industries. It has excellent electronic properties but very poor light emitting capabilities because of its indirect bandgap nature [1, 2]. The idea of turning silicon into an efficient light emitting material has fascinated lots of scientist since the discovery of visible room temperature light emission from porous silicon two decades ago [3]. During these last years, the use of nanometric sized Si particles embedded in oxide matrices has emerged as the most promising way to obtain high emitting efficiency from silicon [4, 5]. In those structures, the quantum confinement and the carrier localization [6, 7] contribute together to the improvement of the optical properties of the material while the presence of the oxide matrix ensures the long time optical stability suited for the application in commercial devices. At the same time, the matrix and production technique influences the recombination mechanism in silicon nanocrystals and this complicates the understanding of their physics. Figure 1.1 shows the photoluminescence spectra of Si nanocrystals formed by ion implantation fabricated in our laboratories [8]. This example shows that the PL peak shifts to lower energy values with increasing implantation dose. This is clear evidence for the quantum size effect occurred in the nanocrystals as an increase in the energy levels with decreasing the size of the quantum dot. The aim of the thesis

thesis is the experimental investigation on the luminescence properties of silicon nanocrystals and search for the physical explanation of the observed light emitting phenomena.

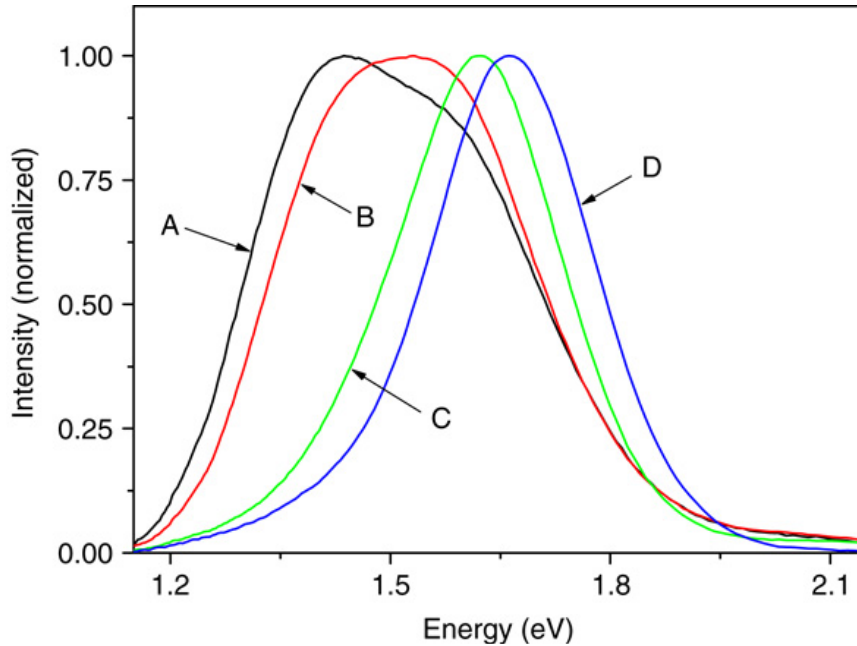


Figure 1.1. Photoluminescence spectroscopy of sample implanted with different dose ^{28}Si into SiO_2 substrate. Sample labels (Si ion dose) are A ($1.5 \times 10^{17} \text{ cm}^{-2}$), B ($1 \times 10^{17} \text{ cm}^{-2}$), C ($5 \times 10^{16} \text{ cm}^{-2}$), and D ($2 \times 10^{16} \text{ cm}^{-2}$) [8]

1.2. Si Nanocrystals as a new light emitting structure for Si-based technology

Silicon, as one of most abundant element on earth having good mechanical and electronic properties, has become the major material of the semiconductor and photovoltaic industry and seemingly will remain dominant in the foreseen future. Si is a semiconductor whose electrical conductivity can be controlled over a wide range, its oxidized state (SiO_2) is one of the best stable electrical insulator and its chemical and mechanical properties make silicon the ideal material for advanced materials and device applications. For all these reasons, silicon became the most important player in electronic integrated circuits, solar cells, communication devices, being the basic building structure of most electronic devices, from transistors and diodes to microprocessors, and more [1]. Because Si is not an

optically active element, and thus a poor light emitter, it is not a good choice for photonic applications. The reason is the indirect bandgap characteristics of silicon, meaning that the energy's minima of the conduction and the valence bands do not fall at the same wavevector value. The situation is illustrated in Figure 1.2 where the energy-band diagram of silicon is shown and compared to Gallium Arsenide (GaAs), which is a direct bandgap semiconductor.

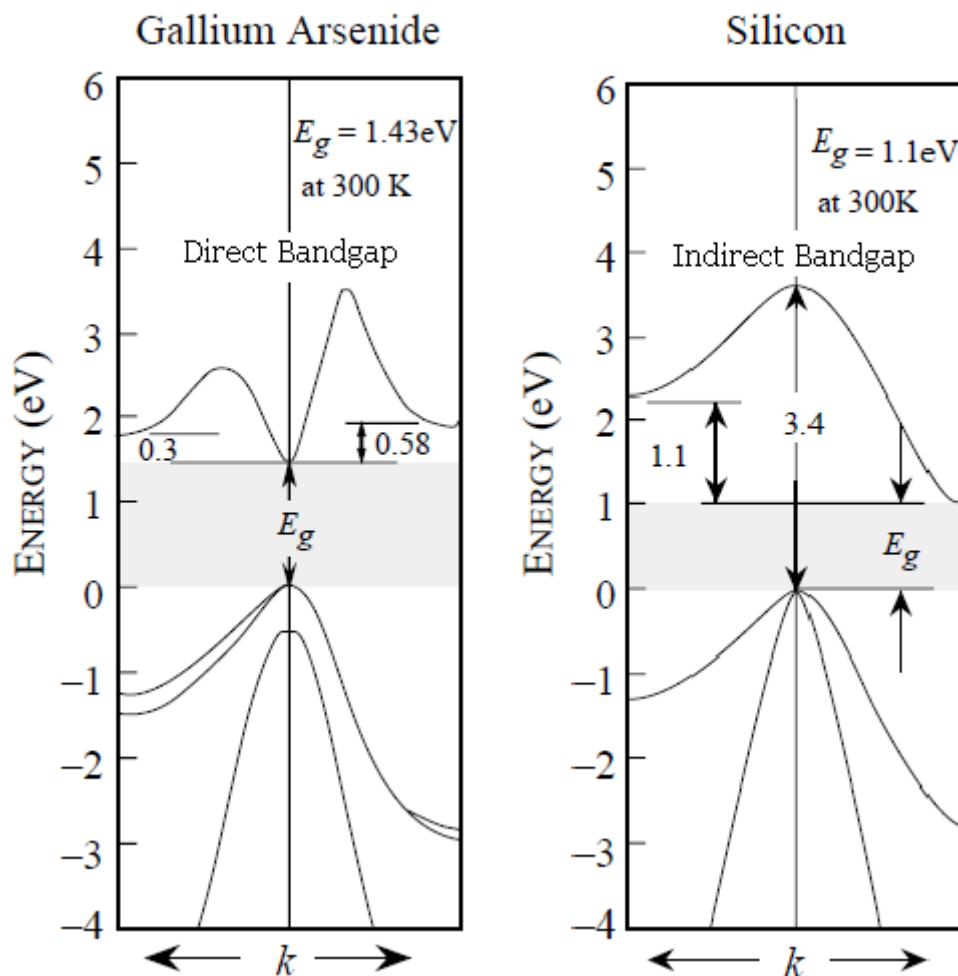


Figure 1.2. Schematic energy-band diagram of Si and GaAs. The top of the valence band of Si lies at $k = 0$ and the minimum of the conduction band is at approximately $0.85X$ along the (001) direction. Thus, direct photon emission is not allowed for silicon. A phonon is needed for the recombination process which might generate an emission [9].

For steady state, electrons occupy the lowest energy states of the conduction band while holes occupy the upper states of the valence band. Electrons drop down to empty states of holes in the valence band, giving their energy in the form of a photon when the recombination happens radiatively the energy of the photon is given by $\hbar\omega = E_c - E_v = E_g$, where E_g is the bandgap energy of the semiconductor and $\hbar\omega$ is the photon energy. Energy and momentum should be conserved during the process. In direct bandgap semiconductors like GaAs, the radiative recombination can take place easily as both the electrons and the holes have the same momentum at the center of the Brillouin zone (Γ -point in figure 1.2). In Si, the momentum mismatch between electrons and holes does not allow direct radiative recombination unless with the help of a phonon which is involved in the recombination process. This requirement reduces the probability of radiative emission significantly. Therefore, silicon is a poor light emitter that cannot be used for optoelectronic applications. This property of silicon is considered to be a disadvantage in the optical community. On the other hand, for direct bandgap semiconductors, the radiative recombination is a fast process which is in the order of few nanoseconds. Silicon has a slow radiative lifetime (of the order of few milliseconds in pure silicon [1]) which allows the minority carriers to diffuse over large distances (few hundreds of micrometers) and this property of Si is very favorable for electronic applications.

When the size of Si crystal is reduced the optical and electrical properties changes substantially. New functionalities that might be very useful in various applications may emerge. Generally, nanostructures are thought as a material whose dimension can be shrunk down [10, 11] to the nanometer length scales in one or more dimensions. Nanostructures are classified upon their dimensionality, for instance, two-dimensional (2D) quantum wells, one dimensional (1D) nanowires and zero-dimensional (0D) nanocrystals. The most important consequence of the dimensional shrinkage to nanoscale is the new quantum phenomena induced in the crystal due to the size effect. A key effect induced by the size effect is the

modification of the energy levels and the density of states of the charge carriers. Quantum confinement (QC) of charge carriers or excitons occurs when the sizes of the volume is comparable to the De Broglie wavelength. The momentum conservation law relaxes with the decreasing size of the object. For silicon nanostructures case, for example a silicon nanocrystal of radius – R, we can use the Heisenberg uncertainty principle to predict the wavevector relaxation: $\Delta k \sim 1/R$. While the wavevector conservation law increases with the decreasing size of the nanostructure, one can estimate the radiative recombination rate to substantially increase when the wavevector mismatch, illustrated in figure 1, becomes comparable to Δk , causing to raise the question: can we produce the active photonic elements [12, 13] from silicon nanostructures?

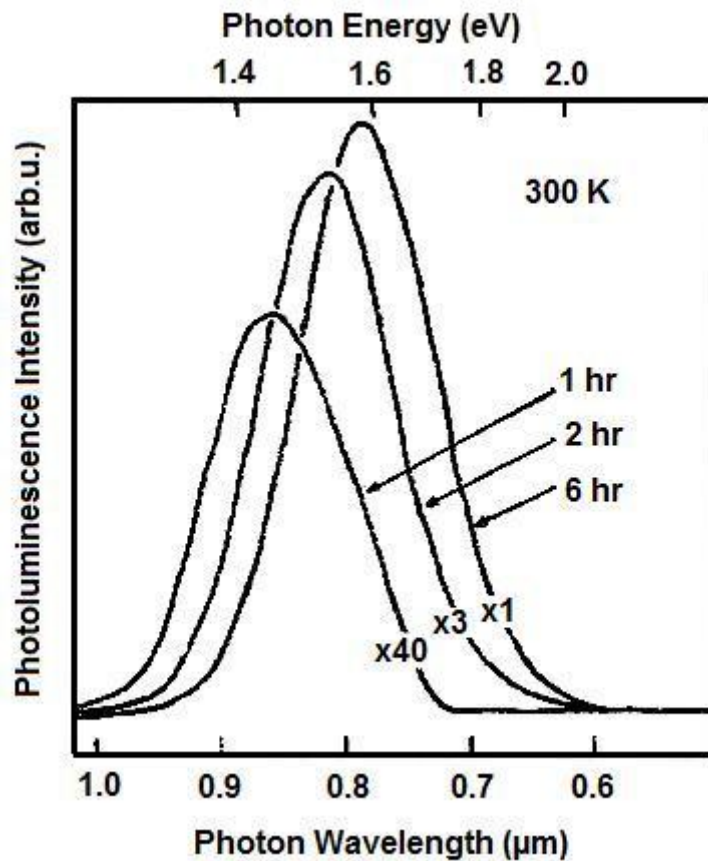


Figure 1.3. “Room temperature PL of a freshly etched layer as a result of partial chemical dissolution in 40% aqueous HF for the times indicated.” (From ref [14])

The idea of generating active photonic element from Si nanocrystals became a reality in 1990 when Canham [14] reported on efficient red light emission from porous silicon exposing UV light source. Figure 1.3 shows a typical spectrum of the photoluminescence (PL) of porous Si which is a nanometric random network of pores. Canham suggested that quantum size effects might be responsible for the efficient PL. There are two evidences which seem to support this conclusion. The first one is the presence of small crystalline silicon nanostructures, in the PS medium [3]. The substantially blue-shift of the maximum PL energy is the second indication of quantum confinement in small nanostructures [10]. After this pioneering study, many groups have focused to verify the quantum confinement model with a variety of experimental and theoretical studies. Most of these studies provided support to quantum confinement model [15], while a remarkable number of works have reported results of the PL that cannot be explained by the quantum confinement picture only [16]. To understand of this puzzle, researchers have tried to propose alternative models such as those including surface phenomena that can generate the observed PL spectra [7, 17]. In these approaches, radiative transitions are attributed to the surface of the nanostructures either due to surface bonds, surface defects, imperfections or even surface molecular species [18].

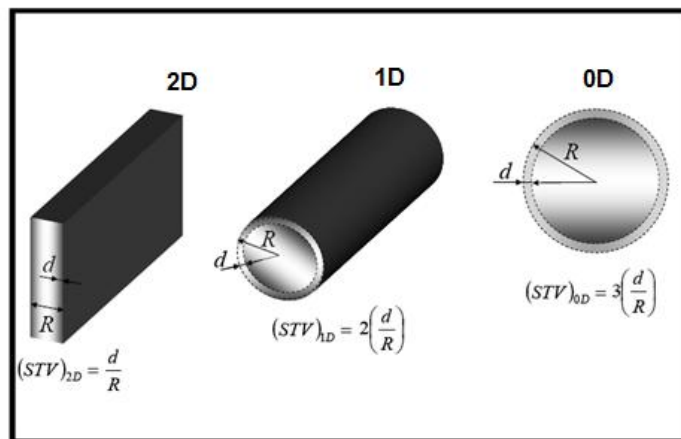


Figure 1.4. The surface-to-volume (STV) ratio for a 2D slab, 1D cylinder and 0D sphere where R is the thickness of the slab, radius of the cylinder and radius of the sphere respectively. In all three cases, d represents the thickness of the surface.

Obviously surface phenomena are expected to play a significant role in nanostructures. To clarify this effect, let us consider the surface to volume ratio for nanostructures which have different geometrical form such as spheres (0D), cylinders (1D) and slabs (2D) as pictured in figure 1.4. In order to define a volume of nanostructure surface, one can estimate the surface thickness of nanostructure, d . For silicon, one may take $d \sim 1$ nm to estimate of the surface's thickness. Therefore, for a 0D nanocrystal one can find, surface to volume ratio = $3(d/R)$, where R is the radius of the sphere. For $R=6$ nm and $R=12$ nm nanocrystals one may get, surface to volume ratio ~ 0.5 , meaning that 50% of the silicon atoms belong to the surface, and ~ 0.25 , meaning that 25% of the silicon atoms sit on the surface of the nanocrystal, respectively. One can then conclude that surface phenomena become more significant with the decreasing size of the nanostructures and this should be taken into the account to explain the electronic and optical properties of the nanostructures. It is clear that, porous Si is not the ideal structure to study the quantum confinement and surface related phenomena because of its randomly network pores and related uncertainties. In addition, PS is not chemically and mechanically stable and shows aging effects [17]. For these reasons, the QC and the surface chemistry models could not be tested with PS. Over the last decade, researchers have concentrated on Si nanostructures to fabricate with different techniques and better capabilities to control their size, shape and the host matrix [19]. With improvements in the production techniques and knowledge accumulated through many studies, it is now possible to investigate the evolution of optical and electrical properties of silicon nanostructures versus size and dimensionality. According to recent experimental results [20-23], a refined comprehensive model can be developed by taking into account both quantum size effect and surface phenomena to explain the whole optical properties of Si nanostructures. M. Dovrat et al. [21] have made contribution to luminescence phenomena of Si nanocrystals. They proposed that the environment of the nanocrystals and the macroscopic properties of the medium effect the lifetime of the lower triplet state and the dispersion exponent.

“The exclusion of non-radiative channel” [21] in the crystals is assigned the origin of the efficient photoluminescence.

Recently, S. Godefroo et. al. were performed Electron Spin resonance (ESR) and magneto-PL experiments [23] to determine the origin of the PL from Si nanocrystals embedded in SiO₂. ESR analysis shows that numerous defects which are non-radiative recombination centers placed between the Si nanocrystals and the surrounding SiO₂ are exist. None of these defects measured by ESR is PL active. Nevertheless, this demonstrates that the observed PL is not from QC effect and defects. So as to determine the origin of the luminescence, PL measurements were taken in the pulsed magnetic field up to 50 T. In the high magnetic fields free exciton of nanocrystals are expected to show blue shift, whereas localized excitons are not expected to show a blue shift. The authors have observed very small shift and conclude clearly the PL stem from highly localized defect states. After the passivation of defects in the sample with hydrogen, ESR and PL measurements were repeated. ESR shows that the defects have been removed; therefore PL signal has increased which shows that the origin of the PL is QC effect after the passivation. Using the UV light source (Ar⁺ laser), the defects can be reintroduced. The UV illumination has reversed the effect of the passivation and the PL is defect-related origin. As a result, the authors show that the origin of PL can be classified by using high magnetic field as either from QC or defects and the controllability of the origin of the PL with the help of hydrogen passivation and UV irradiation.

1.3. Thesis Structure

The purpose of this thesis is to investigate luminescence properties of Si nanocrystals in different environment and to understand the basic physical mechanisms behind light emission from Si nanocrystals. This thesis is organized in 7 chapters. Experimental techniques used in this work are briefly explained in Chapter 2. The photoluminescence spectroscopy of Si nanocrystals is discussed depending on annealing temperature, implantation dose and H₂ passivation in Chapter

3. Chapter 4 investigates the light emission from Si nanocrystals in the temperature range from 10 K to 300 K considering temperature, implantation dose. Decay time dynamics of Si nanocrystals is studied in Chapter 5 by using excitonic model. Photoluminescence properties of free standing Si nanocrystals in powder form, produced by laser pyrolysis technique, are investigated in Chapter 6. Chapter 7 summarizes the conclusion of this thesis and discusses possible directions for future work.

CHAPTER 2

EXPERIMENTAL

2.1. Sample Preparation Methodology

2.1.2. Ion Implantation

Silicon nanocrystals can be produced by a variety of techniques including ion implantation [24-28], sputtering [29, 39], laser pyrolysis [31, 32], chemical vapor deposition [33, 34] and reactive evaporation of silicon-rich oxides [35, 36]. Among these fabrication techniques ion implantation is a well known doping technique in VLSI processing.

In the ion implantation procedure, ions are extracted from a plasma and accelerated by an electric field to the sample. The ions impact with sufficient energy (with the energy range from keV to MeV) to travel some distance into the sample before they come to rest. The total dose of implanted ions is controlled by monitoring the integrated current as the ion beam is rastered over the sample. An implanted layer can be created with good uniformity by the this way. Ion implantation also provides control over the excess Si depth distribution by the choice of acceleration energy. The nature of the ion stopping process result in a Gaussian Si distribution, which results in a broad size distribution of nanocrystals. So the mean nanocrystal size is depth dependent with smaller nanocrystals formed at the concentration tails. Nevertheless this synthesis method provides a simple and flexible approach to nanocrystal synthesis and it is well suited to experimental investigation of nanocrystals and their properties. Implantation causes structural defects in SiO₂, which can quench the nanocrystal luminescence or exhibit luminescence themselves. In order to get more stable luminescent from Si

nanostructures high temperature annealing should be employed above 1000 °C [37].

As mentioned above some samples investigated in this thesis were synthesized by ion implantation. Ion implantation experiments carried out with Varian DF4 ion implanter that allow the ion energy from 5 to 200 keV. A schematic diagram of ion implanter is shown in figure 2.1. In general, the ion implantation system consists of three units; source, beam line and end station. For pumping all these regions the diffusion and mechanical pumps are used. High vacuum is needed for ion implantation which should be around 1×10^{-7} Torr.

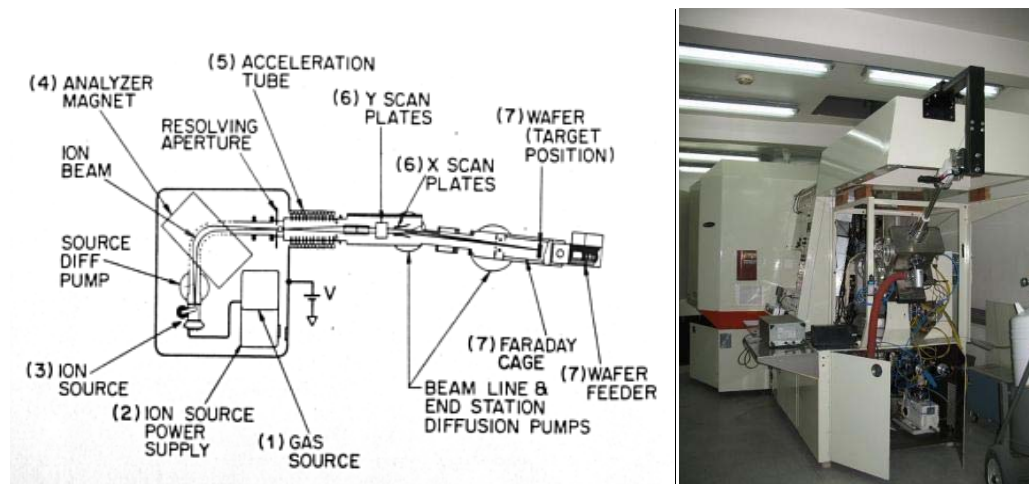


Figure 2.1. Simplified schematic diagram and photograph of ion implantation system [38]

2.1.2. Magnetron Sputtering Deposition Technique

The momentum transfer of ions to the target material is the basis of magnetron sputtering deposition technique. When atoms of the sputtering gas, commonly argon, hits to the surface of the target, momentum transfer occurs by generating free atoms to be deposited on the substrate [39]. “Accelerated, away from the negatively charged electrode (cathode), “free electrons” approach the outer shell electrons of neutral gas atoms in their path. This process leaves the gas atom

electrically unbalanced since it will be more positively charged protons than negatively charged electrons. Therefore it is no longer a neutral gas atom but a positively charged "ion" (e.g. Ar $+$). After that the positively charged ions are accelerated into the negatively charged electrode (a.k.a. "cathode") striking the surface, "blasting" loose electrode material and more free electrons by energy transfer. The formation of ions and the continuation of the plasma are kept by additional free electrons. These free electrons go back into the outer shells of the ions by changing them neutral gas atoms. When these electrons return to a ground state, the resultant neutral gas atom gain energy and release that same energy in the form of a photon (due to the laws of conservation of energy). The releasing of these photons is the reason why the plasma appears to be glowing. Sputtering deposition occurs after the medium get high vacuumed (1×10^{-6} Torr)" [40]. The gas pressure is set low to increase the rate during deposition. There are many other factors that affect the sputtering process. More knowledge about the sputtering can be found A. S. Alagöz Ms thesis in Ref [41].

There are several sputtering methods; the most general ones are DC and RF sputtering techniques. While DC sputtering is very effective for the conducting targets, RF sputtering can be used to avoid the charging if non-conducting targets are needed to be sputtered. In this thesis Nano D100 the sputtering set up was used produced by VAKSIS Ltd. The system has 3 circular independently controlled magnetrons. One of them is connected to 600 W 13.56 MHz RF supply, other two are 500 W and 1 kW DC supplies. High purity argon gas was used as the sputtering gas. Gas flow and chamber pressure of the gas is controlled electronically from a control panel.



Figure 2.2 Photograph of Nano-D100 sputtering system.

2.1.3. Preparation of Free Standing Nanocrystals by Laser Pyrolysis Technique

The samples used in this work were prepared by laser pyrolysis technique at ENEA, Italy, by Prof. Dr. E. Borsella's group [42].

Production of wide variety of pure, crystalline, nearly mono-disperse and disagglomerated nanopowders is very difficult. Lots of variables influence nanoparticle properties, and among these are size, shape, crystal structure, and surface chemistry. In this respect laser pyrolysis technique is highly versatile method for the production of nanopowders of including materials such as Si, SiC Laser pyrolysis technique is described and reviewed in detail in references [43-46]. "In this production technique, particle nucleation and growth occurs as a result of collisions between radicals produced by laser induced dissociation of gas-phase precursors, i.e. SiH₄ [42]". To heat the gas molecules a laser (usually CO₂ laser) is used as an optical heat sources. The advantages of this heating technique are free from contamination, good and uniform process control and absence of hot surfaces. Nanopowders (i.e. Si) are synthesized with respect to the

gas-phase reactions by using NH_4 and C_2H_4 . Because of SiH_4 has strong absorption near $10.6 \mu\text{m}$, it is chosen as a synthesizer. Therefore, the CO_2 laser absorption measurements are directly available for NH_4 and C_2H_4 . “The produced nanopowders consist of aggregates of nearly monodispersed primary particles. These aggregates can be either soft or hard agglomerates. Both the particle size and the degree of agglomeration are determined by the residence time of the particles in the laser irradiation region, which can be adjusted by changing the synthesis parameters. However, it is not possible to obtain PL from raw pyrolytic powders, since the interaction of surface termination and crystalline core dimension [42]”. To overcome this problem lots of studies have been performed [47, 48]. In 1999, Huisken et al. reported significant PL response upon oxidation and etching their product with HF [49]. Thermal oxidation, acid etching and wet-chemical oxidation reaction treatments is also used to get a strong photoluminescence from pyrolytic powders [50-53]. “In order to produce luminescent and disaggregated small nanoparticles, the role of the reaction sensitizer and of the quenching collection system on the synthesis of very small nanoparticles has been studied by E. Borsella group [42]”.

Experimental setup is shown in figure 2.3. High power continuous wave (cw) CO_2 laser ($10.6 \mu\text{m}$) was used as a heat source. As shown in figure, a cw CO_2 laser is focused to the reaction chamber by two coaxial nozzles with help of a ZnSe lens. SiH_4 is chosen as a reactant gas because SiH_4 has strong absorption near $10.6 \mu\text{m}$, SiH_4 absorption is strong function of pressure and strongly depend on laser intensity. “The SiH_4 reactant gas enters though the inner tube. For Si 155, a collector was introduced in the chamber and mounted on the upper part of the chimney at $h=1 \text{ mm}$ distance from the laser beam. The gas mixture together with the particles passes through the hole and then it is suddenly expanded to lower the temperature. In order to produce homogeneous suspensions, the as-prepared powders were first dispersed in methanol at a typical concentration of 1 g/L using a low-power ultrasonic bath treatment for 60 min. A second ultrasonic treatment

using a high-power ultrasonic probe (BRANSON sonicator equipped with 3 mm micro-tip probe) was applied for 30 min to induce disaggregation. In scheme 1A, free-standing Si nanocrystals obtained from laser pyrolysis technique is shown schematically [42]”.

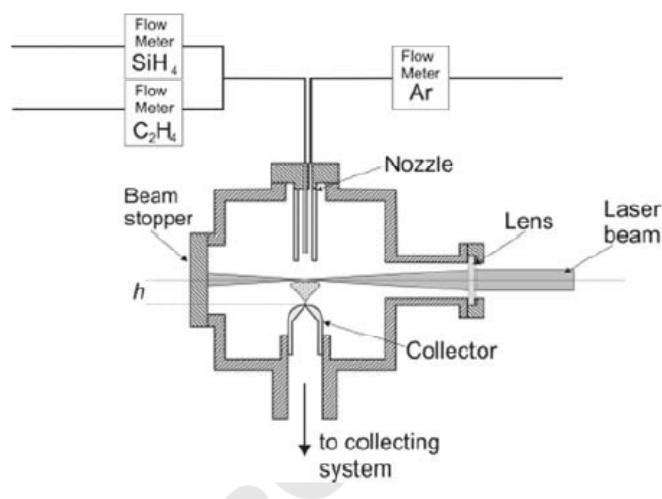


Figure 2.3. Schematic of the laser pyrolysis reactor [42].

“Typical oxidation was performed for sample Si104A by using hydrogen peroxide in alkaline ambient. The oxidation processes is as follows: Row powders were first dispersed in CH₃OH at c = 2 g/L with the help of ultrasonic bath, then deionized H₂O (CH₃OH:H₂O = 1:1) and finally H₂O₂ and NH₄OH (molar ratio Si:H₂O₂:NH₄OH = 5:1:1) were added. The suspension was warmed at 60 °C for 1 h, which is useful to activate the reaction, and then oxidation continued at room temperature for 5 days. The dry powders were obtained by centrifugation or evaporation of solvent and then washed several times with CH₃OH [42]”.

2.2. Sample Details

2.2.1. Thermal Annealing

In this work thermal annealing was used to precipitate the excess Si in to nanocrystals, and to remove defects caused by ion implantation and sputtering. An appropriate combination time and temperature is needed. Thermal annealing was carried out in a conventional horizontal single zone quartz tube furnace under flowing N₂ and 5% H₂ in N₂. Different annealing temperatures were used to get different sized Si nanocrystals in the SiO₂ matrix. After implantation samples annealed at 1100, 1050, 1000 and 900 ° C for 1 hour in either N₂ or 5% H₂ in N₂.

2.2.2. Samples

In this thesis samples were produced by three different production techniques; ion implantation, magnetron sputtering and laser pyrolysis. And subsequent annealing procedures were performed for various temperatures. Samples used in this thesis were produced by Assoc. Prof. Dr. Uğur Serincan, Mustafa Kulakçı, Arif Sinan Alagöz and Prof. Dr. E. Borsella groups [42] at ENEA in Italy. Physical conditions of the samples used in this thesis are given in the below tables.

Table 2.1. Ion Implantation conditions of samples.

Production Tech.	Ion Energy (keV)	Ion Dose(cm^{-2})	Annealing Tempt.($^{\circ}\text{C}$)	Annealing Time (h)
Production Tech.	100	1×10^{16}	1050	2
	100	2×10^{16}	1050	2
	100	5×10^{16}	1050	2
	100	1×10^{17}	800	2
Ion Implantation	100	1×10^{17}	900	2
	100	1×10^{17}	1050	2
	100	1×10^{17}	1050	5
	100	1.5×10^{17}	1050	2
	100	2×10^{17}	1050	2
after N_2 annealing Post annealing conditions with H_2	100	1×10^{17}	300	1
	100	1×10^{17}	400	1
	100	1×10^{17}	500	1
	100	1×10^{17}	600	1
	100	1×10^{17}	1000	1

Table 2.2. Sputtering parameter of samples.

Production Tech.	Si Target Power (Watt)	SiO_2 Target Power (Watt)	Annealing Tempt.($^{\circ}\text{C}$)	Annealing Time (h)
Sputtered	70	350	1100	3

Table 2.3. Laser Pyrolysis properties of samples.

Production Tech.	Sample name	Chemical Oxidation
Laser Pyrolysis	As prepared	no
	Oxidized	yes

2.3. Sample Characterization

2.3.1. Photoluminescence Spectroscopy

Optical spectroscopy has become a useful and popular characterization tool since the invention of the laser and detection techniques. Thus, the optical spectroscopy has flourished and improved with the help of monochromatic, powerful, tunable, pulsed or continuous wave lasers and detection systems. Another factor which makes optical spectroscopy as a unique characterization tool is rapid evolution of results.

Emission processes can be classified according to the source of excitation. Electroluminescence is an emission process by using an electric current. Electron beam excitation results in cathodeluminescence. Excitation by a thermal process is called thermoluminescence. Light emission during a chemical reaction is called Chemiluminescence. If the luminescence continues after switched off the light source, this luminescence is called Phosphorescence. PL is a light emission process which result in optical excitation and it is used for the characterization of dynamical systems in materials. PL is a spectroscopic method based on measuring the energy of emitted photons. The optical emission properties and efficiencies, composition and impurity content of materials can be obtained by using photoluminescence spectroscopy. In order to investigate properties of the materials, the energy distribution is analyzed. PL spectroscopy for material characterization is preferred by scientists due to easy availability and simplicity of the system, with no destruction for samples and no need of sample preparation before experiment, etc. In order to describe the preference of PL, some fundamental knowledge of semiconductors will be reviewed such as semiconductor band structure, free-carrier properties, recombination processes, etc. The bandgap and the momentum difference of semiconductors is the crucial quantities for identifying materials. When the momentum difference is nonzero the semiconductor is called an indirect-gap semiconductor and if the momentum

difference is zero, it is termed direct semiconductor. The typical dispersion relations for direct-gap and indirect-gap semiconductors is depicted in figure 2.4. The band gap characteristic of materials, the relative intensity and temporal response of light emission play important role to examine the recombination dynamics of semiconductors [54].

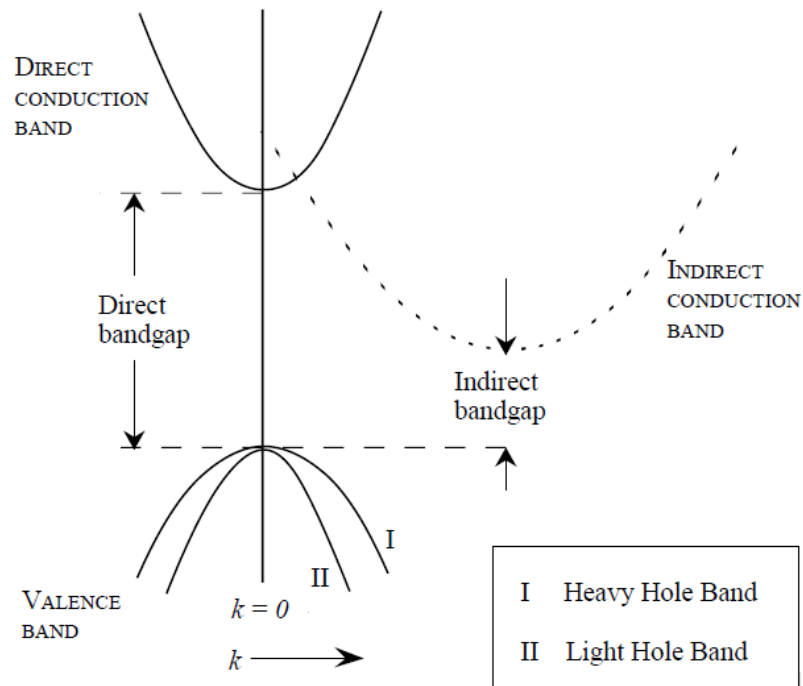


Figure 2.4 Typical band structures of direct- and indirect-gap semiconductors [55].

Electron and holes are the free carriers in semiconductors. Electrons and holes generally are defined by their origin (free or defect related), density, mass, etc. At low temperature the many-particle states may be formed in addition to the single-particle states. An excitons, biexcitons, excitonic molecules, electron-hole plasmas and liquids are the some kind of many particle states. Excitons are the coulomb correlated electron-hole pair. Biexcitons and excitonic molecules consist of two or more excitons bond by van der Waals binding. High density phase of Coulomb correlated electron and hole is defined by electron-hole plasma. The electron-hole liquid occurs only at low temperature and it is a condensed state. If

these many particles recombine by emitting photon, this is called radiative recombination. The recombination is termed non-radiative recombination while the recombination occurs through phonon participation [54]. There are many possible recombination mechanisms; a few of them are illustrated in figure 2.5.

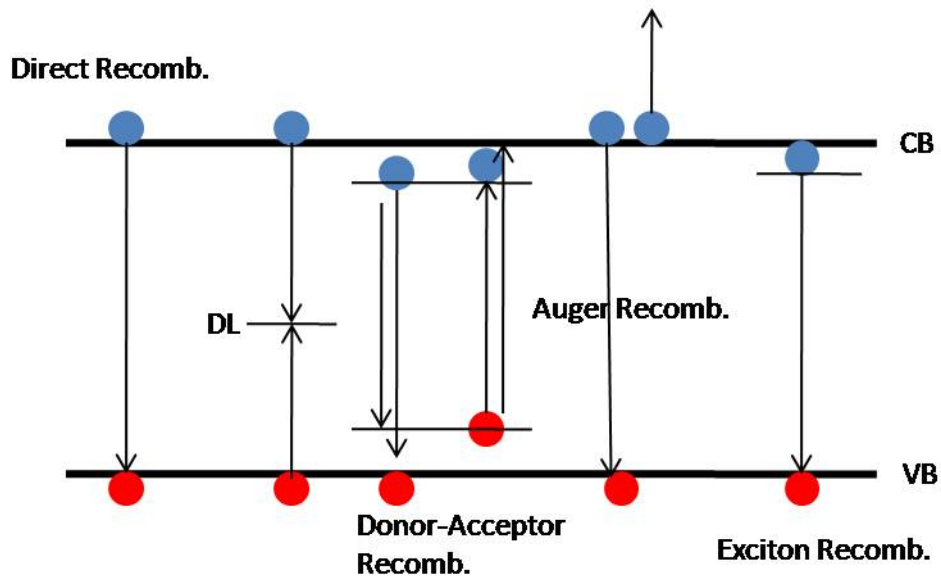


Figure 2.5. Band diagram illustrating; radiative recombination, deep level, exciton, auger process (non-radiative recombination).

If an electron falls from conduction band into the valence band, this process is called band to band recombination. For this emission electron should have energies equal to or greater than the bandgap. For the free-to-bound transitions case, free electrons and holes may become bound by Coulomb interaction. There are two kind of free-to-bound transitions: donor-to-valence band and conduction band-to-acceptor. If the free carrier involve to the radiative recombination bounding to an impurity, this emission is called Donor-acceptor pair recombination. This recombination processes occurs at energies less than the bandgap. This recombination occurs below the bandgap. In Auger recombination, the emitted energy is given non-radiatively to another particle such as electron. The spectral sign of the recombination mechanisms mentioned so far are useful in

identifying the variety of recombination of materials. Additionally, indirect recombination occurs by involving the emission of phonon(s) and a photon. For indirect gap materials, conduction band minimum and valence band maximum has a different the k value. Since the absorbed photon's wave vector is so small to reach the conduction band, a phonon has to be absorbed or released for electron. The possibility of this process is weak which means that indirect gap materials are not good light emitters [54].

As mentioned above, photoluminescence is processes in which excitation photons are absorbed to create electron-hole pairs, which subsequently relax to the energy minima's and then recombine to yield secondary photons characteristic of the materials electronic structure. The principal components used in a PL experiment are a laser source for excitation, a monochromator for spectroscopy, and a photomultiplier or CCD camera for detection as shown in Figure 2.6.

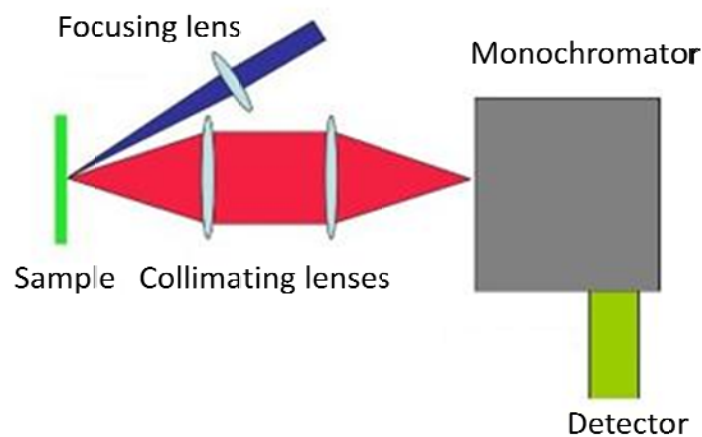


Figure 2.6. Schematic diagram of photoluminescence set-up.

A collimated laser source is directed to a focusing lens which focuses the laser onto the sample. The primary reflection is directed away from the detecting system to avoid overloading the monochromator. The sample luminescence is

focused by collimating lenses and filtered by notch filter to remove laser line from the spectrum. The final output signal is detected by CCD. The excitation source is typically a laser, such as Ar ion (488 nm, 514.5 nm), NdYAG (532 nm), HeCd (325 nm) laser. In this thesis we used all of these lasers as an excitation sources.

2.3.2. Time-Resolved Photoluminescence

TRPL provides information of the excited state of a material by a time dependent measurement. It is a powerful tool for investigating energy and charge transfer processes. To obtain spectral and temporal information from materials there are lots of techniques. The most commonly used technique is the time-correlated single-photon counting. Short pulsed laser sources, which can be spectrally tuned, are used in TRPL experiments. A typical time-resolved PL experimental setup is shown in the Figure 2.7. The PL signal from the sample is collected and focuses on monochromator. Some part of the incident laser beam is directed and focuse to delay unit. The signal is detected with a high sensitive single photon counting unit.

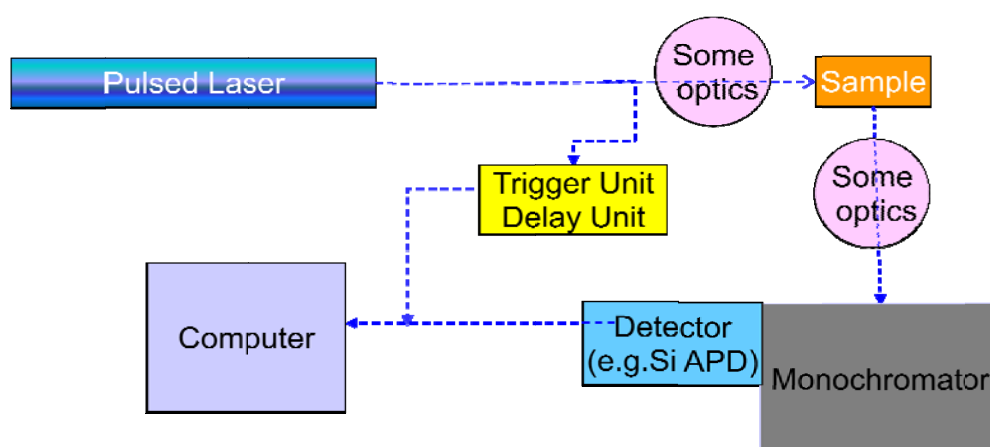


Figure 2.7. Schematic diagram of time-resolved photoluminescence set-up.

TRPL measurements were performed using frequency-doubled yttrium-aluminum-garnet (YAG) laser (532 nm). The repetition rate was 50 Hz. The emitted PL was dispersed by HR460 Jobin Yvon monochromator and detected by a cooled InGaAs photomultiplier tube. PL transients were stored and averaged by

SR400 photon counter and a SR430 Multichannel Scaler- Stanford Research Systems.

2.3.3. Raman spectroscopy

Raman scattering spectra were taken on a confocal micro-Raman (HR800, Jobin Yvon), attached with Olympus microanalysis system and a charge-coupled device (CCD) camera providing a resolution of $\sim 1 \text{ cm}^{-1}$. The spectra were carried out in backscattering geometry with the 632.8 nm line of He-Ne laser at room temperature.

2.3.4. Transmission Electron Microscopy (TEM)

The structural and compositional characterization by transmission electron microscopy (TEM, JEOL 2100 F) has been performed with a field-emission gun (FEG) microscope operating at 200 kV equipped with an EDAX energy-dispersive X-ray spectrometer (EDS) and a Gatan STEM controller for performing scanning transmission microscopy (STEM). The probe size is under 0.5 nm. Concerning the TEM specimen preparation, the Si-np are dispersed in toluene, grinded in agate mortar and then treated in an ultrasonic bath for a few minutes in order to reduce the dimensions of the powder aggregates. Then, some drops of the solution containing the nanopowders are deposited onto the holey carbon film supported by a metal grid (lacey carbon film on 300 mesh copper grid, by TAAB): after evaporation of the solvent, the samples on the grids are analyzed in the TEM.

CHAPTER 3

PHOTOLUMINESCENCE SPECTROSCOPY OF Si NANOCRYSTALS in SiO₂

3.1. Introduction

Today's microelectronic industry is based on Si [14]. Si is widely available, highly purified, and has excellent thermal and mechanical properties. Moreover the natural oxide of silicon (SiO₂) is a good insulator. However concerns about continuing success of microelectronics industry related to fundamental and processing aspects have been raised in recent years [5, 56]. An important example is related to the limitation of the operating speed of microelectronic device. A possible solution of this problem is the use of optical interconnection. This is main driven forces behind Si optoelectronics [19]. However, Si has poor light emitting capabilities because of its indirect bandgap nature [57]. The discovery of visible room temperature light emission from porous silicon has fascinated scientist to obtain high emitting efficiency from silicon nanocrystals. During last two decades the origin of light emitting center have been studied from many groups and a consensus has been reached that highly localized defects at the interface and the quantum confinement of excitons both play important roles, but it is difficult to experimentally distinguish the mechanisms in the radiative emission [58-59]. This chapter presents results of the experimental investigation of the influence of production techniques, annealing temperature, implantation dose, and H₂ passivation on the optical properties of silicon nanocrystals.

It is worth nothing that the oxide matrix can have a fundamental influence on the development process of embedded nanocrystals.

In fact, the growth of Si-nc in an insulating matrix is always obtained by the separation of a Si rich material into Si and oxide phases. This process is typically driven by the energy supplied by a high temperature annealing treatment that turns the meta-stable Si rich phase into a stabilized material. The characteristics of the resulting composite depend on the thermodynamic properties of the initial material, the supplying energy (annealing temperature) and the annealing time; the first two being the most important. In fact, recent studies [22, 60-65] have demonstrated that the Si aggregation process is extremely rapid (few seconds) at temperatures higher than 1000 °C. This indicates that the annealing time does not limit the Si-nc development process and that long time (hours) treatments are necessary only for the improvement of the optical quality of the matrix (non-radiative defects passivation). The values of the annealing temperature needed to develop well passivated, crystalline particles of the desired size can be different for different samples because of the difference in the composition of the starting material.

In this chapter, an overview of the origin of photoluminescence from Si nanocrystals is represented taking into account different influence parameters. Clearly, one can say that it is difficult to determine the origin of PL from Si nanocrystals. It can be either localized defects at the Si/SiO₂ interface, quantum confinement of excitons or both of them. A worldwide research effort has been devoted to the understanding of the origin of the PL from Si nanocrystals.

3.1. PL, Influence of using different production techniques.

In this section, the photoluminescence properties of Si nanocrystals prepared by different fabrication techniques are presented. In Chapter 2, the main features of standard magnetron sputtering, ion implantation and laser pyrolysis techniques are presented. Firstly, the PL property of Si nanocrystals (nc) obtained by Si implantation in SiO₂ is analyzed. Secondly, the differences between the emissions from the nanocrystals deposited by different sputtering processes are thoroughly studied. And finally, the results for Si-nc formed using laser pyrolysis are presented. The photoluminescence measurements were performed with the 532

nm line of an NdYAG laser with an intensity of $\sim 0.7 \text{ W/cm}^2$. Emitted light was collected by a monochromator and a CCD camera; the data presented are corrected for the spectral response of the measuring setup. The room temperature PL measurements are reported in figures 3.1 and 3.2 for the ion implanted and sputtered samples. The former was implanted with a dose of $1 \times 10^{17} \text{ cm}^{-2}$ and annealed at $1050 \text{ }^\circ\text{C}$ for 2 h, and the latter one was sputtered with 70 Watt and annealed at $1100 \text{ }^\circ\text{C}$ for 3 h.

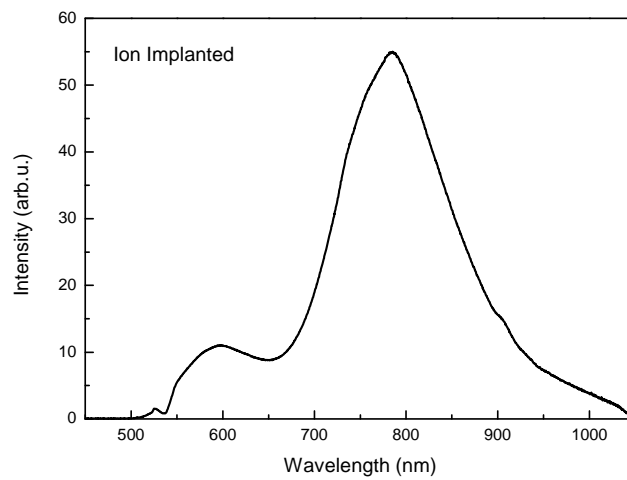


Figure 3.1. Photoluminescence spectra of ion implanted sample with a dose of $1 \times 10^{17} \text{ cm}^{-2}$.

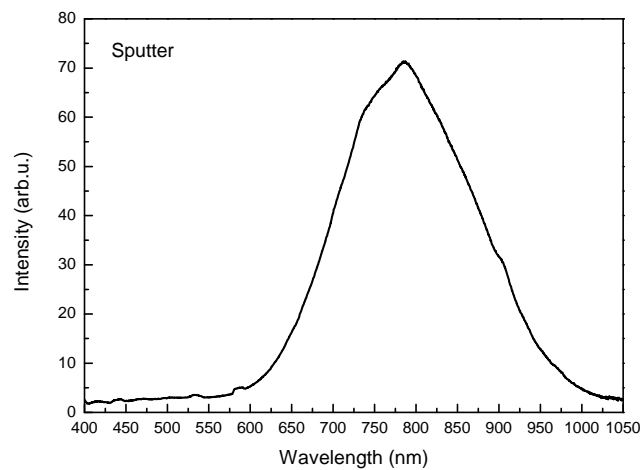


Figure 3.2. Photoluminescence spectra of magnetron sputtered sample.

PL spectra of free standing Si nanocrystals are shown in figure 3.3 for both as prepared and oxidized powders at 300 K. One can see the dramatic blue shift after chemical oxidation processes. This is evidence of smaller Si nanocrystalline structure in the oxidized sample.

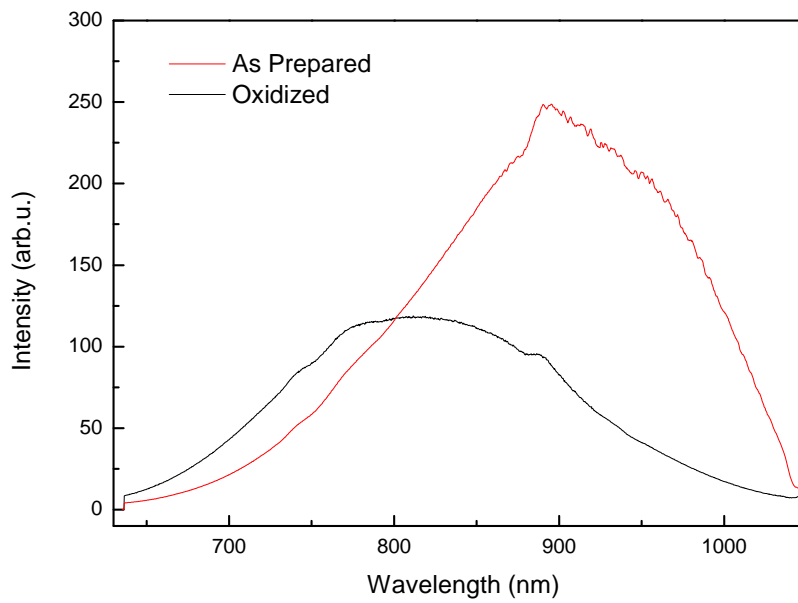


Figure 3.3. Photoluminescence spectra of as prepared and oxidized powder at 300 K.

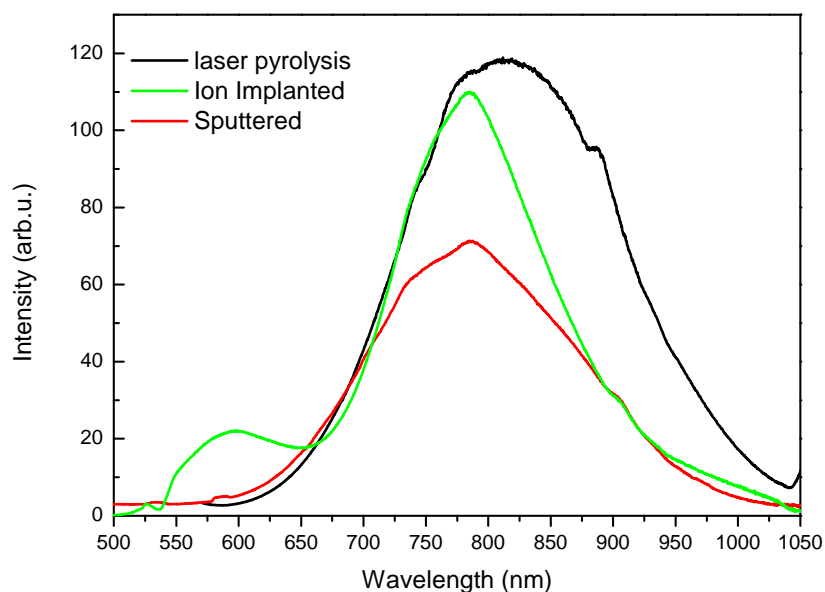


Figure 3.4 Luminescence spectra of samples produced by three different methods.

The PL spectra for various production techniques are shown in figure 3.4 for comparison. All peaks are broad in the range from 650 to 950 nm. It can be noted that photoluminescence emission is practically unchanged between implanted and sputtered samples. Although they have different shapes and characteristics the energy of the PL from different samples are practically similar. As shown in figure 3.4, even if the PL emission intensity from sputtered samples is seen relatively weak compared to other production techniques, it is not true to say something about PL intensity. Since the large variation in silicon nanocrystal size, the luminescence emission exhibits broad characteristics for Si nanocrystals produced by laser pyrolysis techniques, which also generated the maximum PL emission. PL peak position is located at higher wavelengths for laser pyrolysed sample indicating the presence of bigger mean size Si-nc.

3.3 Effects of annealing temperature on PL from Si nanocrystals

Amorphous SiO₂ with excess Si were produced by ion implantation of Si in thermal SiO₂. The annealing process was performed at different temperatures in N₂ atmosphere. This process was performed in order to study the influence of annealing temperature and time on the optical properties of Si nanocrystals. The detailed sample characteristics are reported in table 3.1.

Table 3.1: Details of the implantation process. Samples were implanted with $1 \times 10^{17} \text{ cm}^{-2}$ Si doses and annealed at 800, 900, 1050 °C.

Sample	Implantation dose (cm^{-2})	Annealing Temperature (°C)
U1	1.5×10^{17}	800, 2 h
U2	1.5×10^{17}	900, 2 h
U3	1.5×10^{17}	1050, 2 h
U4	1.5×10^{17}	1050, 5 h

PL spectra for samples U1, U2, U3 and U4 are displayed in figure 3.5. This graph also published in references [66]. The role of the heavily damaged dielectric matrix, typically induced by high dose implantation processes, is clearly evidenced in this figure. In fact, it can be observed a marked difference in emitted intensity between samples annealed for 5h and sample annealed for 2h at 1050 °C. It is clear that with the increase of the annealing time a better passivation of nanocrystals surface is reached [67] with the consequent reduction of non-radiative decay channels.

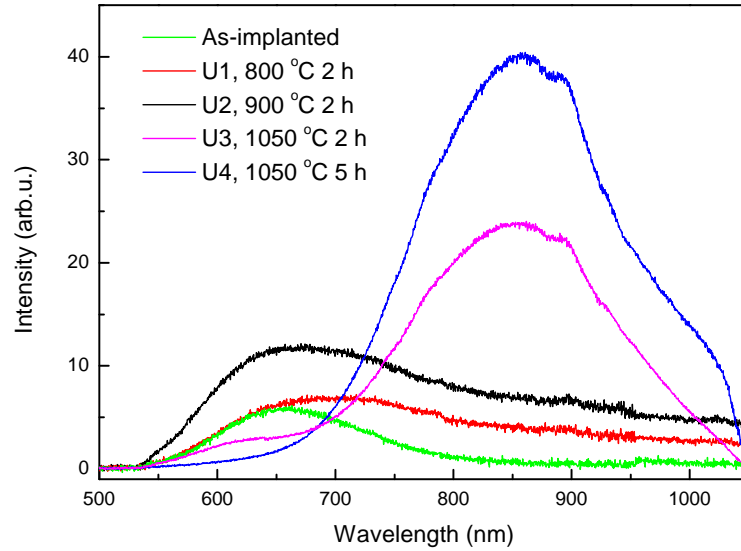


Figure 3.5 PL spectra of a sample which is implanted with Si with a dose of $1.5 \times 10^{17} \text{ cm}^{-2}$ and annealed at various annealing temperatures for 2 h under N_2 atmosphere.

In the spectra shown in figure 3.5, we see a shoulder peaked at about 500 nm and 700 nm. It could be attributed to the recombination of carriers trapped on the pair of oxygen interstitial vacancy or to the electron–hole recombination on a Si cluster of 5 atoms acting as nanocrystals precursors. These kinds of defects are easily produced during the Si implantation process.

3.4 Effect of dose on PL from Si nanocrystals

Si nanocrystals were synthesized by ion implantation at energy of 100 keV with the range of fluencies: 1×10^{16} , 2×10^{16} , 5×10^{16} , 1×10^{17} , and $2 \times 10^{17} \text{ cm}^{-2}$ at room temperature. The as-implanted samples were annealed at 1050 °C in high purity N_2 for 2 h.

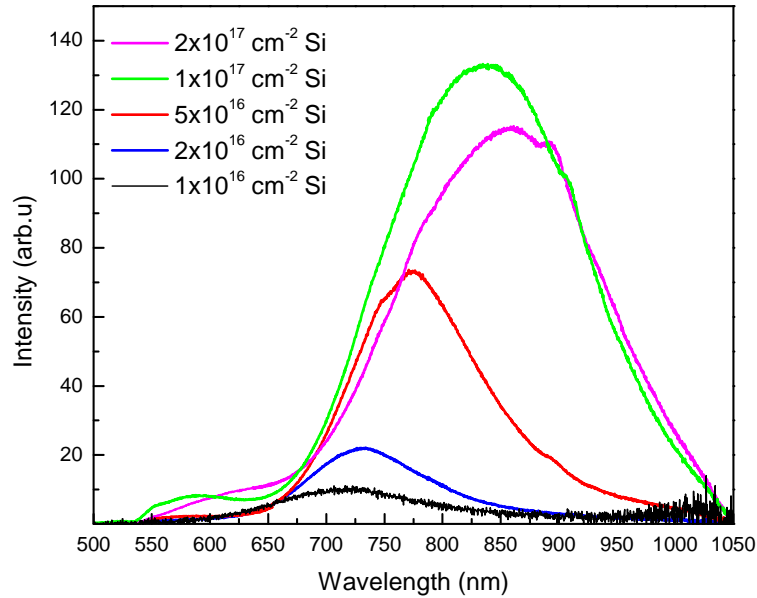


Figure 3.6. PL spectra of SiO₂ film implanted different doses as indicated in the figure.

Figure 3.6 shows the PL spectra after annealing of samples. The PL intensity is the highest for the dose of $1 \times 10^{17} \text{ cm}^{-2}$. The PL intensity decreases for higher fluences. This is because at higher fluence the nanocrystals density and size increase. Therefore interparticle spaces decreases giving rise to exciton migration between nanocrystals. Also, the probability of larger nanocrystals containing defects increases while oscillator strength decreases for larger Si nanocrystals. All of these effects are detrimental to radiative recombination. The first listed effect is important because the probability for energy transfer between nanocrystals becomes more probable.

Figure 3.7 shows the peak intensity position of Si nanocrystals as a function of fluence. Since the emission wavelength corresponds to size of nanocrystals, the red shift corresponds to an increase in the mean size optically active Si nanocrystals. It is clear that larger nanocrystals have a large surface area and thus more likely to contain defects.

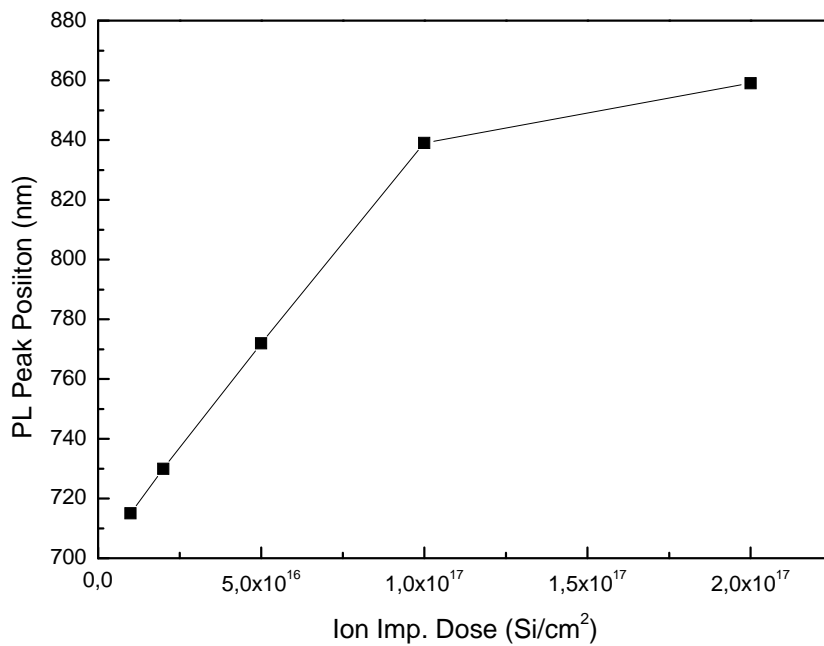


Figure 3.7. The peak intensity position as a function of fluence.

3.5 The effect of H₂ passivation on PL from Si nanocrystals

Si nanocrystals were synthesized by ion implantation at energy of 100 keV with the dose of $1 \times 10^{17} \text{ cm}^{-2}$ at room temperature. The as-implanted samples, placed in a quartz boat, were annealed at 1100 °C in high purity N₂ for 2 h in a conventional quartz-tube furnace. H₂ passivation was performed in high purity H₂ forming gas (%5 H₂ in N₂) at various temperatures for 1 h.

Photoluminescence and Time-resolved PL measurements were performed using frequency-doubled YAG laser (532 nm). The repetition rate was 50 Hz. The emitted PL was dispersed by HR460 Jobin Yvon monochromator and detected by a cooled InGaAs photomultiplier tube. PL transients were stored and averaged by SR400 photon counter and a SR430 Multichannel Scaler- Stanford Research Systems.

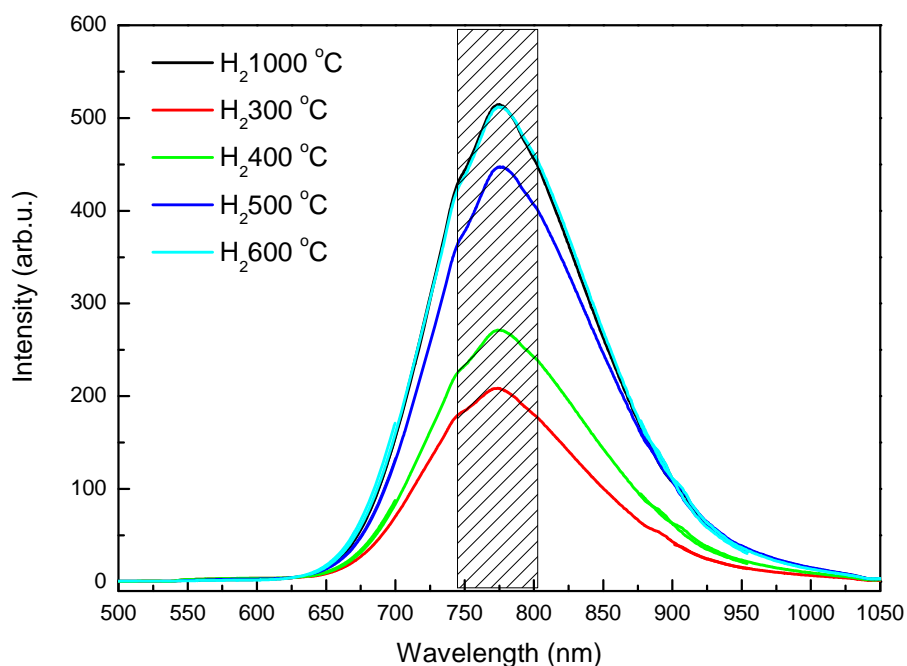


Figure 3.8. The effect of H₂ passivation on the photoluminescence of the Si nanocrystals.

Figure 3.8 shows the effect of H₂ passivation on the photoluminescence of the Si nanocrystals. Samples were produced by ion implantation and annealed at 1100 °C for 2 h with N₂ and post annealed under H₂ for 1 h, respectively. The increase in the PL intensity is due to the passivation of non-radiative defects at the nanocrystals/oxide interface. The shaded region represents the approximate detection window used time-resolved photoluminescence experiments. The choice of this window is arbitrary, as the trend of increasing intensity with improved passivation was found to be comparable across the whole PL spectrum.

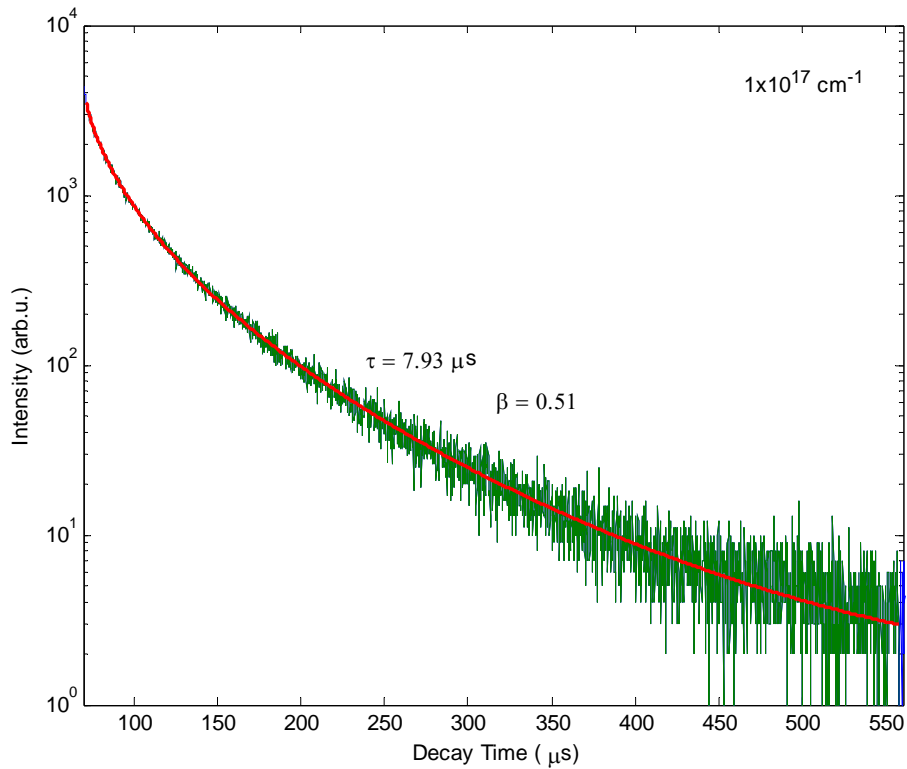


Figure 3.9 Typical normalized decay time measurements of the PL signal around 775 nm for the sample implanted with $1 \times 10^{17} \text{ cm}^{-1}$ and subsequent and post annealing with H_2 for 1 h was performed. The red solid lines are the stretched exponential fit. Data was taken at room temperature.

Figure 3.9 shows the plot of time-resolved PL experiments at 775 nm for the sample post annealed with H_2 for 1 h. The curve is clearly not well fitted by simple exponential. As expected it is well characterized by stretched exponential function.

The complete model of this process is unclear as the source of the PL mechanisms from Si nanocrystals is still under debate. The results of TRPL experiments of Si nanocrystals are extensively discussed in chapter 5.

3.6. Conclusion

In summary, the data reported in this chapter provides an overview of the differences that can be observed in the optical properties of Si-nc fabricated with different techniques and processed in different ways. Ion implantation and sputtering are two well known techniques used in electronic and optoelectronic devices. They are shown to be a suitable process for the fabrication of silicon nanocrystals in oxide matrices. The laser pyrolysis technique is a new approach for the fabrication of free standing nanocrystals. A comparison of these three techniques has revealed that characteristic emission band of Si nanocrystals can be obtained by different approaches. However, some features of the emission spectra are different for different preparation techniques. We show also in this chapter that peak position of the PL band can be tuned by changing the amount of deposited Si into the SiO₂ matrix. This is a direct demonstration of quantum size effect. The effect of annealing temperature and the passivation are also studied and the results are discussed in terms of possible light emission center in Si nanocrystals.

CHAPTER 4

TEMPERATURE DEPENDENT PHOTOLUMINESCENCE OF Si NANOCRYSTALS

4.1. Introduction

The temperature dependence of PL has been studied for porous Si [58, 69] and Si [57, 70-74] nanoparticles in order to understand the basic physical mechanisms generating light emission from these systems. However, the interpretation of the results is usually not straightforward. An adequate explanation for these observations, various models has been suggested. Kanemitsu *et al.* [57] proposed a three-region model and Brongersma *et al.* [74] applied a model premised on the energy splitting of singlet and triplet excitonic states by exchange interaction. The splitting model of luminescent states was first proposed by Calcott *et al.* [69] for porous Si, which give us a useful expression for the temperature dependent radiative decay rates. According to this model, the luminescent excitonic states are split to a singlet state and a triplet state with a splitting energy ΔE due to the exchange interaction. At very low temperatures, almost all of the excitons are trapped in the lower triplet state (resulting in a smaller triplet decay rate, longer lifetime). With temperature some of them are excited to the upper singlet state which is dominant at high temperature (resulting in a larger singlet decay rate, shorter lifetime). Recently, M. Righini *et al.* [75] have demonstrated that the different thermal activation energy behavior between crystal and amorphous nano-silicon is based on their different nano-structure and recombination mechanisms.

Author suggested that the amorphous nano-silicon shows similar PL behavior with those obtained in crystal nano-silicon attributed to quantum confinement effect that the nano-structure size decreases, the band gap increases, photoluminescence shows blue-shift and PL intensity increases as temperature increases. For amorphous silicon nano-structure, other mechanisms should be considered, particularly, regarding band tails of defect and disorder arisen from localized states extending into band gap. The exchange splitting arisen from QC can be disregard for the amorphous silicon nano-structure. Because of the radiative recombination occurs by tunneling between deepest energy states in conduction band and valence band states without a Stokes shift in amorphous nano-silicon, the photo-generated carriers can move to a large volume of amorphous silicon. Therefore, the thermal activating energy is nothing than the potential barrier. The photo-excited carriers tunnel to the lowest tail state. M. Righini et al. suggested that Franck–Condon shift of deep tail state is responsible of this potential barrier. Since the Franck–Condon shift only depends on the local atomic relaxation, it is not affected by the quantum [75].

In this chapter, two kinds of PL experiments have been performed. In continuous wave (cw) PL experiments the system approaches a steady state where all relaxation and transient phenomena have already disappeared and a steady state PL spectrum is measured as a function of temperature. Time-resolved PL experiments have been studied dynamical aspects of the nanocrystals. The investigated dynamics depends on the temperature. Samples are prepared by ion implantation in a SiO₂ layer followed by thermal annealing with H₂ passivation treatment. The results of both experiments have been discussed by considering two-level splitting model proposed by Calcott et al. [69]. However, we observed that at high temperatures two level model do not work properly. Clearly this phenomenon needs a new contribution to explain the PL from Si nanocrystals. Instead two-level model, our data well fitted with three level model proposed by M. Dovrat [76] et al. will be discussed in detail at chapter 5.

Briefly, photoluminescence intensity shows a temperature dependence which has been observed in all samples: the PL intensity rises with increasing temperature

up to ~ 120 K, and then weakly reduces up to room temperature. This characteristic behavior which has been reported by many research laboratories indicates that the population of radiative states is built up by thermally activated process. As described above, this increase in the population of radiative states is related to either splitting of energy states in the nanocrystals or diffusion of charge carriers to the sites where radiative states are available.

4.2. Experiment

4.2.1. Preparation of Silicon (Si) Nanocrystals in SiO₂

Thermally grown 250 nm thick SiO₂ films on (100) Si wafers were implanted with ²⁸Si ions at an energy of 100 keV with the dose of 2×10^{16} , 5×10^{16} , 1×10^{17} and 1.5×10^{17} ions/cm². Samples implanted with Si were annealed at 1100 °C for 2h and 1000 °C for 1h under N₂ and H₂ atmosphere, respectively. Samples were mounted in a closed-cycle helium cryostat to perform measurements in the temperature range of 10-300 K. The structural analysis of these samples has been performed by TEM and Raman analysis with which the presence of Si nanocrystals has been identified.

4.2.2 Photoluminescence and Time Resolved Measurements

PL spectroscopy was used to characterize the samples optically. The luminescence spectra were measured using a monochromator and a 256x1024 charge-coupled device (CCD) detector. Samples were mounted in air and or placed in a closed-cycle cryostat for temperature control between 10 K and 300 K. Samples were excited at an angle of $\sim 45^\circ$ from the normal, using the 532 nm Nd-YAG lasers at power $\sim 10\%$ out of 3 Watt. A 532 nm band-pass filter in front of the monochromator entrance slit was used to cut off diffracted laser illumination. The spectra of reference sample were taken under the same excitation power and used for an identical alignment. All spectra were corrected for the efficiency of the CCD and grating.

TRPL was used to extract PL decay lifetimes. TRPL measurements were performed using YAG laser (532 nm with a repetition rate of 50 Hz at optical

laboratory of The Department of Physics, Chemistry and Biology (IFM) Linköping University, Sweden. The emitted PL was dispersed by HR460 Jobin Yvon monochromator and detected by a cooled InGaAs photomultiplier tube. PL transients were stored and averaged by SR400 photon counter and a SR430 Multichannel Scaler- Stanford Research Systems.

4.3. Results and Discussions

Figure 4.1 shows the PL spectra of the Si nanocrystals measured in the temperature range of 30- 300 K. A broad PL spectrum was observed in the near-infrared region. With decreasing the temperature from 300 to 30 K, the intensity of the PL spectra increased slightly, peaked at about ~120 K and then decreased rapidly. At low temperatures, carriers photoexcited inside the nanocrystal populate radiative recombination centers through thermally activated processes. As a result the PL intensity increases with temperature until the population of radiative centers reaches saturation, this behavior is shown in Fig 4.1.

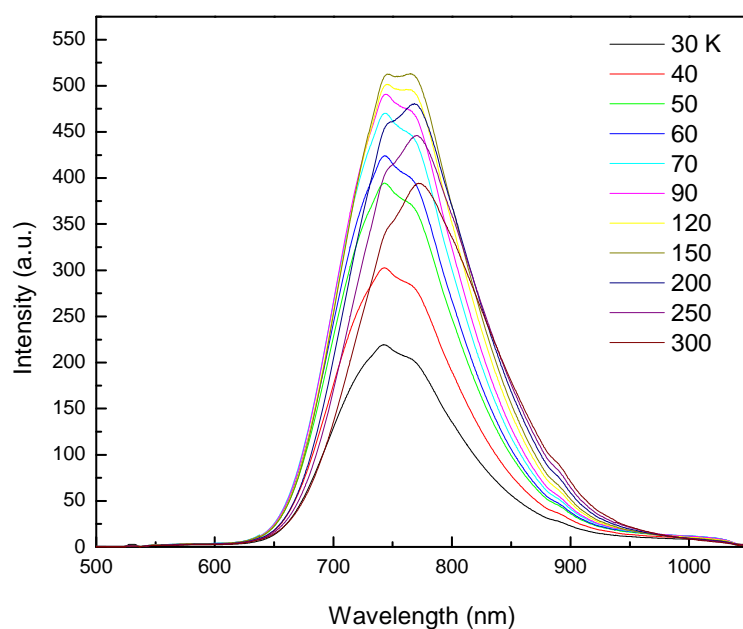


Figure 4.1. PL spectra taken from 30 to 300 K of ion beam synthesized Si nanocrystals with a broad size distribution. Samples annealed at 1100 °C with nitrogen atmosphere and subsequent annealing performed at 1000 °C with H₂.

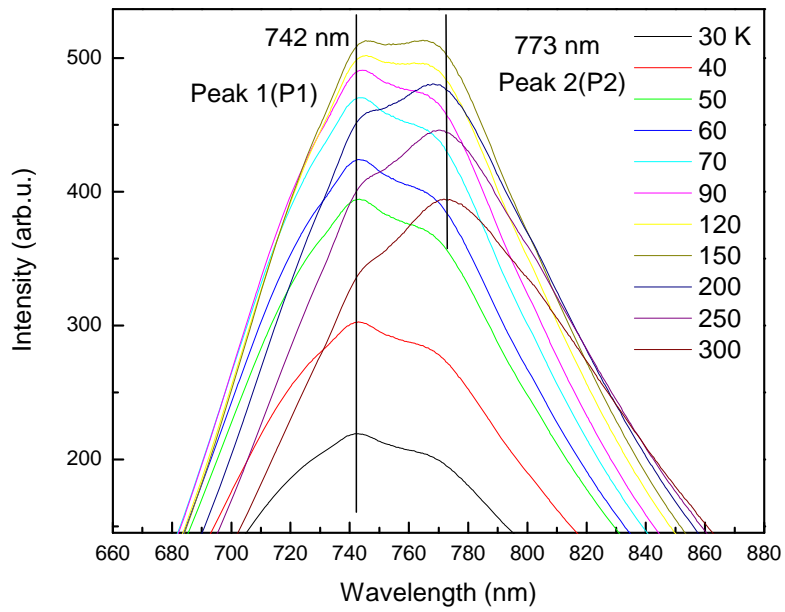


Figure 4.2. Peaks P1 and P2 depicted by focusing view of photoluminescence spectra.

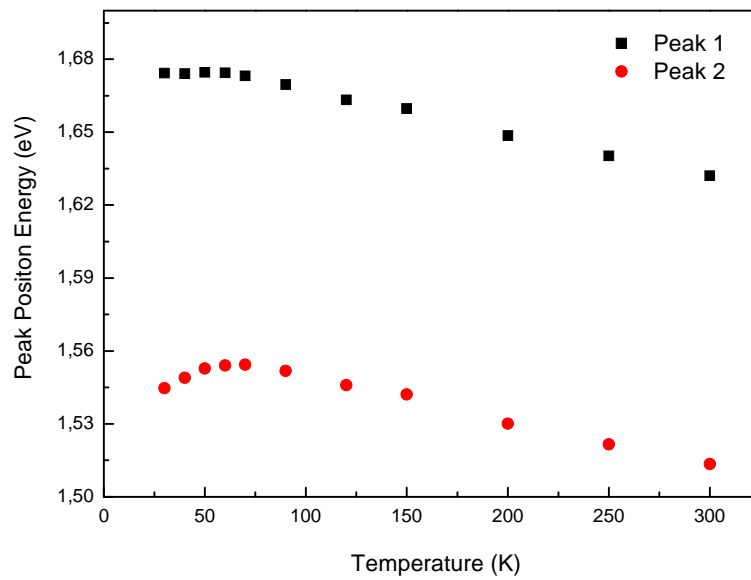


Figure 4.3. Temperature dependence of the deconvoluted PL peaks position for samples with the doses of $1 \times 10^7 \text{ cm}^{-2}$.

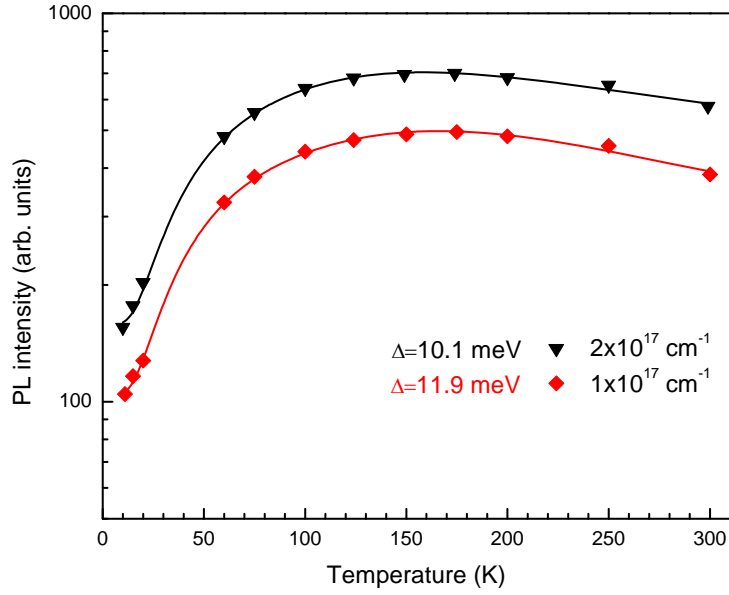


Figure 4.4. Temperature dependence of the PL intensity for samples with Si implantation doses of $1 \times 10^{17} \text{ cm}^{-2}$ (diamond), and $2 \times 10^{17} \text{ cm}^{-2}$, (triangles) respectively. Solid lines are the best fits of data using Eq. 1. In the inset the activation energies obtained from the fitting procedure are shown.

As shown in figure 4.3, all of these findings are consistent with previous experiments in which Brongersma et al. [74]. The authors attribute the temperature dependence of PL to a model in which the excitonic state is split into a lower-energy triplet state and an upper singlet state, where radiation from the triplet state is forbidden by parity, though this rule is relaxed by spin-orbit coupling. The temperature dependence of photoluminescence intensity is given by:

$$I_{PL} = \frac{I_0}{1 + A \exp(-\Delta/kT) + 1 + B \exp(-\Delta_{NR}/kT)}, \text{ Eq (1)}$$

where Δ is the activation energy implied into radiative process and Δ_{NR} that for non-radiative recombination. We obtain the activation energies Δ for each sample.

Δ decreases for samples with Nc of larger sizes. In the Calcott model, by decreasing the Nc size the quantum confinement increases and, so does the energy splitting. The trend of Δ , seen in figure 4.4, is a strong indication for PL more likely originates from QC rather than from the defects located at Si/SiO₂ interface. Similar results were found for various implantation doses by M.Righini et al. [75]. In order to confirm this observation, we have studied the recombination dynamics within the QC model. Following the model developed by Calcott [2], the radiative decay time τ is determined by the thermal equilibrium between radiative lifetimes of triplet (τ_L), singlet (τ_U) states and energy separation (Δ) as described by the equation:

$$\frac{1}{\tau} = \frac{\frac{g}{\tau_L} + \frac{e^{-\frac{\Delta}{kT}}}{\tau_U}}{g + e^{-\frac{\Delta}{kT}}}$$

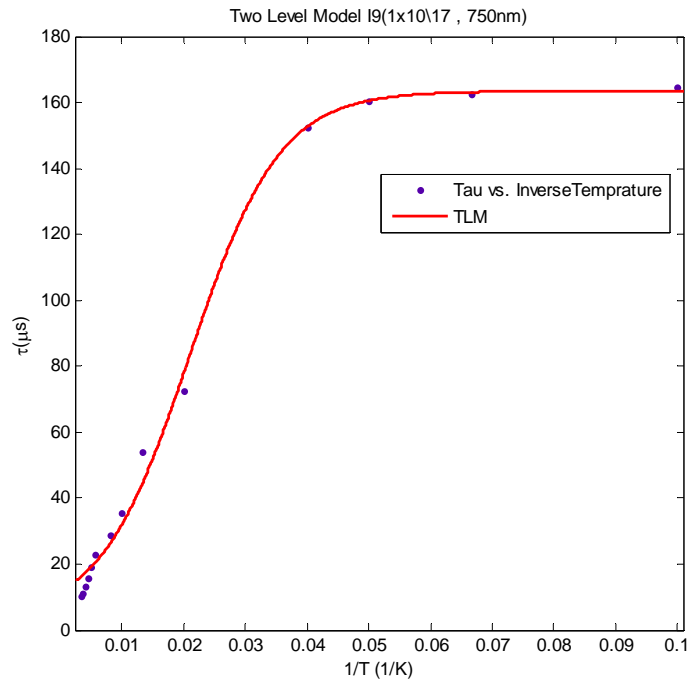


Figure 4.5. PL lifetime versus inverse temperature of Si nanocrystals and fitting curve with respect to two levels model for sample implanted with a dose of $1 \times 10^{17} \text{ cm}^{-2}$. Data was taken at 750 nm.

At low temperatures, only the lower triplet state of the exciton is populated and PL decay is dominated by the long lifetime which was determined to be $\tau_L = 490.3 \mu\text{s}$ for the sample implanted with the dose of $1 \times 10^{17} \text{ cm}^{-2}$ shown in figure 4.5. At high temperatures the upper singlet state becomes populated and PL decay has a short lifetime, $\tau_U = 9.299 \mu\text{s}$. We also determine the splitting energy between these levels as $\Delta = 11.9 \text{ meV}$. At low temperatures, only the triplet state is populated and radiative decay rate is small. At intermediate temperatures, there is enough thermal energy to surmount the splitting energy, $\Delta \sim 12 \text{ meV}$, and the radiative decay from the excited singlet state is high. At high temperatures, the lifetime decreases and therefore so does the quantum yields.

4.4. Conclusion

In conclusion, the temperature dependence of photoluminescence intensity was studied. The analysis of temperature dependence of both PL intensity and lifetime provides evidences for the presence of activation energy in the emission process. This energy decreases by increasing Nc size, in accordance with prediction of quantum confinement models. In conclusion, our experimental results point out that in the range of Nc dimension studied, the radiative recombination seems to rise from excitons confined inside Nc rather than from states at the Nc surface. Moreover, the detail studies on decay dynamics of Si nanocrystals will be discussed in Chapter 5.

CHAPTER 5

TIME-RESOLVED PHOTOLUMINESCENCE of Si NANOCRYSTALS

5.1. Introduction

The PL decay process from Si nanostructures has been intensively investigated over the recent years, both from porous silicon [14] and from Si nc's embedded in SiO₂ [5, 15, 19, 77] matrices. Extensive investigations have been carried out in order to understand the origin of luminescence from Si with a dimension of a few nanometers. The PL properties of emission bands are commonly explained by the widening of the energy gap due to quantum confinement in Si. Since the size of Si decreases beyond the free-exciton Bohr radius the quantum confinement effect would significantly change the optical behavior of the system, causing the excitations in the visible range [78]. As an important prior condition for optoelectronic application of Si nanocrystals, one needs to understand the recombination mechanisms. However, the complicated nature of SiO₂/Si structure does not allow us to identify the basic transition mechanisms generating the light emission from them [23]. The recombination dynamics in Si nanocrystals can be explained by using the excitonic fine structure which is the subjects of intense research activities aiming to understand how they influence the photoluminescence properties of Si nanocrystals. Ignoring the symmetry of excitons, most of the experiments reported so far [74, 79] have tried to understand the origin of photoluminescence of Si Nc's by using the exchange splitting model known as Two Level Model proposed by Calcott et al. [69].

According to this model, the lower level corresponds to a triplet state ($S=1$) and the upper one is a singlet state ($S=0$). Due to the exchange interaction, the degeneracy between these states is lifted locating triplet state at a lower position with respect to the singlet state by a splitting energy Δ . However, some recent studies have suggested that involvement of another exciton level should be taken into the account for a complete description of the system. The fine structure of excitons and its role in optical transitions is needs to be studied to gain a deeper understanding of the light emitting mechanism in Si nanocrystals.

In this chapter, we report the temperature dependent TRPL and PL spectroscopy of Si nc and discuss the role of the confined excitonic states in Si nc referring to the three level model recently proposed by M.Dovrat et al. [76]. We show that three excitonic levels participate in light generation process in Si nanocrystals embedded in SiO_2 matrix.

5.2. Experiment

100 keV ^{28}Si ion were implanted into thermally grown 100 nm thick SiO_2 on an n-type Si substrate with a dose of $1 \times 10^{17} \text{ cm}^{-2}$. Samples were annealed under nitrogen (N_2) atmosphere at 1050 °C for 2 h to induce nanocrystals formation and named as I9. TRPL was used to extract PL decay lifetimes. TRPL measurements were performed using YAG laser (532 nm). The repetition rate was 50 Hz. The emitted PL was dispersed by HR460 Jobin Yvon monochromator and detected by a cooled InGaAs photomultiplier tube. PL transients were stored and averaged by SR400 photon counter and a SR430 Multichannel Scaler- Stanford Research Systems.

5.3. Excitonic Model for Si Nanocrystals

Figure 5.1 show typical PL spectra obtained from Si nanocrystals with a mean diameter of $d \approx 3\text{-}5\text{nm}$ with a deviation of 1.1 nm which were observed with the transmission electron microscope in ref [80]. PL peaks have generally a Gaussian

shape centered at 775 nm at 300 K and shifts to lower wavelengths with decreasing temperature.

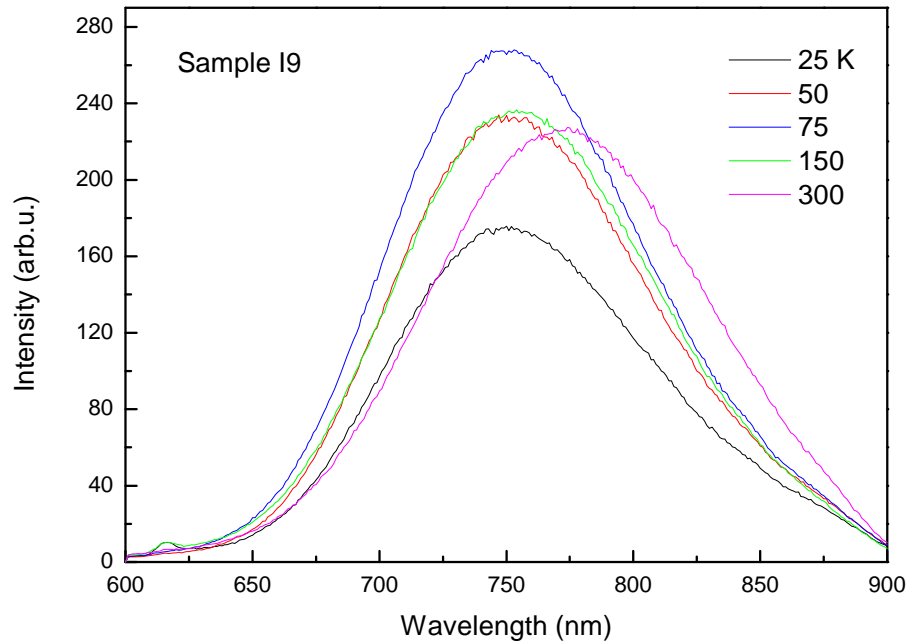


Figure 5.1. PL spectra of Si nanocrystals obtained from sample I9 at different temperatures but only a few represented in the figure.

The time decay of the PL signal at 750 nm for the sample I9 is shown in figure 5.2. The PL decay curve is commonly fitted to the stretched exponential function $I(t) = I_0 \exp(-(t/\tau)^\beta)$ where τ is the PL lifetime and β ($0 \leq \beta \leq 1$) is the dispersion exponent. The origin of the stretched exponential decay for the luminescent emission of Si-nc is really controversial. It is an empirical equation suited for the fitting of experimental data ranging from the dielectric relaxation of glasses and polymeric materials [81] to the structural relaxation of disordered systems like glasses or amorphous materials at a fixed temperature [82].

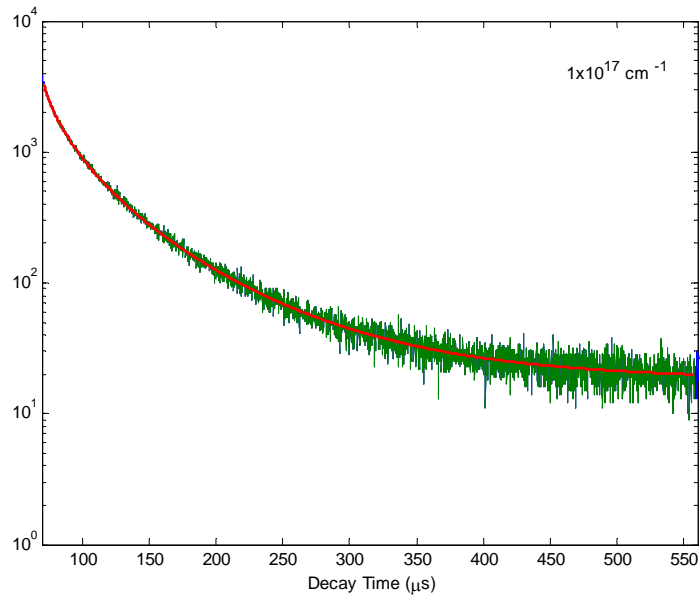


Figure 5. 2. TRPL decays (not normalized to the initial PL intensity) at 300 K for sample I9. The solid line represents the fit of the experimental data to the equation of from, $I(t) = I_0 \exp(-(t/\tau)^\beta)$ where τ is the PL lifetime and β ($0 \leq \beta \leq 1$) is the dispersion exponent.

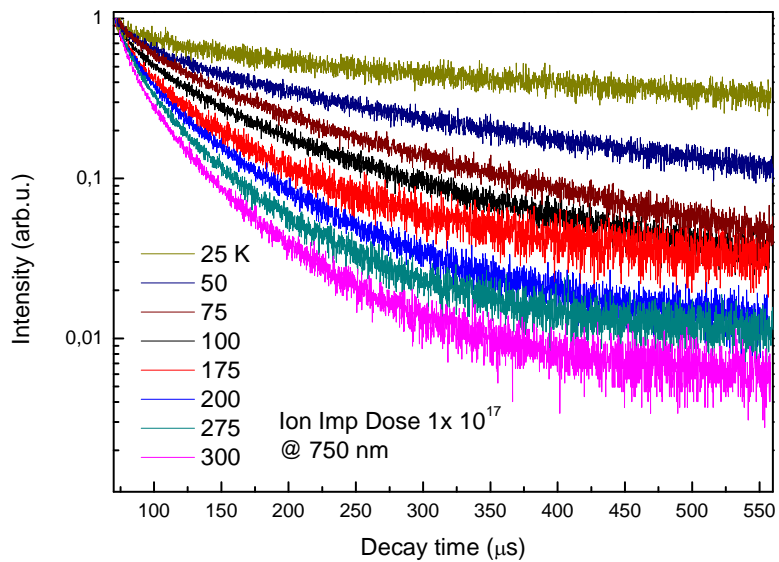


Figure 5.3. PL decay curves at various low temperatures.

The dependence of the PL decay time on temperature is shown in figure 5.3. The temperature decreases while the PL decay time increases and approaching fairly slow PL lifetimes of about a few hundred microseconds at low temperatures. Figure 5.4 shows the temperature dependence of the PL lifetime extracted from the time decay of the PL spectra for various wavelengths. It is seen that the lifetime values increases from $\sim 10\text{-}40\ \mu\text{s}$ at room temperature to $\sim 300\ \mu\text{s}$ at 25 K for this sample. Furthermore, the variation rate in the life time is high at high temperature and gradually decreases with decreasing temperature. Similar lifetime behaviors were recorded for other samples as well.

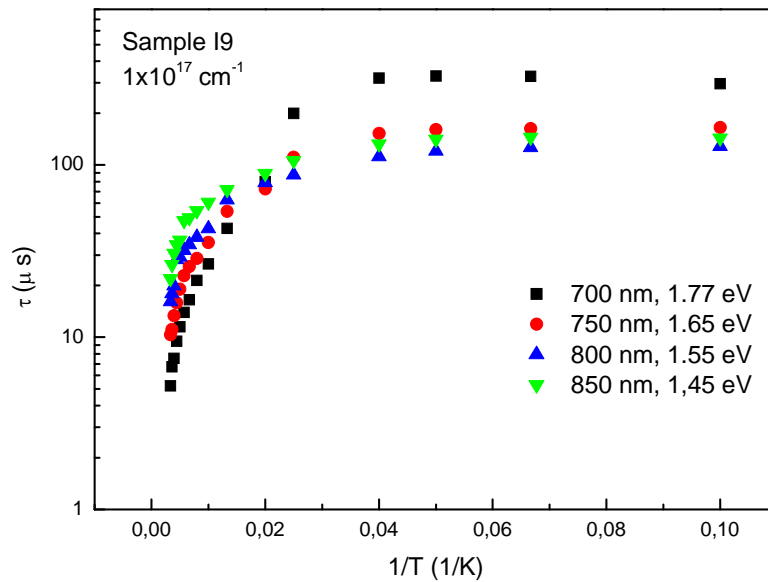


Figure 5.4. Arrhenius plot of the PL lifetime obtained from sample I9 for different wavelengths.

To analyze the temperature dependence of PL decay curve shown in figure 5.4, we can identify two temperature regimes. In the low temperature regime, the PL lifetime is essentially independent of the temperature, while at high temperature region, the PL lifetime becomes shorter with the increasing temperature. This characteristic can be described by the exchange splitting model proposed by Calcott

et al. [69] for porous Si. In typical semiconductors the lowest excitonic state is composed of conduction electrons having a total angular momentum of $J=1/2$ (the sum of orbital angular momentum ($L=0$) of the conduction band and spin of the electrons ($1/2$)) and heavy-holes states having $J=3/2$ ($L=1$ of the valence band and spin $1/2$). Hence, the total angular momentum of the exciton can be either 1 or 2. Of course, quantum confinement makes this picture much more complicated as different bands can be mixed and the spherical symmetry of the ideal dot can be distorted (in fact, the spherical symmetry of the dot is always slightly distorted when constructed from a cubic crystal). Calcott et al. assumed that only the spin components of the total angular momentum are conserved which the exciton consist of two spin $1/2$ particles. According to this case, the total spin of the exciton can be either $S = 1$ (triplet) or $S = 0$ (singlet). The singlet-triplet degeneracy is lifted by the Coulomb exchange interaction between electrons and holes. Following the exchange interaction rule by considering the Pauli principle, a singlet state (which is anti-symmetric with respect to exchange of the electron/hole spins) has to be symmetric with respect to the exchange of the electron/hole orbital states, while the spin-triplet state has to be orbitally anti-symmetric with respect to this exchange. Therefore, the Coulomb energy relevant to the exchange interaction is always larger for the spin-singlet state relative to the spin-triplet state. The case is schematically illustrated in figure 5.5, where Δ is the singlet-triplet exchange splitting energy.

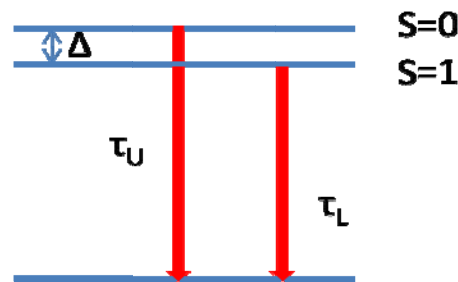


Figure 5.5. Schematically illustration of two levels with τ_L , τ_U and Δ being the lower state (triplet), the upper state (singlet) lifetime and the splitting energy, respectively.

For silicon nc's the splitting energy is fairly small, of the order of \sim a few hundred μeV (e.g. 150 μeV), however, since the exchange interaction is proportional to the overlap between the electron and the hole states, it can significantly be enhanced by confining the exciton into small nanostructures. This situation explains very well the behavior of the PL lifetime. According to this model, the exciton level splits into two levels with a singlet state at the upper and triplet one at lower position. One can extract the lifetimes associated with these states by fitting the following expression to the experimental data:

$$\frac{1}{\tau} = \frac{\frac{g}{\tau_L} + \frac{e^{-\frac{\Delta}{kT}}}{\tau_U}}{g + e^{-\frac{\Delta}{kT}}}$$

where $1/\tau_L$ is the rate of radiative transition from the lower triplet state, $1/\tau_U$ is the rate of radiative transition from the upper singlet state, $g=g_L/g_U=3$ is the level's degeneracy ratio. At low temperatures, only the lower triplet state of the exciton is populated and PL decay is dominated by the long lifetime which was determined to be $\tau_L = 490.3 \mu\text{s}$ for the sample I9 shown in figure 5.4. At high temperatures the upper singlet state becomes populated and PL decay has a short lifetime, $\tau_U = 9.299 \mu\text{s}$. We also determine the splitting energy between these level as $\Delta = 11.9 \text{ meV}$.

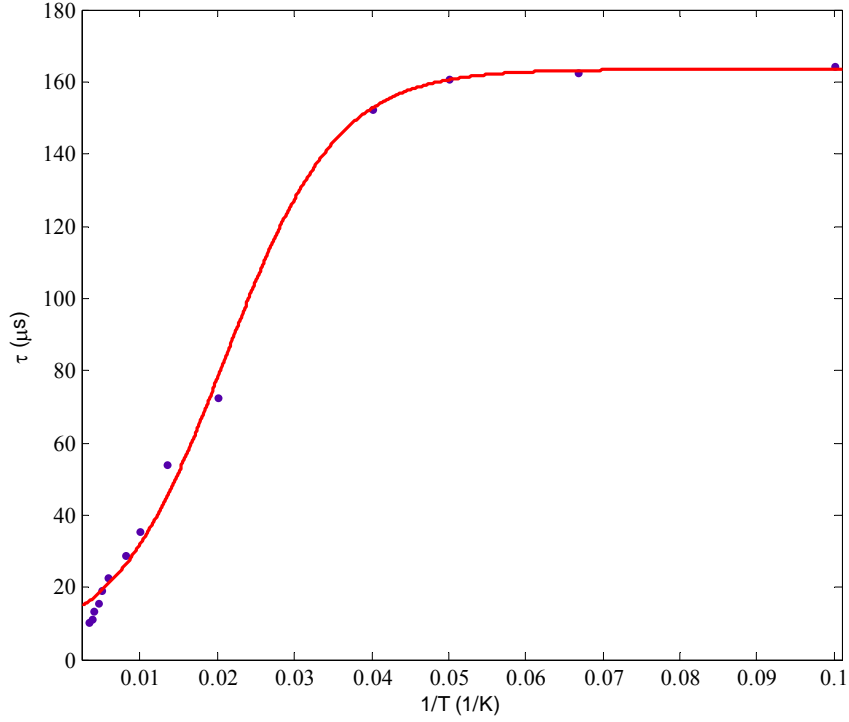


Figure 5.6. PL lifetime versus inverse temperature of Si nanocrystals and fitting curve with respect to two level model for sample I9 at 750 nm.

However, we see from figure 5.6 that the two-level model does not properly fit the experimental data, particularly at high temperatures. This discrepancy can be removed by using a model with three level involvements in the light emission process [76]. The PL decay times corresponding to three energy levels τ_1 , τ_2 , τ_3 , are then determined by using the following expression:

$$\frac{1}{\tau} = \frac{\frac{g_1}{\tau_1} + \frac{g_2}{\tau_2} e^{-\frac{\Delta_{21}}{kT}} + \frac{g_3}{\tau_3} e^{-\frac{\Delta_{31}}{kT}}}{g_1 + g_2 e^{-\frac{\Delta_{21}}{kT}} + g_3 e^{-\frac{\Delta_{31}}{kT}}}$$

where Δ_{ij} is the splitting energy between i^{th} and j^{th} levels, τ_j and g_j are the lifetime and corresponding degeneracy of the j^{th} level, and T is the temperature.

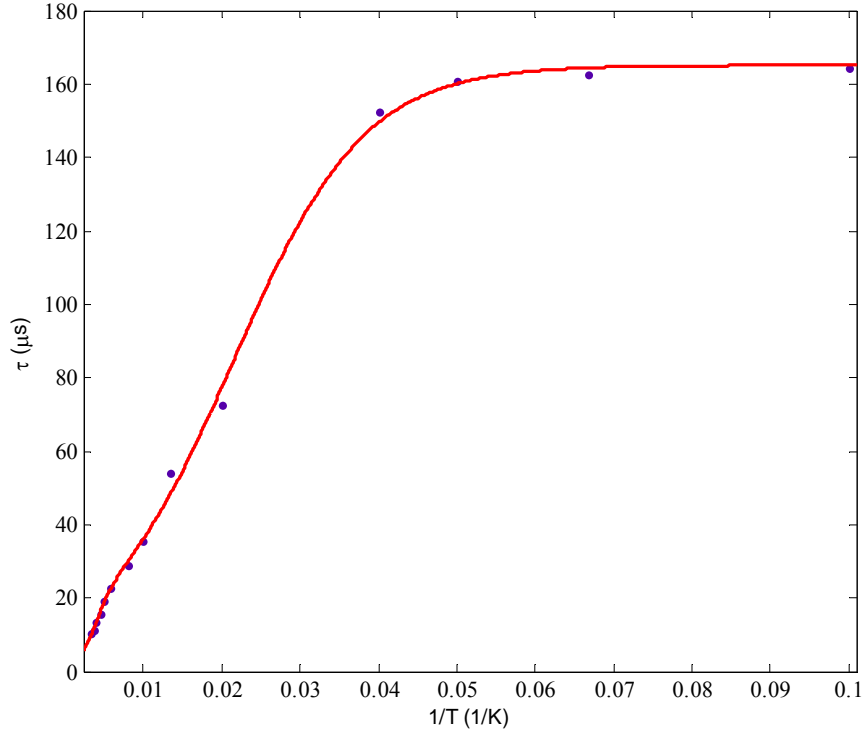


Figure 5.7. PL lifetime versus inverse temperature of Si nanocrystals and fitting curve with respect to three level model.

As shown in Figure 5.7, an excellent fit has been obtained by three level expressions. PL decay times and splitting energies obtained from this fit are: $\tau_1 = 165.1 \mu\text{s}$, $\tau_2 = 4.134 \mu\text{s}$, $\tau_3 = 0.202 \mu\text{s}$, $\Delta_{21} = 10.37 \text{ meV}$, $\Delta_{31} = 83.81 \text{ meV}$. Note that the degeneracy factors $(g_1: g_2: g_3) = (9:3:3)$ are used in this fitting procedure.

Excitonic transitions in Si nanocrystals have been studied by several research groups [83-85]. In these studies excitonic states are shown to possess the several symmetries derived from the symmetries of the bulk silicon carriers (eg. the conduction band electrons and valence band holes). These particles have t_2 symmetry of the bulk silicon T_d point group. Reboledo et al. [86] showed that the electron-hole Coulomb interactions are very important in determining the symmetry of excitons for silicon atom. There are some possible symmetry of the excitons as a

result of the symmetry of conduction band electrons and valance band holes. For instance, if both the valance band maximum and conduction band minimum have t_2 symmetry, one can get $t_2 \times t_2 = T_1 + T_2 + A_1 + E$ excitons. The coulomb interactions are able to shift and split the 36-fold degeneracy of the exciton energies into four degenerate levels denoted E, A_1 , T_1 , and T_2 with degeneracy 8, 4, 12, and 12, respectively. Following these considerations [86], M. Dovrat et al. [76] explained the hierarchy of the excitonic splitting and lifetimes. There are three lowest excited states, namely 3T_1 , 3A_1 , and 3E which are all spin triplet. Total degeneracy of the states is 18. Owing to the fact that there is no T_2 symmetry, any optical transition from these states is not only optically forbidden but also spin forbidden since they are all spin triplet. Such a state is the source of so-called dark excitation in the spectrum. There are semidark and semibright excitonic states which are optically allowed but spin forbidden (3T_2 with 9 times degenerate) or optically forbidden but spin allowed (1T_1 with 3 times degenerate), respectively. The remaining 3 times degenerate state (1T_2) is called bright since it's both optically and spin allowed. It's also noted that due to weaker spin-orbit interaction in silicon the spin selection rules is violated less than the orbital selection rules whose violation depends on structural imperfection such as surface and interface defects. Applying this model the following values were reported for the associated life times: $\tau_1 = 2 - 4$ ms, $\tau_2 = 40 - 60$ μ s, and $\tau_3 = 5 - 15$ μ s [11]. These values are well above our results, $\tau_1 = 165.1$ μ s, $\tau_2 = 4.134$ μ s, $\tau_3 = 0.202$ μ s. However, the characteristic of the decay time in both cases agrees with each other in a way that τ_1 is the slowest, τ_2 is midlevel, and τ_3 is the fastest lifetime. Therefore, we can conclude that the hierarchies of the exciton levels are the same in both measurements. With these results, the exciton splittings obtained from $t_2 \times t_2$ multiplets are schematically shown in figure 5.8.

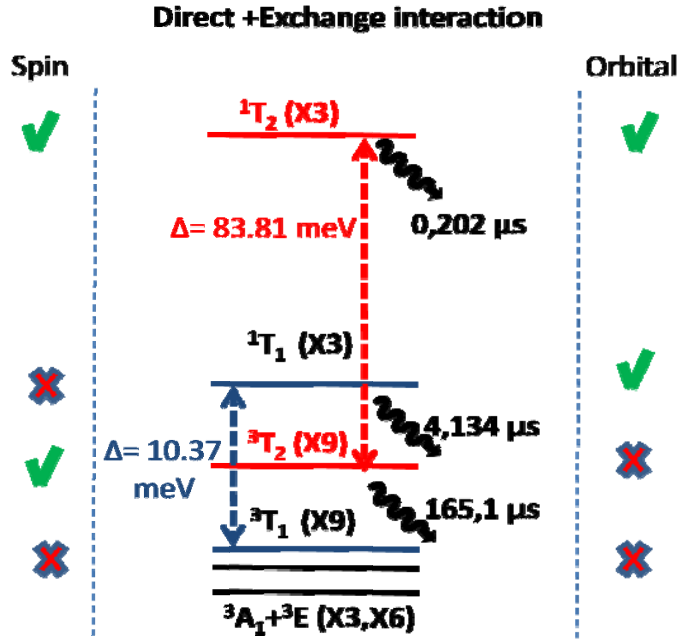


Figure 5.8. Schematic diagram of exciton splitting of Si nanocrystals. The measured energies and lifetimes of the excitonic states are presented. The degeneracy of each exciton is shown as X3 (level is 3 times degenerate), etc. An ✓ and an ✗ denote allowed and forbidden states, respectively.

Many experimental [69, 87-89] and theoretical [86, 91-96] studies carried out on the optical properties of silicon nc's have shown that the optical properties are significantly affected by the method of preparation of nanocrystals, inhomogeneous size distribution, environment and shape of nanocrystals. Particularly, the defect structure of the nanocrystals plays a detrimental role in the carrier life time. Hence, the difference between the measured life times and the previously reported values should be related to the structural and defect differences in nanocrystals.

5.4. Conclusion

In summary, we have investigated the effect of excitonic fine structure of silicon nanoparticles embedded in a silicon oxide matrix on light emission from them by using temperature dependent TRPL and PL spectroscopy. Due to QC effects, the

optical gap shifts to the higher energies as the nanocrystal size decreases as expected from quantum size effect. From the behavior of PL decay time as a function of temperature and wavelength, we have concluded that the light generation in nanocrystals occurs via involvement of three excitonic levels as suggested by a recently proposed model. The life times of the carriers residing in these levels have been determined by a curve fitting procedure, and found to be shorter than the previously reported values. The difference in the life time values can be attributed to the structural differences.

CHAPTER 6

LIGHT EMISSION FROM FREE-STANDING Si NANOCRYSTALS

6.1. Historical Perspective

Silicon nanostructures in the forms of porous silicon [1], silicon nc in the oxides matrix [97], and freestanding crystalline Si nanoparticles [45] have been investigated intensively because of their unique electrical, optical and chemical characteristics. In addition their potential as light sources [98, 99], Si nanocrystals are strong candidates for a new generation of flash memory, solar cell application and other optoelectronic technology.

The most challenging task is the understanding of light emitting mechanisms from Si nanocrystals. Because of radiative and nonradiative recombination processes that may occur at interface and within the core of the nanoparticle, one can expect that the characteristics of photoluminescence from Si nanocrystals are related to both the crystal size and the environment of its surface. After intensive efforts in many research laboratories around the world, a consensus has been reached that both surface defect-related and QC mechanisms play a role, but it is difficult to distinguish the two contributions from each other [23]. Obviously, the optical response of semiconductor nanoparticles is influenced by both particle size and surface chemistry. These factors must be controlled and optimized by any

production methods to obtain best conditions for aging in light emitting properties. Particularly, several techniques [100] have been employed for production of free-standing Si nc but it has been rather difficult to synthesize a very small, spherical, disagglomerated and highly pure nanopowders. The laser pyrolysis technique is the most attractive one for producing such ideal nanopowders. The silane pyrolysis that used a CO₂ laser to decompose the silicon precursor was first reported in 1982 by Cannon et al. [43,44]. This group didn't see the PL behaviour from their products. Significant PL signal upon etching with HF reported by Huisken et al [48, 101] The laser induced SiH₄ pyrolysis is also an efficient method for preparing large quantities of Si nanoparticles at rates of 20–200 mg which reported by Swihart and coworkers. These particles with 5 nm diameter show tunable photoluminescence upon controlling etching with HNO₃–HF [52, 102]. In last decades, a number of groups have studied different aspects of the production of free standing Si nc. Both preparing large amount of free standing Si nc and some ability to tailor shape have been demonstrated [103–105]. But still some important challenges remain. One of them is the reliability of different methodologies on reactors and second one is hazardous chemical processes for effective control over the nanocrystals size. Recently, the role of the reaction sensitizer and of the quenching collection system on the production of very small nanoparticles has been deeply studied by E. Borsella group. The effect of the size and crystallinity of the collected Si-np on the optical emission properties, before and after wet chemical oxidation, has been studied [42]. Freestanding silicon nanoclusters are light emitters with strong luminescence in the wavelength range from red to blue depending on their size [105, 52, 103]. In addition to the crystal size, there are other variables that affect the luminescence properties of FS-nc-Si such as laser induced thermal effect and excitation wavelength. Intense laser light may increase temperature in absorbing materials so the laser heat becomes highly stronger for freestanding nanocrystals [45, 106]. Moreover, freestanding nanocrystals show emission fluctuation which is called photoluminescence bleaching and PL intermittency: ON-OFF blinking. Briefly it

is fluctuation of the photo-luminescence signal from Si nanocrystals under laser exposure with the duration of the order of ten seconds [107, 108].

In this chapter, we focus on photoluminescence and Raman properties of freestanding Si nanocrystals prepared by laser pyrolysis technique at Borsella group. The production and oxidation processes of free standing Si nc have been described in chapter 2. Here, the term “freestanding” is used for structures which do not require full contact with a solid substrate to sustain their shape and properties. We performed temperature dependent photoluminescence by using two different lasers. Fluctuation of photoluminescence was studied as a function of time and temperature. In order to study of structural properties, we report Raman spectra and TEM images. This information is valuable for discussions on light-emission mechanism of this material.

6.2. Temperature dependent photoluminescence properties of Free-standing Si nanocrystals.

The optical properties of the free standing Si ncs were investigated by using UV–visible PL spectroscopy. PL spectra of free standing Si excited with NdYAG laser is shown in Figure 6.1 for both as prepared and oxidized powders at 300 K. The nanoparticle size is equal to 6.0 nm before oxidation, and then it decreases to 5.9 nm after oxidation [42]. One can see the dramatic blue shift after chemical oxidation processes. This is evidence of more and small Si nanocrystalline structure in the oxidized sample rather than as-prepared one.

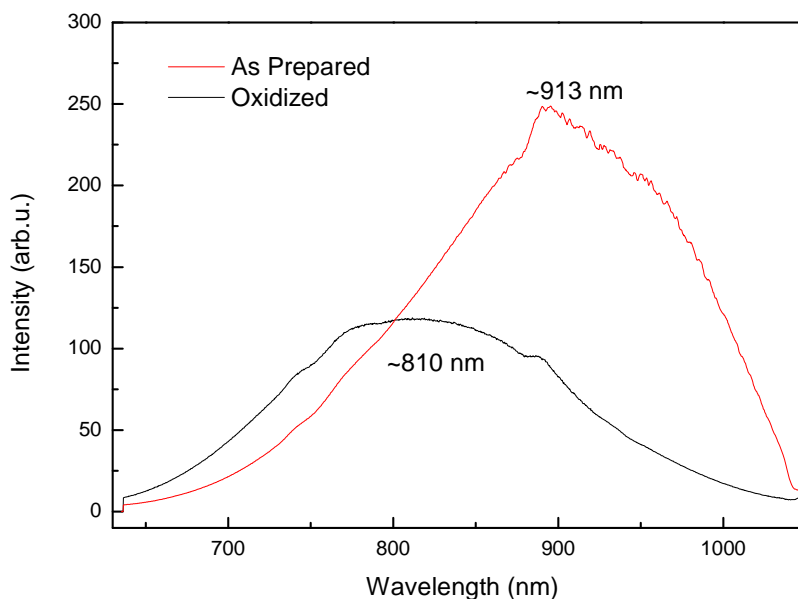


Figure 6.1. Photoluminescence spectra of as prepared sample and oxidized sample, at 300 K. NdYAG laser, 532 nm, was used as an excitation source.

Free standing Si nc has been studied through the temperature dependent photoluminescence spectroscopy. The PL behavior of Si nc strongly depends on the temperature and excitation wavelength. In particular, the PL intensity was found to be increasing with decreasing temperature, which is contrary to what is commonly observed for the nanocrystals embedded in a matrix. It should be noted that all analysis was made by considering the relative intensity of photoluminescence experiments and all spectra was taken under same conditions. Temperature dependence of PL spectrum is shown in figures 6.2 and 6.3 before and after oxidation, respectively.

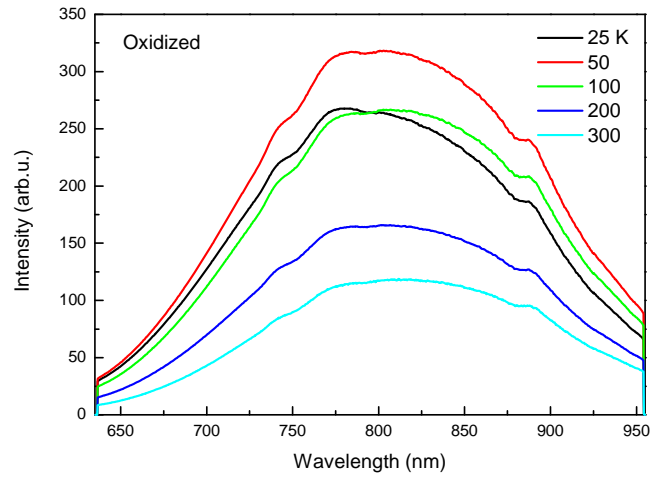


Figure 6.2. Photoluminescence spectra of oxidized sample with respect to different temperature.

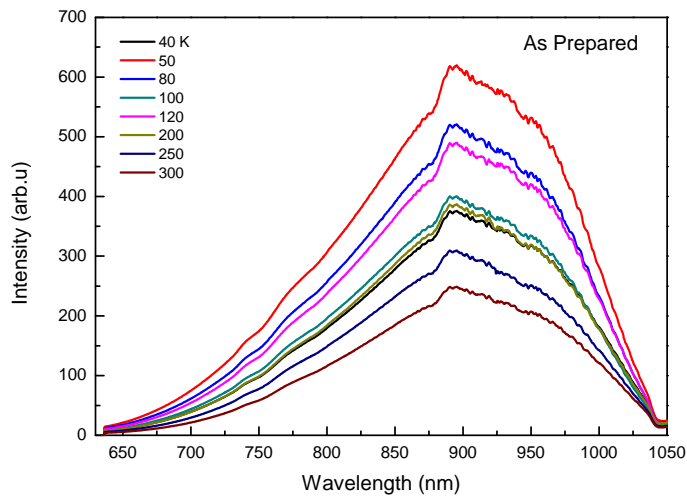


Figure 6.3. Photoluminescence spectra of as prepared sample with respect to different temperature.

Figure 6.4 shows the peak position intensity as a function of temperature for oxidized and as prepared sample. The PL intensity of the samples increases with decreasing the temperature down to a certain value but below this temperature, it

starts to decrease. This critical temperature is at around 50 K for the samples studied here.

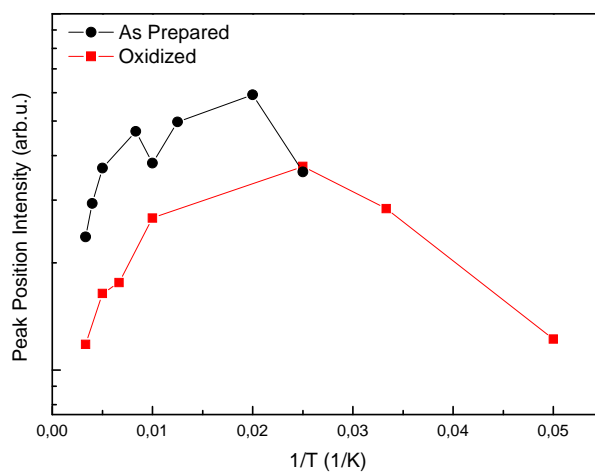


Figure 6.4. PL emission maxima intensity as a function of $1/T$.

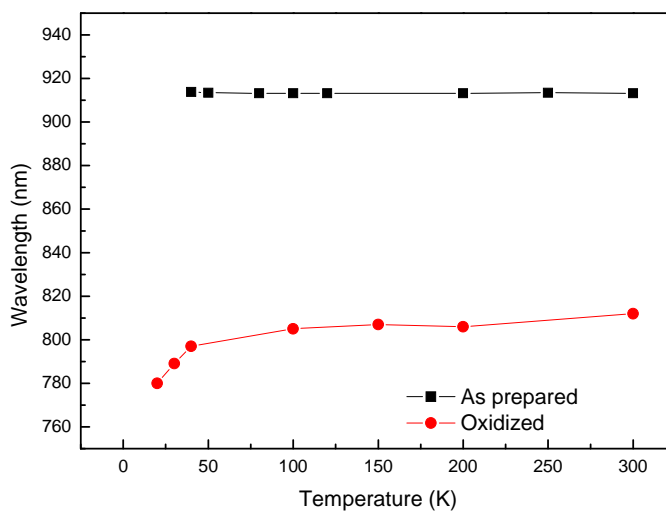


Figure 6.5. Wavelength of PL emission maxima as a function of temperature.

The peak position of oxidized sample shifts slightly to the higher wavelengths while the temperature increases. However, there is no shift with increasing temperature for as-prepared samples. This behavior is shown in figure 6.5. In order to see the different light emitting components to the total measured signal a deconvolution process has been applied to the PL spectra of both as prepared and oxidized samples. The deconvoluted PL spectra for oxidized sample are shown figure 6.6. Here, we identify four components centered at ~ 690 nm, ~ 790 nm, ~ 845 nm, and ~ 980 nm. Temperature dependence of these peaks is indicated in figure 6.7. The peak centered at ~ 790 nm has highest intensity. All peaks show nearly same behavior as a function of temperature.

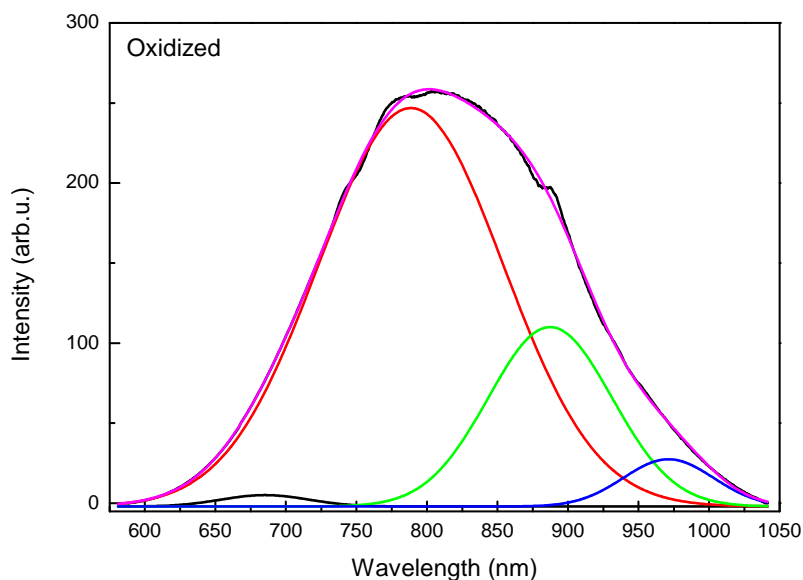


Figure 6.6. Deconvolution spectra for oxidized taken with NdYAG Laser at 300 K. PL spectra are deconvoluted by four peaks and labeled as follows black is Peak 1, red is Peak 2, green is Peak 3, and blue one is Peak 4.

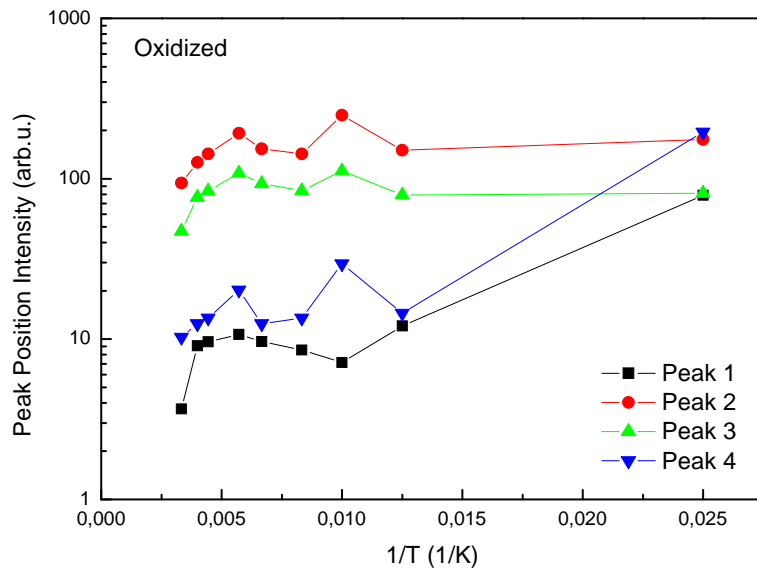


Figure 6.7. PL emission maxima intensity as a function of $1/T$ for oxidized sample..

The deconvoluted PL spectra the as-prepared sample is shown in Figure 6.8. PL spectra are deconvoluted by four peaks and labeled as follows Black is Peak 1, red is Peak 2, Green is Peak 3, and Blue one is Peak 4. Similarly we identified four different PL peaks studied them as a function of the temperature. The PL intensity of the samples increases slightly with decreasing the temperature down to 100 K, but below this value, it decreases as shown in figure 6.9.

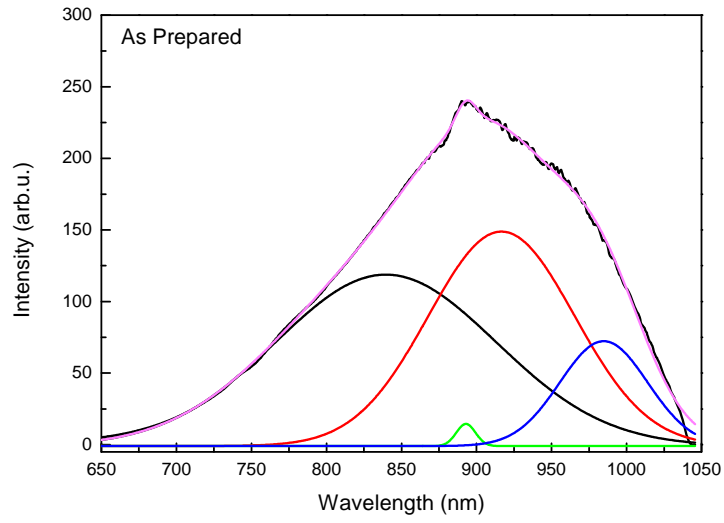


Figure 6.8. Deconvolution spectra for oxidized sample taken with NdYAG laser at 300 K.

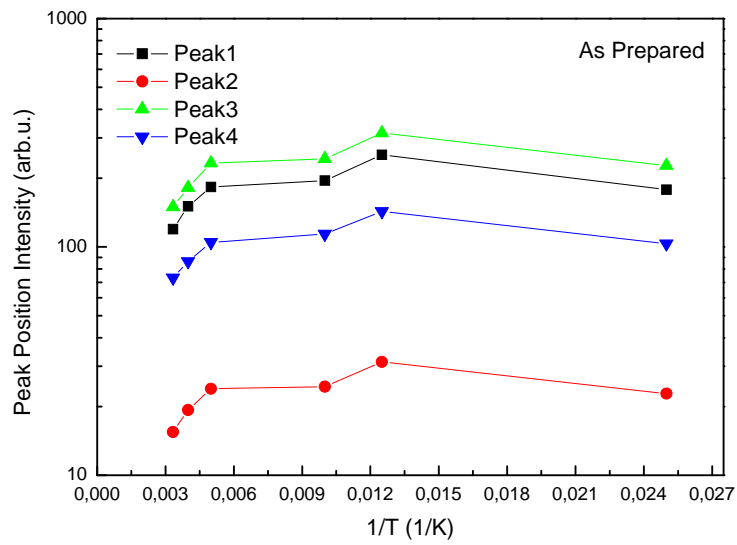


Figure 6.9. PL emission maxima intensity as a function of $1/T$ for as prepared sample.

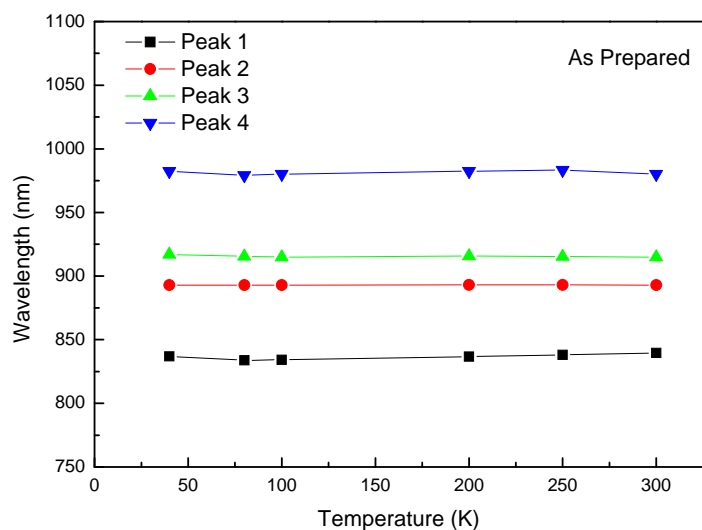


Figure 6.10. Wavelength of PL emission maxima as a function of temperature.

Photoluminescence spectra were also measured with HeCd laser operating at 325 nm as a function of temperature, and the results are depicted in figure 6.11. As the temperature increases, the intensity of PL spectra decreases significantly. Photographs of photoluminescence observed for oxidized sample upon exposure to a UV light, HeCd laser, can be seen in the inset of figure 6.11. As shown in the picture, nanopowders have bright and intense luminescence that can be seen with naked eye. If we compare the emission spectra taken by 532 nm line of NdYAG laser and HeCd laser, there is significant blue-shift in PL spectra as shown in figure 6.12. The shift of the PL with excitation wavelength results from the excitation of different sizes of nanocrystals that have different optical transition energies, thus confirming size-dependent energy levels consistent with a quantum confinement model. The size distribution is evident from the emission of the sample over a range of energies in the visible region.

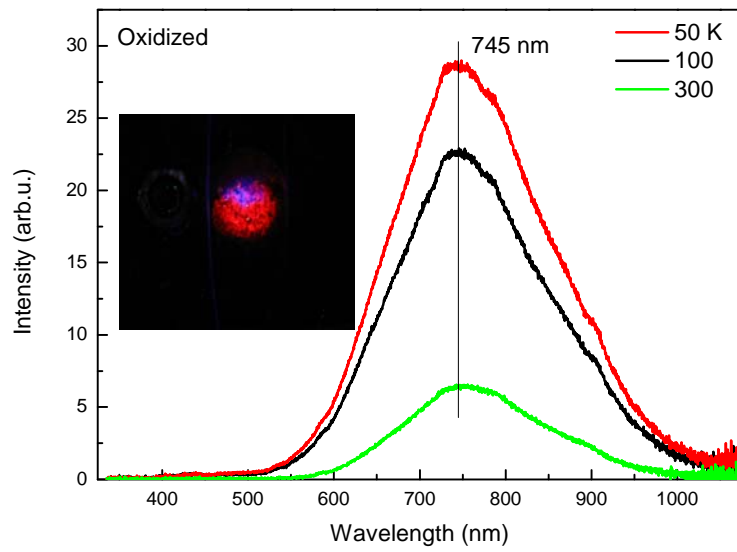


Figure 6.11. Photoluminescence spectra of oxidized sample with respect to different temperature conducted by HeCd Laser, 325 nm.

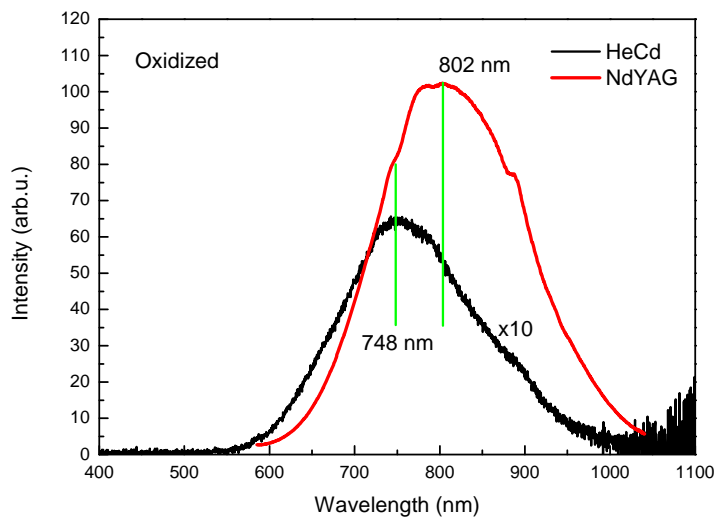


Figure 6.12. Photoluminescence spectra of oxidized sample with respect to different excitation wavelength at 300 K. (NdYAG, 532 nm and HeCd, 325 nm)

We also performed a multi-Gaussian fitting procedure in order to separate the 4 different components of the emission peaks for the oxidized sample excited by HeCd Laser at 300 K which is shown in figure 6.13. The fitting procedure is performed in the wavelength range from 400 nm to 1100 nm. PL spectra are deconvoluted by four peaks and labeled as follows Black is Peak 1, red is Peak 2, Green is Peak 3, and Blue one is Peak 4. The peak position, of each PL bands report in figure 6.14 as a function of temperature. While the temperature increases the intensity of each band decreases.

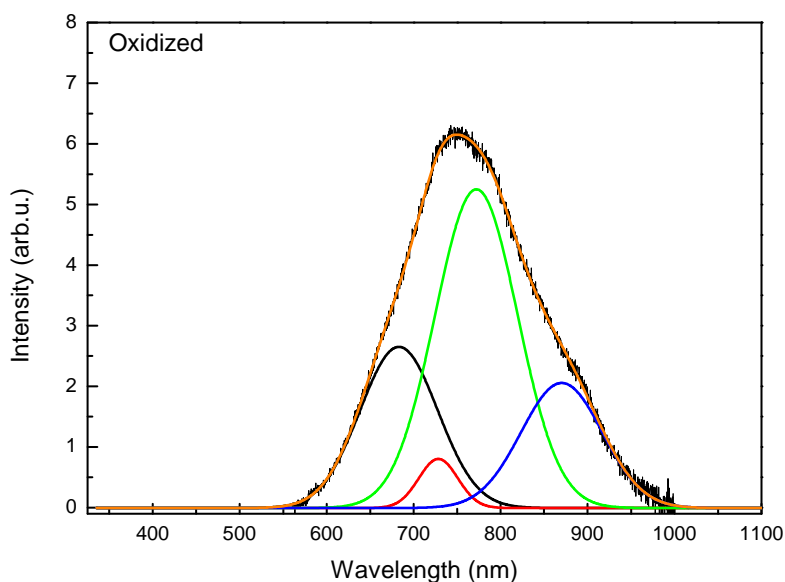


Figure 6.13. Deconvoluted spectra for oxidized taken with HeCd Laser at 300 K.

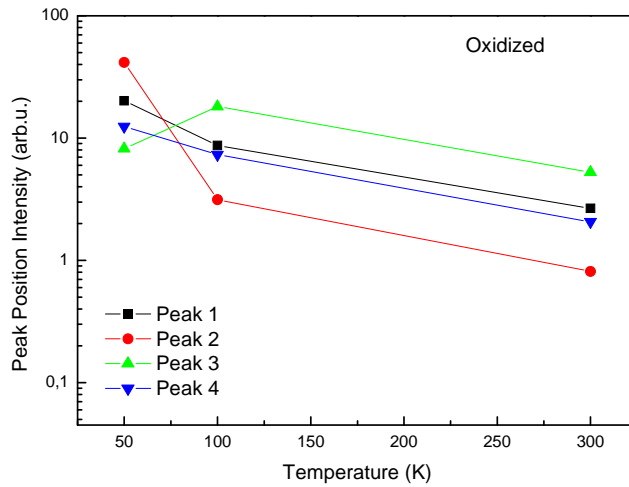


Figure 6.14. PL emission maxima intensity as a function of temperature for oxidized sample.

6.3. Photoluminescence Experiments as a function of Time

During the PL experiments, we noticed that the photoluminescence intensity varies with the time. Here, we should emphasize that the temperature-dependent measurements were consistent within itself because all measurements were taken under the same condition and compared relative to each other. In order to investigate variations in the PL intensity, we conducted a series of photoluminescence experiments as a function of time at the wavelength of maximum PL intensity. The PL intensity decreases sharply in a few seconds then stabilize around some value as shown in figure 6.15. When the laser power intensity is increased, the photoluminescence intensity also increases correspondingly, while the same characteristic is observed in the intensity variation. The interesting point is that the photoluminescence intensity recovers itself after some time upon switching the laser power off. A summary of this behavior found from PL measurements is depicted in figure 6.16. This experiment was conducted by measuring the intensity as a function of time and the full recovery of PL intensity was observed after 1 hour.

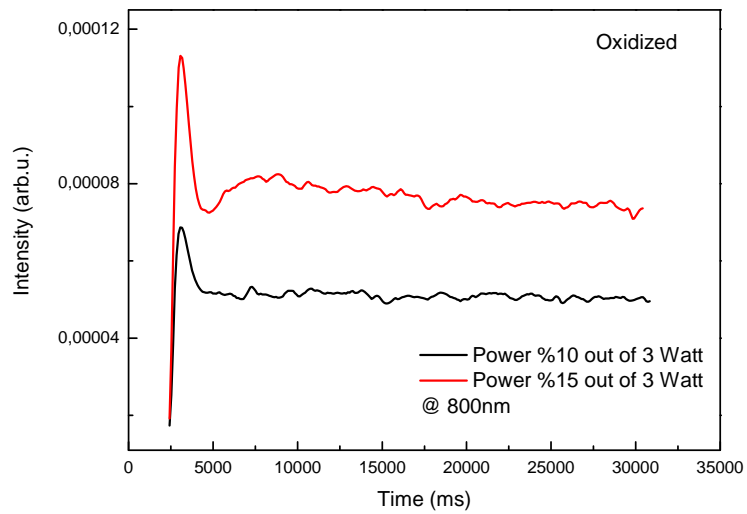


Figure 6.15. PL intensity of the emission at 800 nm under continuous irradiation (NdYAG laser) as a function of time

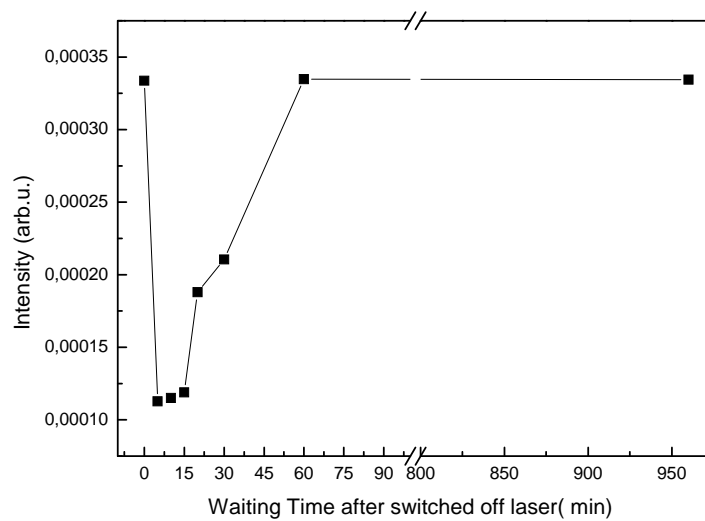


Figure 6.16. Recovery PL intensity of the emission at 800 nm as a function of time.

The first question about this observation whether or not this behavior is related to the thermally induced structural change. Laser light can increase temperature in the illuminated volume, which might lead to some structural transformations. It has been reported that the intense laser light increases the absorption and cause to

nonlinear rise of light emission [109]. Therefore the laser heat becomes very important for luminescence properties of freestanding nanocrystals [106]. However, in the present case, the fluctuation of PL is found to be reversible. In order to be sure about this behavior is not resulting of laser annealing; we performed photoluminescence experiment by continuously exposing the sample during 150 minutes and recorded PL intensity for every 5 minutes. As one can see in figure 6.17, during the laser exposure the PL intensity is almost same. If it is laser induced effect, we should observe drastic change in intensity. The results indicate that the fluctuation of PL intensity is independent of laser annealing.

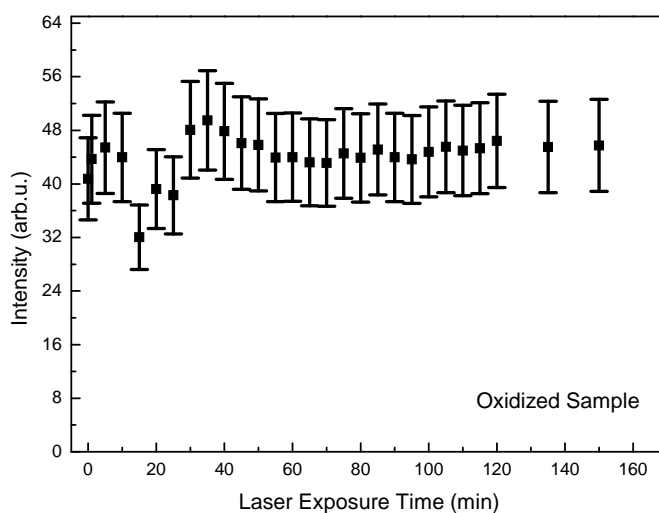


Figure 6.17. PL intensity of the emission under continuous irradiation with NdYAG laser as a function of time.

In order to check low temperature behavior of intensity, samples cooled and photoluminescence spectroscopy study was carried out as a function of time by using two different lasers. At low temperatures, the PL intensity again decreases by showing different exponential decay. This result is reported in figure 6.18 and 6.19 for the oxidized sample measured by UV and visible illumination, respectively. PL intensity recovers itself after waiting for a while and stabilization

of the intensity takes longer time than those measured at room temperature. The low temperature decay of the PL intensity as a function of time suggests the presence of two possible mechanisms. The first one is a faster decay occurring immediately after laser exposure while the second one is a slower process which is dominating the decay process after some time. These two different decay mechanisms suggest that there are two different trapping sites for the carriers as discussed below. Probably, at low temperature, an electron trapping takes longer time for one of these sites.

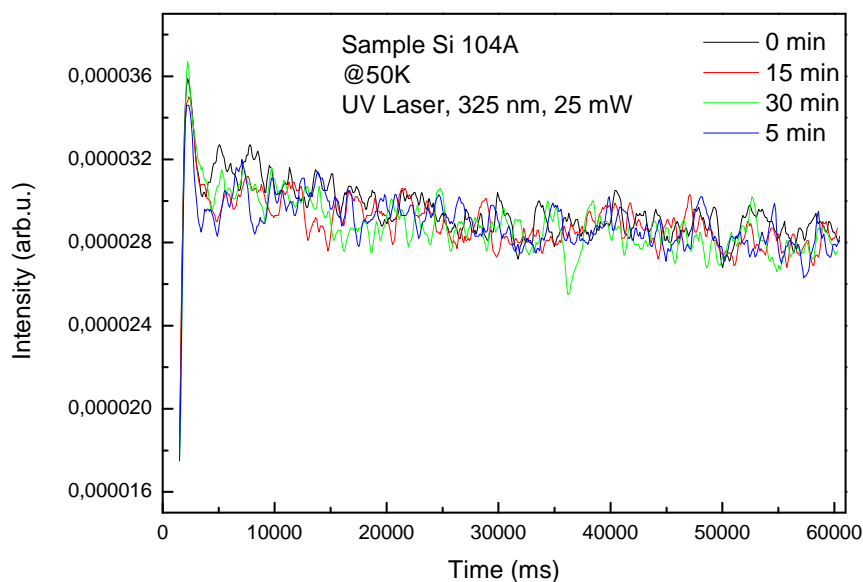


Figure 6. 18. PL intensity of the emission at 744 nm under continuous irradiation (HeCd laser) as a function of time at 50 K.

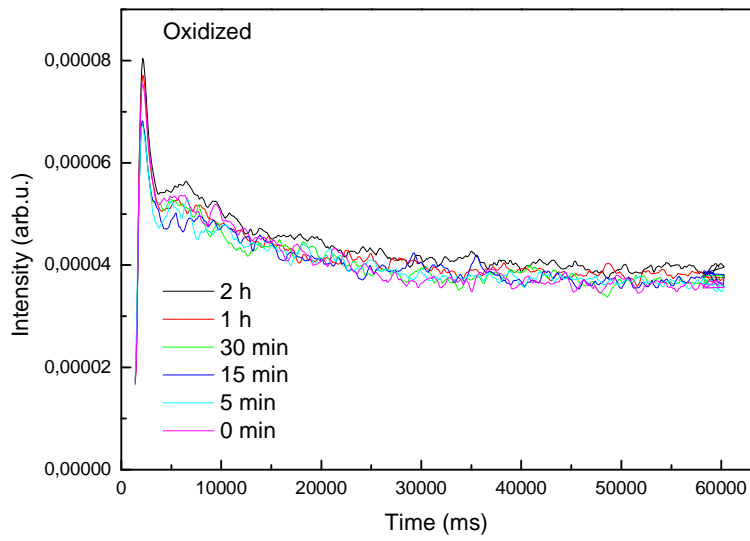


Figure 6.19. PL intensity of the emission at 775 nm under continuous irradiation (NdYAG laser) as a function of time at 100 K.

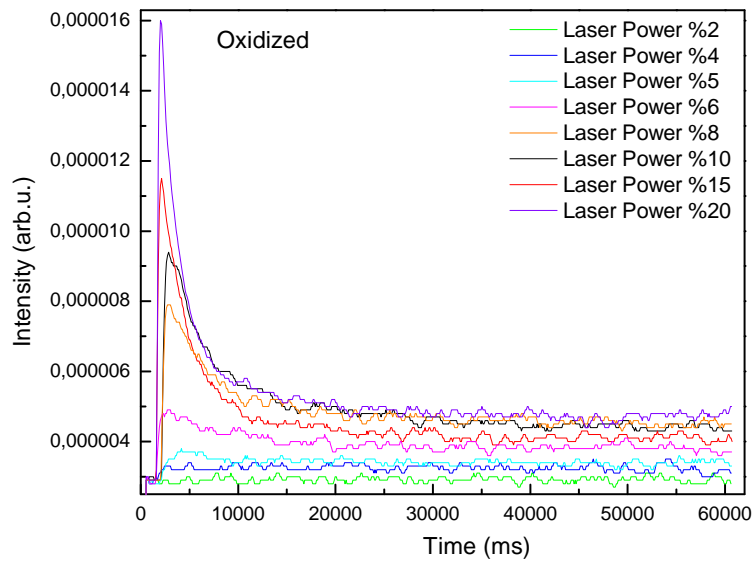


Figure 6.20. PL intensity of the emission at 800 nm under continuous irradiation (with respect to Ndyag laser power) as a function of time at RT.

In order to see the effect of laser power, we have performed PL measurement as a function of laser power. Results are shown in Figure 6.20 and 6.21 for oxidized and as prepared samples respectively. We observe that the PL decay decreases with decreasing laser power. We did not see fluctuation below certain laser power. We have studied the dependence of the decay on the PL wavelength as shown in Figure 6.22. Although the PL intensity varies with the wavelength, the intensity decay exhibits the same behavior for all three wavelengths.

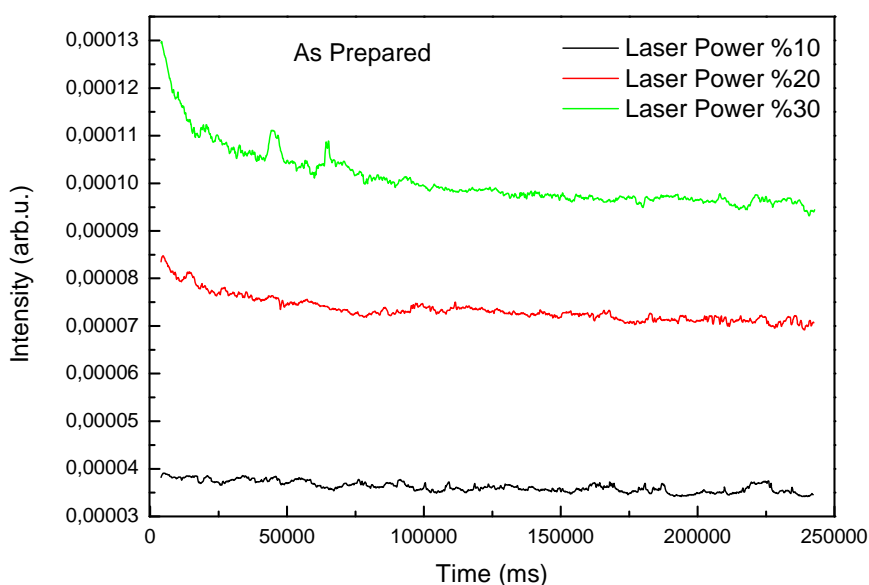


Figure 6.21. PL intensity of the emission intensity as a function of time under continuous irradiation with different laser power.

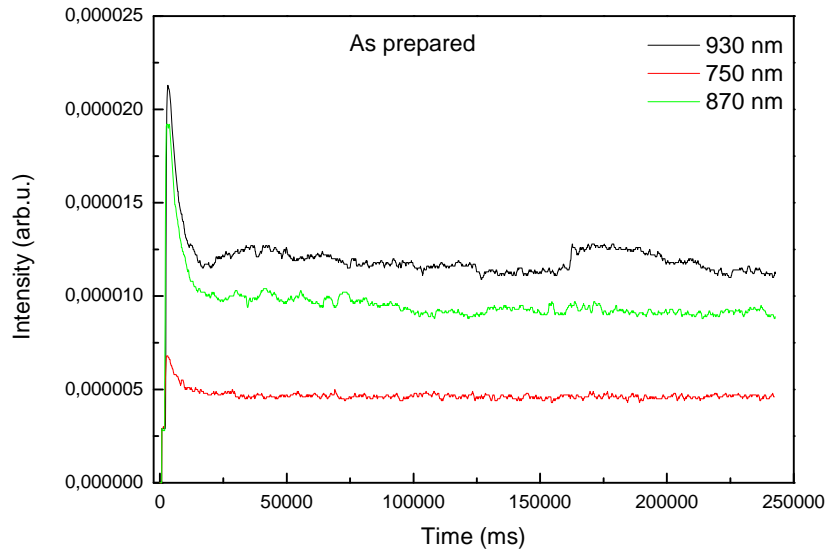


Figure 6.22. PL intensity of the emission intensity as a function of time under continuous irradiation with different observation wavelength at RT.

6.4. Photoluminescence bleaching and possible mechanisms for the observed intensity decay

A possible origin of the observed intensity fluctuations can be bleaching or photoluminescence intermittency: ON-OFF blinking. Photoluminescence blinking and bleaching were frequently observed under continuous-wave (cw) laser excitation and can be mainly attributed to interactions of the Si nanocrystals with its local environment [107]. Briefly, photoluminescence blinking of nanocrystals is caused by a random switching between light-emitting “on” and non-light-emitting “off” states even under continuous-wave (cw) laser excitation. Power and exponential dependence is the key indication for understanding of the blinking mechanism ($P(t) = const. t^{-1.5} e^{\left(-\frac{t}{\tau}\right)}$). This model is explained as follows (shown in figure 6.23): electron- hole pairs, forming a confined exciton, are generated by absorbing a photon. Nanocrystals confine exciton tightly but it is possible that it penetrates to a region with complicated energy profile and could

come across a nonradiative center. Thus, the average QE of radiative recombination is reduced. By taking into account of the slow PL decay for SiNCs together with high QE of the radiative recombination occurring in SiNC (in ON state) a second exciton is highly expected to be produced while the other is still around so that there could happen an exciton-exciton scattering. Such scatterings should essentially affect both radiative and nonradiative recombination processes. Nonradiative recombination of exciton can be induced by the inelastic scattering. The Auger recombination is for example another way to create the effect when an exciton recombines with a third quasiparticle. A charge separation could happen under appropriate conditions. The Auger recombination effectively destroys the excitons produced in the charge separated state which leaves the NC dark until the next charge recombination takes place [108].

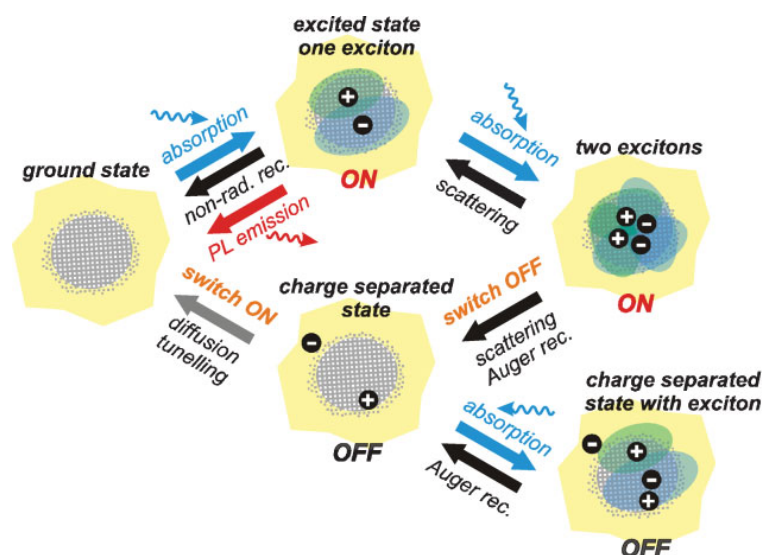


Figure 6.23. “Schematic illustration of processes involved in the radiative and nonradiative recombination of a single Si nanocrystal” [108].

The bleaching phenomena are closely related to blinking process of the PL measurement. The bleaching can be described by the time dependent emission intensity of particles which are on state at a certain time. The bleaching process

shows reversible characteristic after switching off the excitation on a long time scale. The bleaching curve of silicon nanocrystals are well fitted with power law according to $I = I_0(t + \tau_0)^{-\beta}$, where τ_0 is related to the mean on time and β is empirically found to follow $\beta = 2 - \alpha_{\text{off}}$, where α_{off} is the exponent of the off time statistics. Therefore it is possible to predict the bleaching of nanocrystal ensembles from the blinking statistics of single nanocrystals [107]. In general, the bleaching in Si nanostructures is attributed to a blinking process which is observed in a single nanoparticle populated by more than one exciton under strong laser illumination [107, 108]. It should be noted that, bleaching and blinking of PL upon strong laser irradiation is often observed, however the underlying mechanism is not fully understood. This phenomenon of Si nanocrystal emission intermittency is related to the nature of the trap states at the interface between nanocrystal and the surrounding oxide layer. According to our results, we suppose that the observed PL intermittency is the combination of PL blinking and bleaching mechanisms, since our measuring system does not allow focusing on single nanoparticle, which facilitate observation of blinking.

As described above, blinking is a result of charge trapping at the trap states located at the interface or in the SiO₂ shell surrounding the nanocrystal. A nanocrystal can be at ON or OFF state depending on whether an electron is trapped or not. If a nanocrystal stays longer time at the OFF state than ON state the overall PL intensity generated by an assembly of nanocrystals will decay with time. This PL intensity will approach a constant value after a steady state trapping and de-trapping process has been established.

A visual summary of the possible mechanism for the observed PL decay for the oxidized sample is shown in Figure 6.24.

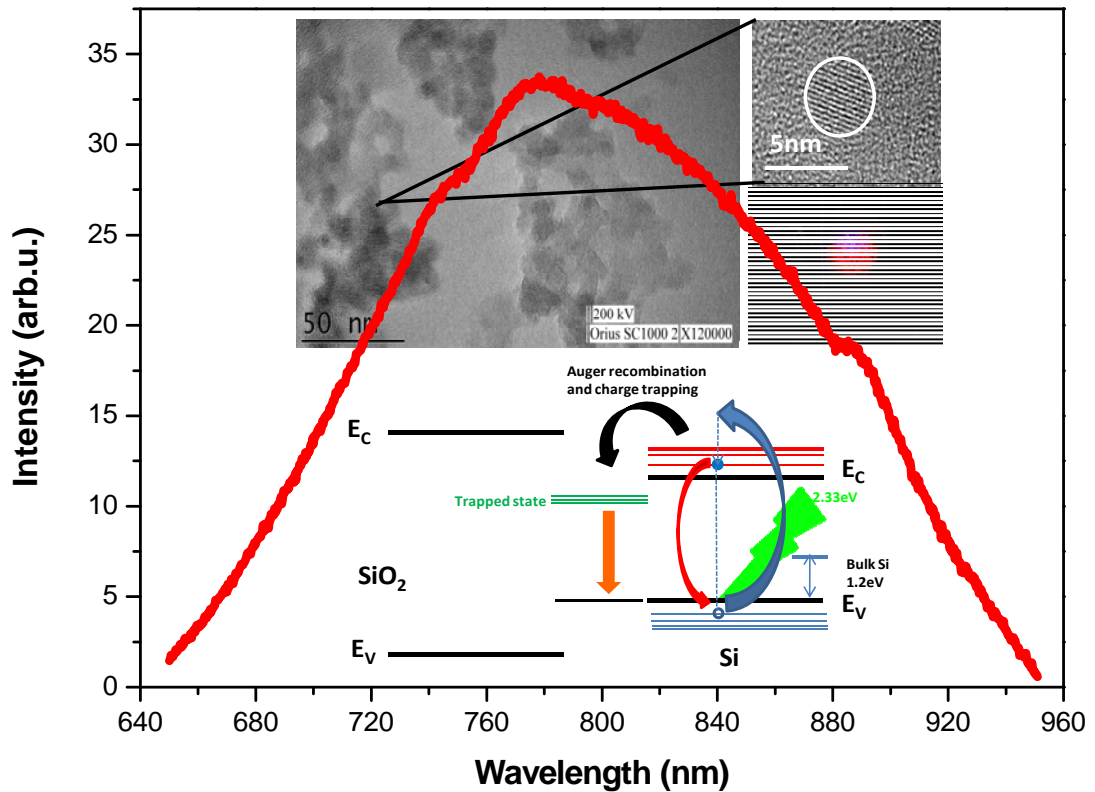


Figure 6.24. The colored arrows indicate the recombination ways for an excited electron. Green arrows: excitation with photons by using 2.33 eV light . Blue arrows: indirect absorption. Red arrows: indirect radiative recombination (with the assistance of a phonon). Black arrow: Auger recombination. Orange arrows: nonradiative recombination mechanism.

6.5. Raman Spectroscopy

Raman spectroscopy is a powerful tool to study the vibrational dynamics and bonding of amorphous and crystalline solids, and it has been also extensively applied for silicon materials.

In general, a broad Raman band around $\sim 470 \text{ cm}^{-1}$ is an evidence for the presence of amorphous silicon [110]. It also indicates that Si excess in SiO_x is not distributed homogenously so that amorphous Si agglomerates are formed.

Additionally, if there exists, with annealing, a narrowing as well as up-shifting of Raman bands as shown in Fig. 6.25, there is strong possibility that Si crystallization occurs [111].

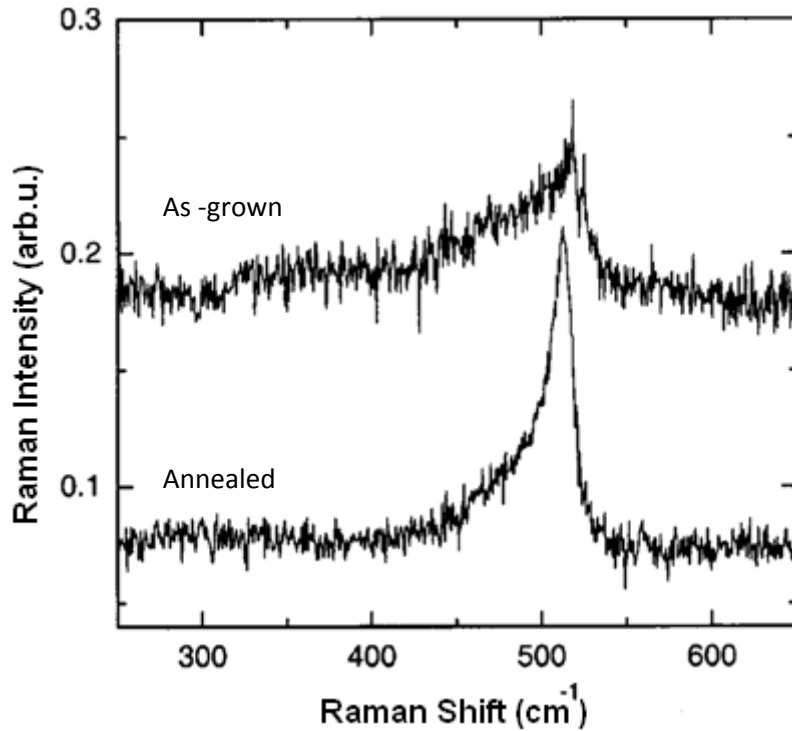


Figure 6.25. The Raman spectra of as-grown and annealed sample for a Si/SiO₂ superlattice [112].

The change of the Raman band position can be explained by the stress in the lattice. It is well known that a compressive stress generated by the surrounding matrix causes an increase in the phonon frequency and therefore there exist an up-shift in the relative wavenumber of the first-order Stokes line and the situation is reversed for a tensile stress, which is mentioned in chapter 2. Additionally, the phonon confinement model suggests that unstressed 4-nm Si nanocrystals scatter at 517-518 cm⁻¹ with a bandwidth of ~12 cm⁻¹ [112-116]. 4-nm is the lower limit of the Si-nc size based on possible stress and size distributions.

The Raman shift in wavenumber decreases related to the reduced dimensionality as well as the stress which are originated from the quantum confinement of the ensemble of Si NC's. In fact, in addition to the two effects, there is also another important possibility that is caused by the local temperature of the point on the sample where the laser beam is exposed [117].

In order to investigate the contributions of laser annealing and laser heating to the PL bleaching we performed the Raman Spectroscopy to our samples. Raman scattering spectra were taken on a confocal micro-Raman (HR800, Jobin Yvon), attached with Olympus microanalysis system and a charge-coupled device (CCD) camera providing a resolution of $\sim 1 \text{ cm}^{-1}$. The spectra were carried out in backscattering geometry with the 632.8 nm line of He-Ne laser at room temperature.

To perform Raman study, we have used two samples; free-standing as-prepared and oxidized Si nanopowders. The Raman spectra of the as-prepared and oxidized Si nanocrystals are shown in figure 6.26. The Raman band of oxidized Si nanocrystals is slightly narrower and stronger than the bands of the as-prepared one.

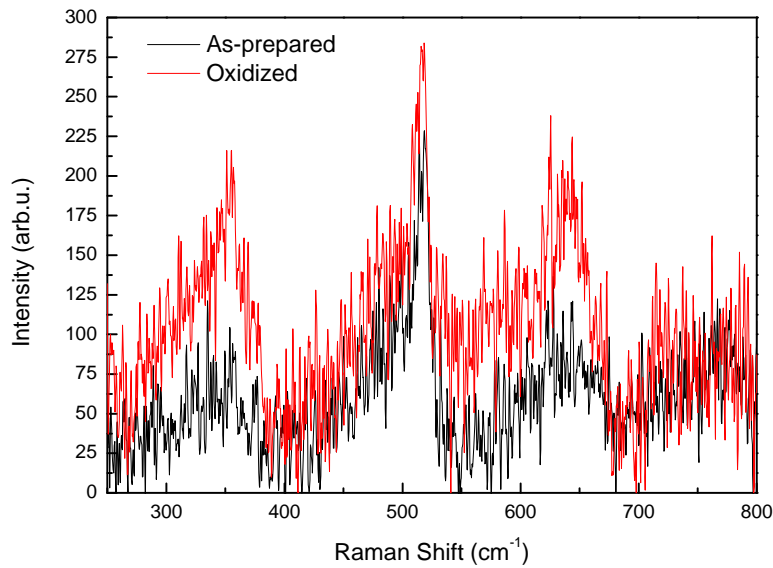


Figure 6.26. Raman spectra of the as-prepared and oxidized free-standing Si nanocrystals.

Raman spectroscopy exhibits a four-band structure so that it can be fitted by the use of four Gaussians as shown in Figure 6.27. The Raman spectrum gets broader and asymmetrical as the wavenumber decreases. By considering the 400-550 cm^{-1} part of the Raman spectra, we found that there is a broad lower-energy band centered at 490–500 cm^{-1} (Peak 2) [110], which is resulted from amorphous structures, and a narrow high-energy peak centered at 514–516 cm^{-1} (Peak 1), which is due to the bindings between Si nanocrystals [112, 115]. In addition to the broad signal, Peak2, on the lower wavenumber part of the spectrum near 350 cm^{-1} , there are two additional peaks (Peak 3, Peak 4) for both as-prepared and oxidized Si nanopowders as seen in figure 6.27.

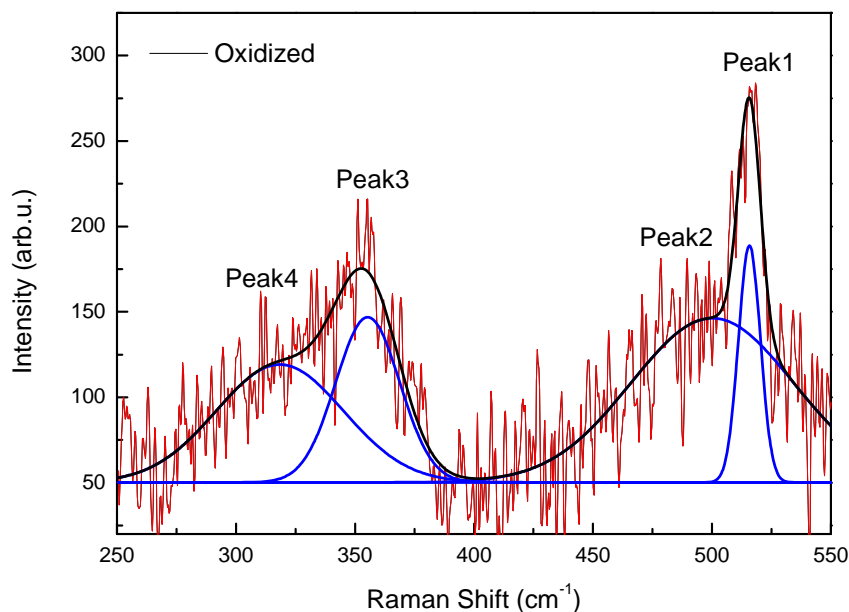


Figure 6.27. Deconvolution of Raman spectra for oxidized free-standing Si nanocrystal.

To make sure that the laser annealing effect is not responsible for the decrease in the PL intensity the Raman spectroscopy measurements were performed for both as-prepared and oxidized samples by first exposing continuous wave Nd-YAG laser on the samples for a while. The results for the laser exposed samples are reported in Figure 6.28. As seen from this figure, the position and width of the Raman bands do not change significantly. Thus, it seems that there is no measurable change in the size of the nanocrystals for both as-prepared and oxidized free-standing Si nanopowder samples measured with continuous wave laser radiation with %10 of total power (3 Watts). However, increase in the Raman signal indicates an improvement in the crystallinity of the nanocrystals.

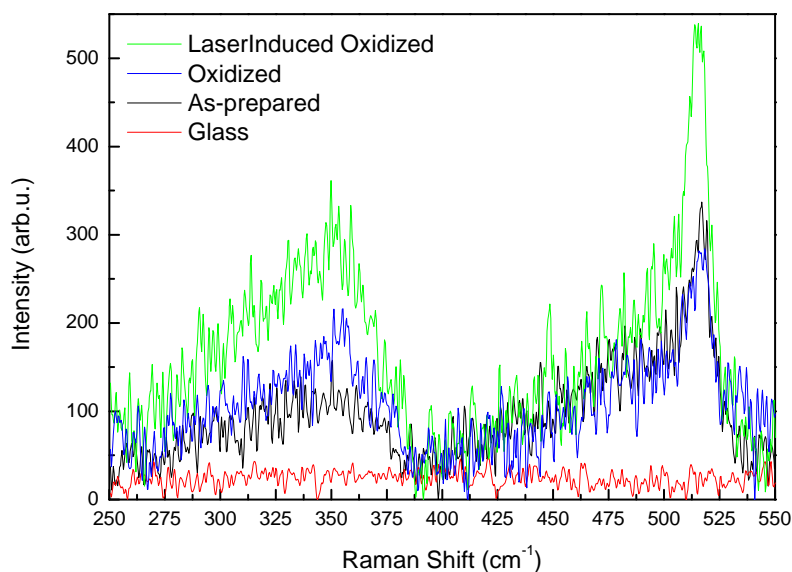


Figure 6.28. Comparative Raman spectra of the laser induced oxidized free-standing Si nanocrystals according to oxidized and as prepared sample.

In order to have a complete picture of the Raman spectra it is worth comparing the deconvoluted peaks for all samples reported in table 6.1. The Raman spectra are deconvoluted by four peaks labeled as Peak 1, Peak 2, Peak 3, and Peak 4, shown in Figure 6.27. One can conclude from table 6.1. The following:

- In the as prepared sample, there is no significant shift and broadening after laser irradiation for the Peak 1 (centered at $\sim 515 \text{ cm}^{-1}$). On the other hand, the Peak 2 shifts towards to higher wavenumber from 484 to 498 cm^{-1} .
- In the oxidized sample, we observe the same behavior for the Peak 1 as in the as prepared sample. Unlike to the as prepared case, the Peak 2 shifts towards to the lower wavenumber with the laser power increasing (The peaks at $500, 490, 480 \text{ cm}^{-1}$ for the oxidized, the laser %10 and the laser %30 of 3 Watt, respectively)
- In general, the Peak 1 has approximately same position and width for all the case but the Peak 2 shifts towards to higher wavenumber after certain

oxidation processes take place. Existing of such shifts in the spectrum is in fact indicating the formation of Si nanocrystals in the system.

- In general, the Peak 1 has approximately same position and width for all the case but the Peak 2 shifts towards to higher wavenumber after certain oxidation processes take place. Existing of such shifts in the spectrum is in fact indicating the formation of Si nanocrystals in the system.

Table 6.1. The deconvolution parameters of the Raman spectra for all samples.

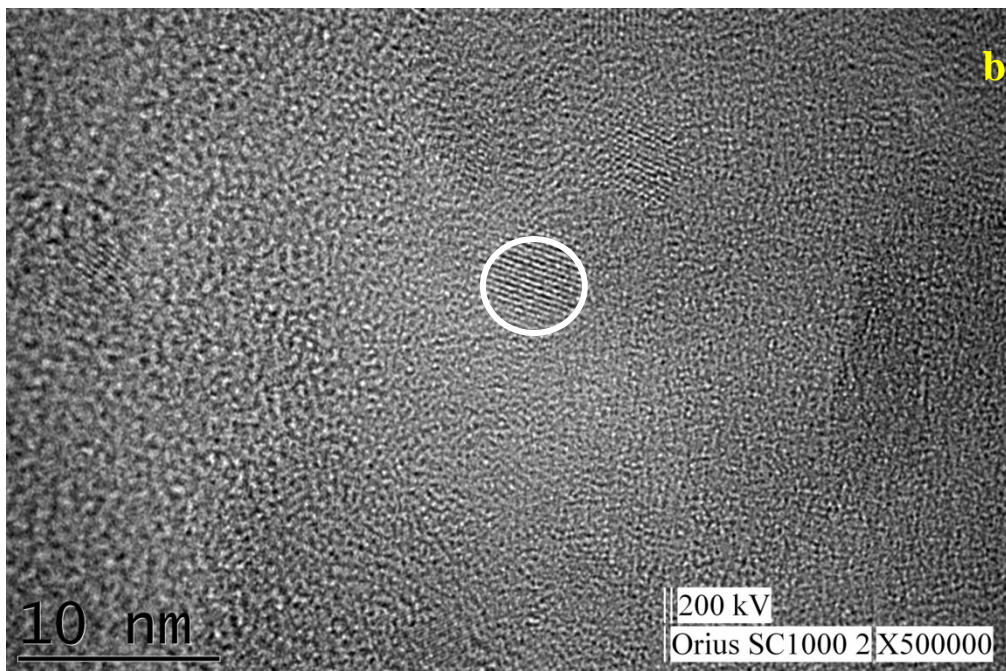
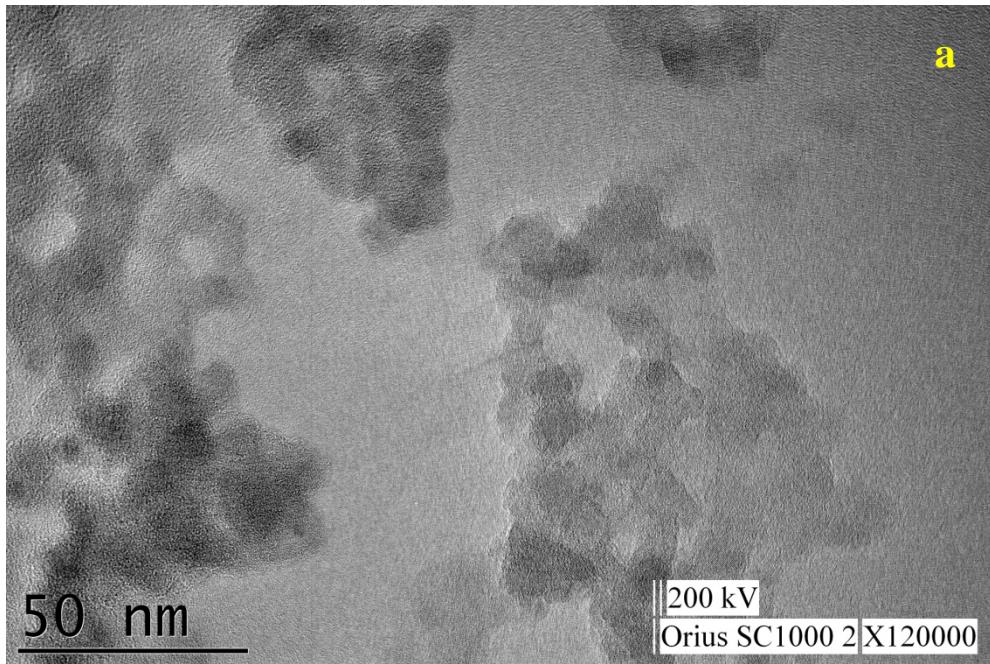
		Area	Center (cm ⁻¹)	Width	Height
As-prepared	Peak1	2623,6	515,9	11,0	191,2
	Peak2	7454,5	484,1	55,2	107,8
	Peak3	3650,4	352,7	39,8	73,1
	Peak4	3001,2	306,9	51,5	46,5
Oxidized	Peak1	1609,8	515,7	9,3	138,7
	Peak2	8281,8	500,1	68,8	96,1
	Peak3	3171,4	355,4	26,6	95,1
	Peak4	4629,9	319,0	53,8	68,6
Oxidized, Laser Irradiated (%10,150 min)	Peak1	4693,3	515,0	10,3	363,6
	Peak2	8590,5	490,4	48,0	142,7
	Peak3	6395,4	353,6	31,3	163,0
	Peak4	12328,8	316,4	64,5	152,6
Oxidized, Laser Irradiated (%30,4 min)	Peak1	4105,9	515,2	10,7	305,6
	Peak2	6614,0	480,5	54,9	96,1
As-prepared, Laser Irradiated (%30,4 min)	Peak1	1708,9	516,8	9,6	141,7
	Peak2	7710,9	498,4	62,1	99,0

Following the literature, it is argued that under intense laser irradiation the structural reorganization can be seen in Si material which is called Laser Annealing (LA) [118]. The laser light can heat the illuminated region up. At

higher excitation powers (higher temperature), the Raman bands shift towards to lower wavenumber and with a broaden width due to the phonon confinement effect [112, 115]. However, we have observed different behavior than in the literature [27]. For example there are no variations in the Raman spectra except that of Peak 2 which shows similarity to those reported in the literature. We may conclude from the Raman results that the cw laser irradiation can make the Si-nc inclusions better ordered. These results demonstrate an improvement in the quality of the Si nanocrystals. It can also be seen from our results that the laser irradiation and its effect on the samples are not responsible for decreasing PL intensity in time.

6.6. Transmission electron microscopy (TEM)

TEM eliminates many ambiguities associated with optical spectroscopic techniques and provides direct estimate of the nanocrystals size, interface quality, etc. The structural and compositional characterization of free-standing Si nanopowders by high resolution transmission electron microscopy because HRTEM allows having deeper information on crystalline structure of Si nc. These observations show that free-standing nanopowders consist of many Si nanocrystals. Figure 6.29 shows HRTEM bright field images of free-standing Si nanopowders for oxidized sample. The lattice fringes in the image clearly indicate that the nano dots are crystalline in nature and have an average diameter of approximately 3-5 nm as seen in Figure 6.29 (b) and (c). In addition to individual Si nanocrystals, one can see the agglomerated Si with amorphous structure in Figure 6.29 (a).



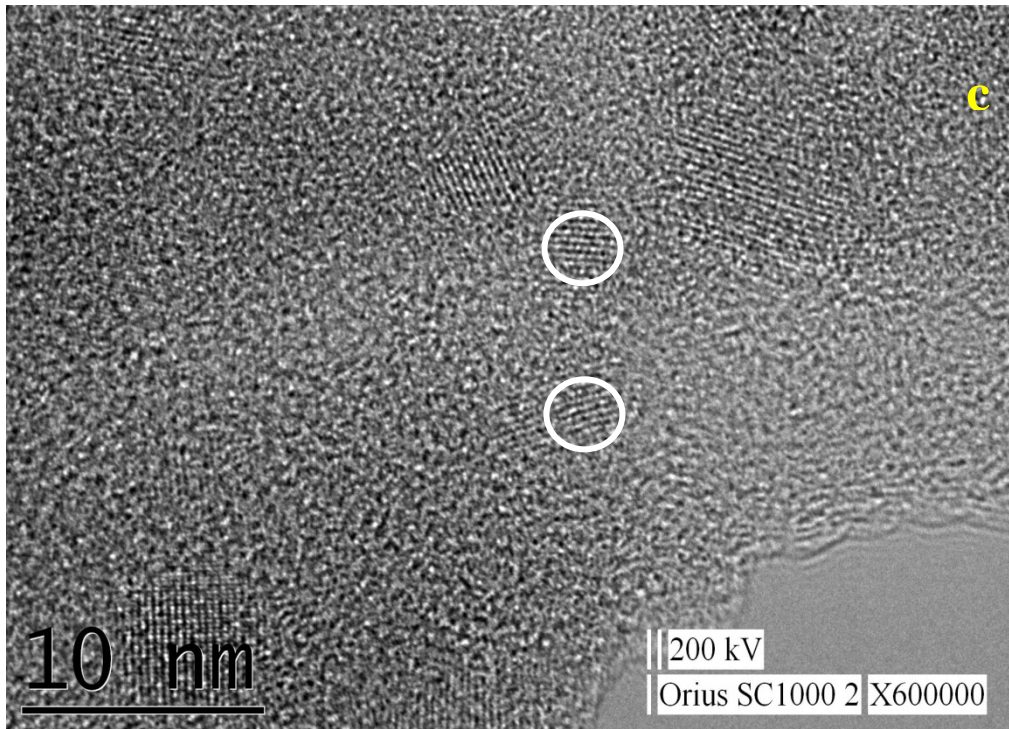


Figure 6.29. The HRTEM image of free-standing nanopowders containing Si nanocrystals. a) agglomerated free-standing Si nano particles., b) Si-nc with diameter ~5 nm, c) Si-nc with diameter ~3 nm.

6.7. Conclusion

In this chapter we have presented photoluminescence experiments performed in freestanding Si nanocrystals using temperature dependent photoluminescence spectroscopy. The main findings are summarized a few points:

- PL spectrum of nanopowders show board shape band that fitted four Gaussian peaks. Cryogenic experiments performed down to 20 K and the main peak shifted towards to higher energies.
- The emission PL spectra were collected with using two excitation wavelengths 325 nm and 532 nm. A size-dependent luminescence property is observed in the PL spectra as expected. The observed blue shift (45 nm)

in PL maximum can be attributed to quantum confinement effects arising from decreased particles size.

- The high resolution transmission electron microscopy images confirmed the presence of both crystalline and amorphous nanoparticles with an average diameter of 5 nm. The chemical structure of the nanoparticles was identified by Raman spectroscopy which exhibited two bands corresponding Si-Si bonds in crystalline and amorphous form.
- PL emission of freestanding nanocrystals shows intermittence on the time scale of a few seconds. Cryogenic experiments show different characteristics as a function of temperature. The bleaching in Si nanostructures is generally attributed to a blinking process which is observed in a single nanoparticle populated by more than one exciton under strong laser illumination. It is commonly accepted that the blinking occurs only in connection with and Auger assisted charge trapping. We discuss the observed PL decreasing in terms of exciton trapping at the interface between nanocrystal and the surrounding oxide layer.
- The strong PL emission performance of freestanding nanocrystals is excellent but the non-radiative transitions somehow reduce the overall emission. Therefore photoluminescence blinking and bleaching must be studied and understood in details in order to find how to increase and stabilize PL emission.

CHAPTER 7

CONCLUSIONS

We have presented experimental measurements on the luminescence properties of Si nanocrystals embedded in silicon dioxide matrix. In effort to enhance the understanding of Si nanostructure properties, a fabrication process based on the combination of ion implantation, sputtering, and laser pyrolysis and annealing has been studied to yield well controlled luminescent Si nc. The samples studied by ion implantation have the advantage of great controllability. However it also introduces damage into sample, which requires high temperature annealing to repair. The choice of the annealing environment was found to have a significant importance on the luminescence of Si nanocrystals. PL from annealed at 1050 °C in N₂ and %5 H₂ in N₂ were found similar but the latter one show more efficient PL. The increase on the PL intensity is due to the passivation of non-radiative defects on the nanocrystals/oxide interface. The passivation with Hydrogen influences the efficiency of PL but not the peak position nor its shape. Additionally, it is also clear that with the increase of the annealing time a better passivation of nanocrystals surface is reached with the consequent reduction of non-radiative decay channels.

We have demonstrated the effect of nanocrystals size to photoluminescence properties. Since the emission wavelength corresponds to size of nanocrystals, the red shift (QC) corresponds to an increase in the mean size optically active Si nanocrystals.

It is fact that, larger nanocrystals have a large surface area and thus more likely to contain defects. The temperature dependence of PL intensity was studied. By analyzing the temperature dependence of both PL intensity and lifetime, the activation energy has been calculated. This energy decreases by increasing Nc size in accordance with prediction of quantum confinement models. The temperature dependence of Si nanocrystals have been investigated in detail by using time-resolved photoluminescence to show the effect of excitonic fine structure of Si nanocrystals. Due to QC effects, the optical gap shifts to the higher energies as the nanocrystal size decreases as expected from quantum size effect. From the behavior of PL decay time as a function of temperature and wavelength, we have concluded that the light generation in nanocrystals occurs via involvement of three excitonic levels as suggested by a recently proposed model. The life times of the carriers residing in these levels have been determined by a curve fitting procedure, and found to be shorter than the previously reported values. The difference in the life time values can be attributed to the structural differences.

The freestanding Si nanocrystals were studied using temperature dependent PL. PL spectrum of nanocrystals show broad shape band that fitted four Gaussian peaks. Cryogenic experiments performed down to 20 K and the main peak shifted towards higher energies. The emission PL spectra were collected with using two excitation wavelengths 325 nm and 532 nm. A size-dependent luminescence property is observed in the PL spectra as expected. The observed blue shift (45 nm) in PL maximum can be attributed to quantum confinement effects arising from decreased particles size. The high resolution transmission electron microscopy images confirmed the presence of both crystalline and amorphous nanoparticles with an average diameter of 5 nm. The chemical structure of the nanoparticles was identified by using Raman spectroscopy which exhibits Si-Si bonds in crystalline and amorphous form. PL emission of freestanding nanocrystals shows intermittence on the time scale of a few seconds. Cryogenic

experiments show different characteristics as a function of temperature. The bleaching in Si nanostructures is generally attributed to a blinking process which is observed in a single nanoparticle populated by more than one exciton under strong laser illumination. It is commonly accepted that the blinking occurs only in connection with and Auger assisted charge trapping. We discuss the observed PL decreasing in terms of exciton trapping at the interface between nanocrystal and the surrounding oxide layer. The strong PL emission performance of freestanding nanocrystals is excellent but the non-radiative transitions somehow reduce the overall emission.

Future Work

Although the intense research effort directed on the Si nc over the two decades, a great number of question remain unanswered. Actually there is much intention for developing the understanding of optical properties of Si nanocrystals. This is significant because, although there is a general understanding and several model proposed of the PL mechanisms, the exact mechanisms still under debate. The broad PL of Si nanocrystals hamper the understanding of the PL mechanisms. To handle this problem single dot spectroscopy are needed to reveal the PL mechanisms. This method is widely used for III- V and II- IV semiconductors but has rarely been used for Si nanocrystals. The use of Single dot spectroscopy techniques allowed the luminescence from each nanostructure to be individually resolved. Through single nanocrystal measurements, there can also be opportunity to measure the passivation efficiency directly and the efficiency on photoluminescence. Therefore photoluminescence blinking and bleaching should be studied and understood in details in order to find mechanisms of the PL emission from Si nanocrystals.

REFERENCES

- [1] S. M. Sze and K. K. Ng, *Phys. of semiconductor devices*, 3rd ed. 2006, Wiley.
- [2] M. A. Green, *Silicon solar cells advanced principles and practice*, Centre for Photovoltaic Devices and Systems, University of New South Wales, Sydney (1995).
- [3] A. G. Cullis and L. T. Canham, *Nature* 353, 335 (1991)
- [4] L. Pavesi, L. Dal Negro, C. Mazzoleni, G. Franzo, F. Priolo, *Nature* 408, 440 (2000)
- [5] F. Iacona, G. Franzo, C. Spinella, *J. Appl. Phys.* 87, 1295 (2000)
- [6] S. Ossicini, L. Pavesi, and F. Priolo, *Light Emitting Silicon for Micro-photonics*, Springer Tracts on Modern Physics, Springer-Verlag, Berlin, 194 (2003)
- [7] O. Bisi, S. Ossicini, L. Pavesi, *Surf. Sci. Rep.* 38, 1-126 (2000)
- [8] J. Wang, Righini M., Gnoli A, Foss S, Finstad T, Serincan U, Turan R., *Solid State Comm.* 147, 461, (2008)
- [9] Prof. Jasprit Singh's Homepage, <http://www.eecs.umich.edu/~singh/>, last visited on March 2010
- [10] A. L. Efros and M. Rosen, *Annu. Rev. Mater. Sci.* 30, 475-521 (2000)
- [11] P. Moriarty, *Rep. Prog. Phys.* 64, 297-381 (2001)
- [12] L. Pavesi, *J. Phys.: Condens. Matter* 15, R1169-R1196 (2003)
- [13] A. G. Nassiopoulou, "Silicon nanocrystals in SiO₂ thin layers," in *Encyclopedia of Nanoscience and Nanotechnology*, H. S. Nalwa Ed., Vol. 9, 793-813, American Scientific, CA (2004).
- [14] L. T. Canham, *Appl. Phys. Lett.* 57, 1046-1048 (1990)

- [15] D. Kovalev, H. Heckler, G. Polisski, and F. Koch, *Phys. stat. sol. (b)* 215, 871-932 (1999)
- [16] G. Amato, C. Delerue, and H.-J. von Bardeleben, Eds., *Structural and Optical Properties of Porous Silicon Nanostructures*, Vol. 5, Gordon & Breach, Amsterdam (1997)
- [17] A. G. Cullis, L. T. Canham, and P. D. J. Calcott, *J. Appl. Phys.* 82, 909-965 (1997)
- [18] J. Gole and D. A. Dixon, *Phys. Rev. B.* 57, 12002-12016 (1998)
- [19] J. Heitmann, F. Müller, M. Zacharias, and U. Gösele, *Adv. Mater.* 17, 795-803 (2005)
- [20] M. Dovrat, Y. Oppenheim, J. Jedrzejewski, I. Balberg, and A. Sa'ar, *Phys. Rev. B.* 69, 155311 (2004)
- [21] M. Dovrat, Y. Goshen, I. Popov, J. Jedrzejewski, I. Balberg, and A. Sa'ar, *Phys. stat. sol. (c)* 2, 3440-3444 (2005)
- [22] M. V. Wolkin, J. Jorne, P. M. Fauchet, G. Allan, and C. Delerue, *Phys. Rev. Lett.* 82, 197-200 (1999)
- [23] S. Godefroo, M. Hayne, M. Jivanescu, A. Stesmans, M. Zacharias, O. I. Lebedev, G. Van Tendeloo, and V. V. Moshchalkov, *Nature Nanotech.* 3, 174-178 (2008)
- Chp2
- [24] T. Shimizu-Iwayama, K. Fujita, S. Nakao, K. Saitoh, T. Fujita, and N. Itoh, *J. Appl. Phys.* 75, 7779 (1994).
- [25] K. S. Min, K. V. Shcheglov, C. M. Yang, H. A. Atwater, M. L. Brongersma, and A. Polman, *Appl. Phys. Lett.* 69, 2033 (1996)
- [26] T. Shimizu-Iwayama, N. Kunumado, D. E. Hole, and P. Townsend, *J. Appl. Phys.* 83, 6018 (1998).

- [27] M.L. Brongersma, Optical properties of ion beam synthesized Si nanocrystals in SiO₂, PhD thesis, Utrecht University (1998).
- [28] J. Linnros, N. Lalic, A. Galeckas, and V. Grivickas, *J. Appl. Phys.* 86, 6128 (1999).
- [29] Q. Zhang, S. C. Bayliss, and D. A. Hutt, *Appl. Phys. Lett.* 66, 1977 (1995)
- [30] J. U. Schmidt and B. Schmidt, *Mat. Sci. Eng. B* 101, 28 (2003)
- [31] Cannon W. R., Danforth S. C., Flint J. H., Haggerty J. S. and Marra R. A., *J. Am. Ceram. Soc.*, 65, 324–330 (1982)
- [32] Cannon W. R., Danforth S. C., Haggerty J. S. and Marra R. A., *J. Am. Ceram. Soc.*, 65, 330–335 (1982)
- [33] L. A. Nesbit, *Appl. Phys. Lett.* 46, 38 (1985)
- [34] C. F. Lin, W. T. Tseng, and M. S. Feng, *J. Appl. Phys.* 87, 2808 (2000).
- [35] U. Kahler and H. Hofmeister, *Opt. Mat.* 17, 83 (2001)
- [36] M. Zacharias, J. Heitmann, R. Scholz, U. Kahler, M. Schmidt, and J. Blasing, *Appl. Phys. Lett.* 80, 661 (2002)
- [37] G. A. Kachurin, K.S. Zhuravlev, H. Tang, *Nucl. Instr. Meth. Phys. Res. B*, 127/128, 583 (1997)
- [38] Georgia Tech. homepage, <http://www.ece.gatech.edu/research/labs/vc/theory/ionimplant.html>, last visited on March 2010
- [39] J. S. Haggerty, R. W. Cannon, Sinterable powders from laser driven reactions. In: Steinfeld JI (ed) *Laser-induced chemical processes*. Plenum Press, New York, 165–241 (1981)
- [40] A. S. Alagöz, Ms. Thesis, METU, August (2005)
- [41] AJA International Inc., <http://www.ajaint.com/whatis.htm>, last visited on March 2010

- [42] D'Amato R., Falconieri M., Fabbri F., Bello V., E. Borsella, J. Nanopart. Res., 10.1007/s11051-009-9746-3 (2009)
- [43] W. R. Cannon, S. C. Danforth, J. H. Flint, J. S. Haggerty and R. A. Marra, J. Am. Ceram. Soc. 65, 324–330 (1982)
- [44] W. R. Cannon, S. C. Danforth, J. H. Flint, J. S. Haggerty and R. A. Marra, J. Am. Ceram. Soc., 65, 330–335 (1982)
- [45] Veinot J. G. C., Chem. Commun., 40, 4160–4168 (2006)
- [46] E. Borsella, S. Botti, M. Cremona, S. Martelli, R. M. Montreali and A. Nesterenko, J. Mater. Sci. Lett., 16, 221–223 (1997)
- [47] S. Botti, R. Coppola, F. Gourbilleau and R. Rizk, J. Appl. Phys., 88, 3396–4836 (2000)
- [48] F. Huisken, B. Kohn and V. Paillard, Appl. Phys. Lett., 74, 3776–3778 (1999)
- [49] G. Ledoux, J. Gong and F. Huisken, Appl. Phys. Lett., 79, 4029–4030 (2001)
- [50] G. Ledoux, J. Gong, F. Huisken, O. Guillois and C. Reynaud, Appl. Phys. Lett., 80, 4834–4836 (2002)
- [51] E. Trave, V. Bello, F. Enrichi, G. Mattei, E. Borsella, M. Carpanese, M. Falconieri, C. Abate, N. Herlin-Boime, K. Jursiokova, F. Costa, L. Costa, L. Gini, Opt. Mater. 27, 1014–1019 (2005)
- [52] X. Li, Y. He, S. S. Talukdar and M. T. Swihart, 4720–4727 (2004)
- [53] D'Amato R, Falconieri M, Carpanese M, Fabbri F, Borsella E Appl Surf Sci 253, 7879–7883 (2007)
- [54] G.D. Gilliland, Materials Science and Engineering, R18, 99 (1997)
- [55] Prof. Jasprit Singh's Homepage, <http://www.eecs.umich.edu/~singh/>, last visited on March 2010
- [56] X. X. Wang, J. G. Zhang, L. Ding, B. W. Cheng, W. K. Ge, J. Z. Yu, and Q. M. Wang, Phys. Rev. B 72, 195313 (2005)

- [57] Y. Kanemitsu, Tetsuo Ogawa, Kenji Shiraishi, and Kyozauro Takeda, Phys. Rev. B 48, 4883 (1993)
- [58] H. Takagahara, Kyozauro Takeda, Phys. Rev. B 46, 15578 (1992)
- [59] J. P. Proot, C. Delerue and G. Allan, Appl. Phys. Lett. 61, 1948 (1992)
- [60] G. Ledoux, O. Guillois, D. Porterat, C. Reynaud, F. Huisken, B. Kohn, V. Paillard, Phys.Rev. B 62, 15942 (2000)
- [61] S. Ögüt, James R. Chelikowsky, Steven G. Louie, Phys. Rev. Lett. 79, 1770 (1997)
- [62] G. Hadjisavvas , P. C. Kelires, Phys. Rev. Lett. 93, 226104 (2004)
- [63] A. Yu. Kobitski, K. S. Zhuravlev, H. P. Wagner, D. R. T. Zahn, Phys. Rev. B 63, 115423 (2001)
- [64] Fauchet P.M. et. al., J.Lumin70, 294 (1996)
- [65] B. Averboukh, R. Huber, K. W. Cheah, Y. R. Shen, G. G. Qin, Z. C. Ma, and W. H. Zong., J. Appl. Phys. 92, 3564(2002)
- [66] U. Serincan, G. Aygun and R. Turan, Journal of Luminescence 113, 229–234 (2005)
- [67] B. Garrido, Nucl. Inst. Meth. Phys. Res. B 216, 213 (2004)
- [68] Y. Kanemitsu, H. Uto, Y. Masumoto, T. Matsumoto, T. Futagi, H. Miura, Phys. Rev. B 48, 2827 (1993)
- [69] P. D. J. Calcott et al., J.Luminescence. 57, 257, (1993)
- [70] S. Schuppler, S.L. Friedman, M.A. Marcus, D.L. Adler, Y.-H. Xie, F.M. Ross, Y.J. Chabal, T.D. Harris, L.E. Brus, W.L. Brown, E.E. Chaban, P.F. Szajowski, S.B. Christman, P.H. Citrin, Phys. Rev. B 52, 4910 (1995)
- [71] Y. Yamada, T. Orii, I. Umez, S. Takeyama, T. Yoshida, Jpn J. Appl. Phys. 35, 1361 (1996)
- [72] M. Ehbrecht, B. Kohn, F. Huisken, M.A. Lagun, V. Paillard, Phys. Rev. B 56, 6958 (1997)

- [73] S. Takeoka, M. Fujii, S. Hayashi, *Phys. Rev. B* 62, 16820 (2000)
- [74] M. L. Brongersma, P.G. Kik, A. Polman, K.S. Min, H.A. Atwater, *Appl. Phys. Lett.* 76, 351 (2000)
- [75] Marcofabio Righini, Jiwei Wanga, Andrea Gnoli, Steinar Foss, Terje Finstad, Ugur Serincan, Rasit Turan, *Solid State Commun.* 147, 461–464 (2008)
- [76] M.Dovrat, Y. Shalibo, N. Arad, I. Popov, S.-T. Lee, A. Sa'ar, *Phys. Rev B* 79, 125306 (2009)
- [77] D. Kovalev, H. Heckler, G. Polisski, and F. Koch, “*Physica Status Solidi B*, vol. 215 (2), pp. 871–932 (1999)
- [78] C. Delerue, G. Allan, M. Lannoo, *Phys. Rev. B* 48, 11024 (1993)
- [79] S. Lutjohann, C. Meier, M. Offer, A. Lorke, and H. Wiggers, *Europhys. Lett.* 79, 37002 (2007)
- [80] J. Mayandi, T. G. Finstad, A. Thogersen, S. Foss, U. Serincan and R. Turan, *Thin Solid Films* 515, 6375 (2007)
- [81] M. F. Shlesinger and E. W. Montroll, *Proc. Natl. Acad. Sci. USA*, 81, 1280 (1984)
- [82] J. Kakalios et al., *Phys. Rev. Lett.*, 59 1037 (1987)
- [83] B. Delley and E. F. Steigmeier, *Phys. Rev. B* 47, 1397 (1993)
- [84] S. Y. Ren, *Phys. Rev. B* 55, 4665 (1997)
- [85] J. P. Wilcoxon, G. A. Samara, P. N. Provencio, *Phys. Rev. B*, 60, 2704 (1999)
- [89] F. A. Reboredo, A. Franceschetti, and A. Zunger, *Appl. Phys. Lett.* 75, 2972–2974 (1999)
- [87] D. J. Lockwood, *J Mater Sci: Mater Electron* 20, S235–S244 (2009)
- [88] Y. Kanemitsu, S. Okamoto, M. Otake, and S. Oda, *Phys. Rev. B*, vol. 55 (12), pp. R7375–R7378 (1997)

- [89] M. Kulakci, U. Serincan, R. Turan and T. Finstad, *Nanotechnology* 19, 455403 (2008)
- [90] F. A. Reboredo, A. Franceschetti, and A. Zunger, *Phys. Rev. B* 61, 13073–13087 (2000)
- [91] D. H. Feng, Z. Z. Xu, T. Q. Jia, X. X. Li, and S. Q. Gong, *Phys. Rev. B* 68, 035334 (2003)
- [92] H. Ch. Weissker, J. Furthmüller, and F. Bechstedt, *Phys. Rev. B* 69, 115310 (2004)
- [93] B. Delley; E. F. Steigmeier, *Phys. Rev. B* 47, 1397 (1993)
- [94] C. S. Garoufalis, A. D. Zdetsis, S. Grimme, *Phys. Rev. Lett.* 87, 276402 (2001)
- [95] H. Ch. Weissker, J. Furthmüller, F. Bechstedt, *Phys. Rev. B* 65, 155328 (2002)
- [96] T. Takagahara, K. Takeda, *Phys. Rev. B* 46, 15578 (1992)
- [97] A. Meldrum, *Recent Res. Dev. Nucl. Phys.* 1, 93 (2004).
- [98] R. J. Walters, G. I. Bourianoff, H. A. Atwater, *Nature Mater.* 4, 143–146 (2005)
- [99] S. Tiwari, et al. *Appl. Phys. Lett.* 68, 1377–1379 (1996)
- [100] J. R. Heath, *Science* 258, 1131–1133 (1992)
- [101] F. Huisken, *Appl. Phys. Lett.* 79, 4029–4030 (2001)
- [102] F. Hua, M. T. Swihart and E. Ruckenstein, *Langmuir* 21, 6054–6062 (2005)
- [103] X. Li, Y. He, S. S. Talukdar and M. T. Swihart, *Langmuir* 20, 4720 (2004)
- [104] Liu, Yang Y., Sato S. and Kimura K., *Chem. Mater.* 18, 637–642 (2006)
- [105] C. M. Hessel, M. Colin, E. J. Henderson, and J. G. C. Veinot, *Chem. Mater.* 18, 6139–6146 (2006)
- [106] Khriachtchev L., Novikov S., *Appl. Phys. A* 87, 761–766 (2007)

- [107] F. Cichos, J. Martin, Ch. von Borczyskowski, Phys. Rev. B 70, 115314 (2004)
- [108] J. Valenta, Fucikova A., Vacha F., Adamec F., Humpolickova J., Hof M., Pelant I., Kusova K., Dohnalova K., J. Linnros, Adv.Func.Mate.18, 2666-2672(2002)
- [109] N. Herlin-Boime, M. Mayne-L’Hermite, C. Reynaud, In Naiwa HS (ed) Encyclopedia of nanoscience and nanotechnology, 10. ASP, Valencia (2004)
- [110] N. Maley, D. Beeman and J. S. Lannin, Phys. Rev.B 38, 10611(1988)
- [111] L. Khriachtchev, S. Novikov, J. Lahtinen, J.Appl. Phys. 92, 5856 (2002)
- [112] V. Domnich, Y. Gogotsi, Rev. Adv. Mater. Sci. 3, 1 (2002)
- [113] I.H. Campbell, P.M. Fauchet, Solid State Commun. 58, 739 (1986)
- [114] H.Richter, Z.P.Wang, L.Ley, Solid State Commun. 39, 625 (1981)
- [115] Ch. Ossadnik, S. Veprek, and I. Gregora, Thin Solid Films 337, 148 (1999)
- [116] L. Khriachtchev, M. Räsänen, S. Novikov, and L. Pavesi, Appl. Phys. Lett. 85, 1511 (2006)
- [117] F. Giuseppe, G. Santo, A. R. Pennisi, Phys. Lett. A, 373, 3779–3782 (2009)
- [118] H. Koyama, P.M. Fauchet, J. Appl. Phys. 87, 1788 (2000)

CURRICULUM VITAE

PERSONAL INFORMATION

Surname, Name: Seyhan, Ayşe

Nationality: Turkish (TC)

Date and Place of Birth: 12 September 1976 , Konya

Marital Status: Single

Phone: +90 312 210 5080

Fax: +90 312 210 1281

email: ayseyhan@metu.edu.tr

EDUCATION

Degree	Institution	Year of Graduation
MS	METU Department of Physics	2003
BS	Selçuk University Department of Physics	1997
High School	Atatürk High School, Konya	1993

WORK EXPERIENCE

Year	Place	Enrollment
2001-	METU Department of Physics	Research Assistant
1999-2001	Niğde Univ. Department of Physics	Research Assistant
Sept. 1997-Feb.1999	Kuluncak High School, Malatya	Teacher

FOREIGN LANGUAGES

English

TECHNICAL SKILLS AND EXPERTISE

Origin, LabVIEW, Peak Fit, MS Office, MS PowerPoint, Linux and qualified for instrumentation both in electronics and optics.

PUBLICATIONS

1. On the Excitonic Model for Light Emission Luminescence from Si Nanocrystals Embedded in SiO₂ matrix. **A. Seyhan**, M. Willander, M. Kulakci, R. Turan. Submitted to Journal of Luminescence.
2. Photoluminescence from Si Nanocrystals Embedded in SiO₂ Matrix in Weak Quantum Confined Regime, N. A. P. Mogaddam, **A. Seyhan**, A. G. Imer, R. Turan. Submitted to Journal of Applied Physics.
3. Photoluminescence spectra of nitrogen implanted GaSe crystals, M. Karabulut, G. Bilir, G.M. Mamedov, **A. Seyhan**, R. Turan, Journal of Luminescence 128, 1551 (2008)
4. Spectroscopic Measurements of Electron Temperature and Electron Density in Electron Beam Plasma Generator Based on Collisional Radiative Model, H. Goktas, A. Demir, E. Kacar, H. Hegazy, **A. Seyhan**, R. Turan, and G. Oke, Spectroscopy Letters, 40: 183–192, (2007)
5. Temperature and excitation intensity dependent photoluminescence in Ga₄Se₃S layered crystal, K. Goksen, N.M. Gasanly, **A. Seyhan**, R. Turan, Materials Science and Engineering B 127 , 41–46 (2006)
6. Optical Anisotropy in GaSe, **A. Seyhan**, O. Karabulut, B. G. Akinoglu, B. Aslan, R. Turan, Crystal Research Technology Cryst. Res. Technol. 40 (9), 893–895 (2005)
7. Photoluminescence spectroscopy in the study of growth of CdS_xSe_{1-x} nanocrystals in glass, C. Allahverdi, M.H. Yukselici, R. Turan, **A. Seyhan**, Semiconductor Science and Technology 19 (8): 1005-1009 (2004)

Book Chapters

1. Silicon Nanocrystals: Fundamentals, Synthesis and Applications. Chapter 21: Characterization of Si Nanocrystals, S. Yerci, I. Dogan, **A. Seyhan**, A. Gencer, and R. Turan Edited by Lorenzo Pavesi and Rasit Turan, Copyright 2010 Wiley-VCH Verlag GmbH & Co. KGaA, Weinheim, ISBN: 978-3-527-32160-5

Conferences/meetings

1. Study of the photoluminescence bleaching in Si nanocrystals prepared by Laser Assisted Silane pyrolysis. **A. Seyhan**, U. Guler, M. Falconieri, R. D'Amato, E. Borsella, R. Turan. BONSAI Symposium “ Breakthroughs in Nanoparticles for Bio Imaging”, Rome, Italy, April 8-9, 2010
2. Structural and optical properties of Al₂O₃ with Si and Ge nanocrystals, Yerci S, Yildiz I, **Seyhan A**, Kulakci M, Serincan U, Shandalov M, Golan Y, Turan R. MRS Fall Meeting Boston, MA, NOV 27, 2006 Group IV Semiconductor Nanostructures-2006 Book Series: Materials Research Society Symposium Proceedings, Volume: 958, Pages: 105-111 (2007)
3. Visible Photoluminescence from Al₂O₃ containing Ge nanocrystals, **A. Seyhan**, S. Yerci, A. Erbil, M. Kulakci, U. Serincan, A. Aydinli and R. Turan, International Workshop on SEMIconductor NANOstructures 2007, Bad Honnef, Germany, June 13th - 16th (2007)
4. PL and FTIR Analysis of Ge and Si Implanted SiO₂ Layers”, U. Serincan, S. Yerci, M. Kulakci, **A. Seyhan** and R. Turan, Poster presented at the Optical Interconnects 3rd Optoelectronic & Photonic Winter School 2005, Sardinia (Trento), Italy, 27 February 4 March (2005)
5. Photoluminescence of implanted GaSe(N) excitons, H. Mammadov, M. Karabulut, G. Bilir, R. Turan, **A. Seyhan**, Turkish Physical Society 23th Physics Meeting, Mugla, Turkey, September 13-16 (2005)
6. Investigation of optical anisotropy in GaSe with Photoluminescence and FTIR Spectroscopy, **A. Seyhan**, O. Karabulut, B. G. Akinoglu, B. Aslan, R. Turan. Poster presented at 11th National Condensed Matter Physics Meeting, Ankara, Turkey, December 3 (2004)
7. Measurements and modelling of neutral helium spectral lines emitted from electron beam generator, H. Goktas, A. Demir, R. Turan, **A. Seyhan**, G. Oke, International Conference Plasma 2003, Research and Applications of Plasmas, Warsaw, Poland, 8 – 12 September (2003)
8. The comparison of experimental and simulated ArI and ArII spectral lines emitted from electron beam generator, A. Demir, E. Hajiev, E. Kayhan, H. Goktas, **A. Seyhan**, R. Turan, International Conference Plasma 2003, Research and Applications of Plasmas, Varsaw, Poland, 8 – 12 September (2003)

HOBBIES

Scuba Diving

- Dive Master, PADI (**P**rofessional **A**ssociation of **D**iving **I**nstructors)
- Rescue Diver, PADI
- First Aid Instructor (Adult, Children, and Infant), PADI
- National Geographic Diver, PADI
- Underwater Photographer, PADI
- Wreck Diver, PADI
- Nitrox Diver, PADI
- Project Aware Specialist, PADI
- Specialty Diver, Equipment Specialist, PADI

Squash, Tracking, Taking Photograph, Movies, Playing Flute.